



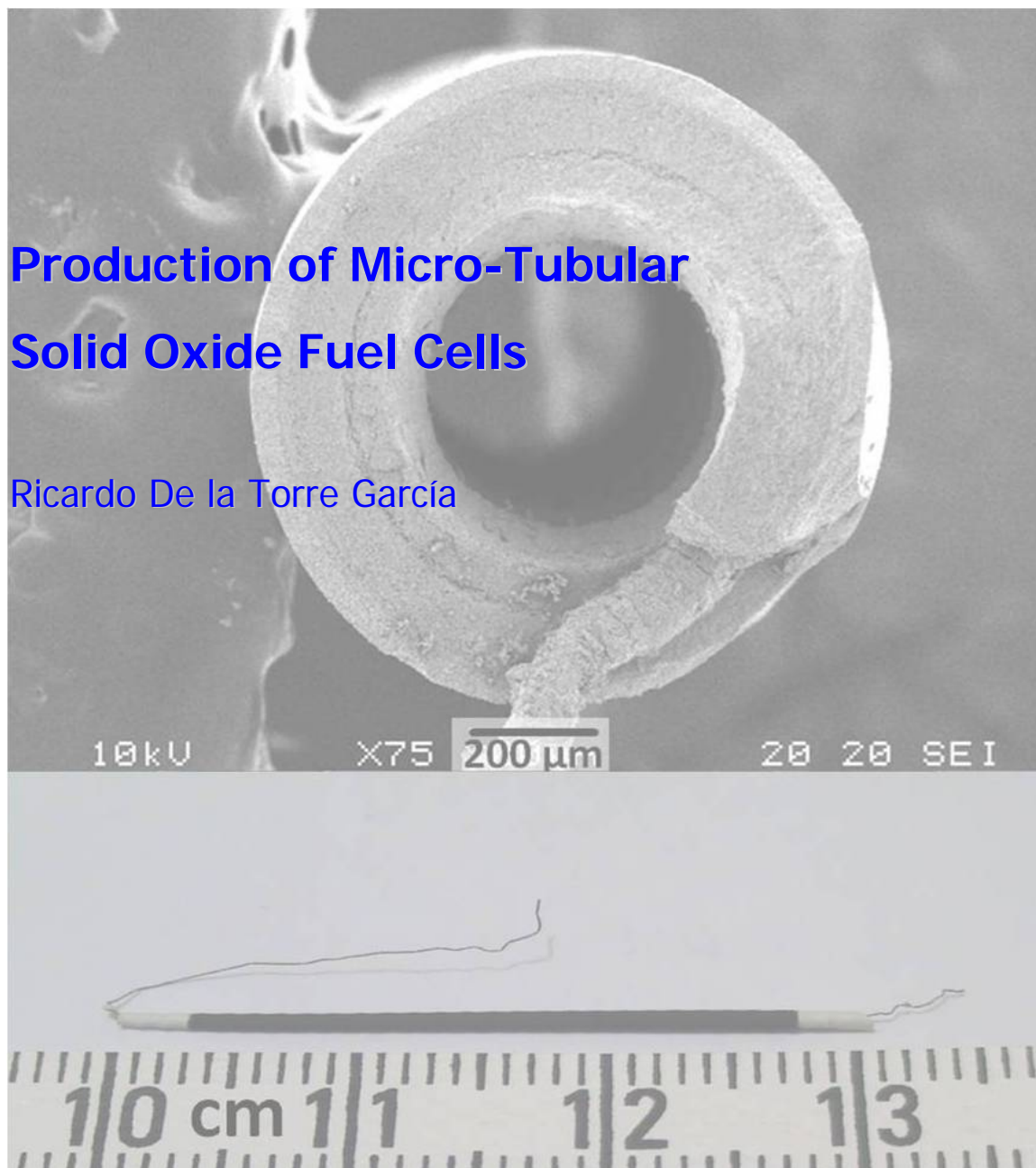
UNIVERSITY  
OF TRENTO - Italy

Department of Materials Engineering  
and Industrial Technologies

Doctoral School in Materials Engineering – XXIII cycle

## Production of Micro-Tubular Solid Oxide Fuel Cells

Ricardo De la Torre García



April 2011



# **Production of Micro-Tubular Solid Oxide Fuel Cells**

By

**Ricardo De la Torre García**

A thesis submitted to the University of Trento

For the degree of

Doctor of Philosophy

In

Materials Engineering

2011



# **Production of Micro-Tubular Solid Oxide Fuel Cells**

**Ricardo De la Torre García**

Advisor:  
Prof. Vincenzo M. Sglavo  
*University of Trento*

Committee:  
Prof. Gian Domenico Sorarù  
*University of Trento*

Prof. Herbert Danninger  
*Vienna University of Technology*

Prof. Michel Vert  
*University of Montpellier*

Prof. Laura Montanaro  
*Polytechnic University of Turin*



# Abstract

---

An innovative current collection architecture for micro-tubular solid oxide fuel cells (SOFC) has been developed. A nickel wire is coiled around a thin carbon composite rod in order to fabricate cell supports. Different carbon composites such as pencil leads and carbon fibres were investigated. The cell support was then coated with ceramic slurries based NiO/YSZ and YSZ for anode and electrolyte, respectively, by successive dip coatings. Effect of thermal behaviour, porosity, amount of binder and dip coating parameters were conjunctly analysed to produce anode and electrolyte crack-free layers with the thickness desired. Pyrolisable materials were then eliminated under air atmosphere at 800°C followed by co-sintering of half-cells at 1380°C for 2 h in argon to avoid the oxidation of the nickel wire. In order to complete the cells, sintered half-cells were dipped into cathode inks consisted of LSM-YSZ composite for a functional layer and LSM pure to increase the electrical conductivity of the cathode. The cathode was also sintered at 1150°C for 2 h under argon atmosphere.

Complete cells with an outer diameter below 1.2 mm and length of 30 mm with an effective cathode length of 20 mm and whose active cathode area is 0.75 cm<sup>2</sup> were produced.

## Abstract

---

The efficiency of the current collector method developed is evaluated by comparison with the performance of a micro-tubular cell produced and tested under similar conditions, but with a common current collection method. The results of I-V curves shown that the innovative current collection method enhances the performance of a typical micro-tubular cell in the order of 3-4 times. The improvement in performance is attributed to the reduction of current paths of the micro-tubular cells.

Suggestions for the production and characterization of current collector-supported micro-tubular cells are also given.

# Acknowledgements

---

First and foremost, I would like express my deep and sincere gratitude to my supervisor Prof. Vincenzo M. Sglavo for the constant support and guidance to complete this work. Many thanks for the trust and freedom to develop this research.

My sincere thanks are due to the official committee for their detailed review, constructive criticism and excellent advice during the preparation of this thesis.

During this work I have collaborated with many colleagues for whom I have great regard, and I wish to extend my warmest thanks to all of those who have helped me with my work in the Department of Ceramics in the University of Trento.

I would like express my gratitude to Michele Casarin for the valuable help and unconditional friendship.

## Acknowledgements

---

I owe my loving thanks to Wendy Hernández Soria for the constantly encouragement, love and patience for these three years.

Lastly, and most importantly, I wish thank my mother Elena García Vásquez for the endless encouragement and love. Equal gratitude goes to my brothers Raúl and Miguel Angel, my sister Ivonne and my nephew Alejandro for their love and support in any circumstance. Without their encouragement and understanding it would have been impossible for me to finish this work.

# Table of Contents

---

Abstract .....	i
Acknowledgements .....	iii
Table of Contents .....	v
List of Tables .....	viii
List of Figures .....	ix
Preface.....	1
1. Literature Review.....	3
1.1 Fuel Cell: General Aspects.....	3
1.1.1 Definition of a fuel cell.....	3
1.1.2 Types of fuel cells.....	4
1.2 Solid Oxide Fuel Cell.....	6
1.2.1 Overview.....	6
1.2.2 Principle of operation.....	7
1.2.3 Polarization curve .....	8
1.2.3.1 Nernst potential .....	8
1.2.3.2 Ohmic polarization.....	10
1.2.3.3 Activation polarization.....	11
1.2.3.4 Concentration polarization.....	12
1.2.4 Materials for SOFC.....	13
1.2.4.1 Electrolyte .....	13
1.2.4.2 Anode .....	19
1.2.4.3 Cathode.....	23
1.2.4.4 Interconnectors/current collectors .....	27
1.2.5 SOFCs design.....	28
1.2.5.1 Basics .....	28
1.2.5.2 Planar design .....	29
1.2.5.3 Tubular design.....	30

## Table of Contents

---

1.2.5.4 Miniaturization of SOFC.....	32
1.2.6 Micro-tubular SOFC .....	33
1.2.6.1 Fabrication techniques for micro-tubular SOFC.....	33
1.2.6.2 Current status of the performance of micro-tubular SOFCs .	37
1.2.7 Methods of current collection in tubular/micro-tubular SOFCs .....	43
1.2.7.1 Current collector placed along the cell.....	45
1.2.7.2 Current collector placed at one/two ends .....	51
1.3 Aim of the thesis.....	54
2. Experimental Procedure .....	55
2.1 Cell Supports .....	55
2.1.1 Cell support materials .....	57
2.1.1.1 Current collector.....	57
2.1.1.2 Sacrificial inner core .....	57
2.1.2 Production of cell supports .....	58
2.1.3 Pyrolyzation test .....	59
2.2 Powder Processing.....	61
2.2.1 Materials .....	61
2.2.2 Powders characterization and suspensions optimization .....	62
2.2.2.1 Sedimentation tests.....	63
2.2.2.2 Slurries preparation .....	65
2.2.2.3 Cathode ink preparation .....	65
2.3 Production of Micro-Tubular SOFC .....	66
2.3.1 Dip coating process for half-cells .....	67
2.3.2 Thermal analysis of half-cells.....	69
2.3.3 Effect of pore former in anode.....	70
2.3.4 Co-sintering of half-cells .....	71
2.3.5 Deposition and sintering of cathode .....	73
2.3.5.1 Cathode deposition and characterization.....	73
2.3.5.2 Sintering of cathode .....	75
2.4 Performance analysis of Micro-Tubular SOFC.....	76
2.4.1 Testing apparatus .....	76
2.4.1.1 Current collector-supported cells .....	76
2.4.1.2 Straight wire within the core of the cells.....	78
2.4.2 Conditions of testing .....	79
2.4.2.1 Anode reduction .....	79

## Table of Contents

---

2.4.2.2 Electrochemical testing .....	80
3. Results and discussion .....	81
3.1 Cell Supports .....	81
3.2 Powders Processing .....	85
3.2.1 SSA and dispersant concentration .....	85
3.2.2 Thermal analysis .....	85
3.2.3 Effect of pore former within the anode.....	93
3.2.4 Addition of binder .....	97
3.2.5 Cathode porosity .....	98
3.3 Production of Micro-Tubular Cells .....	102
3.3.1 Dip coating parameters .....	102
3.3.2 Drying conditions.....	103
3.3.3 Anode coating .....	104
3.3.4 Electrolyte coating and half-cell co-sintering.....	108
3.3.5 Remains from carbon composites.....	113
3.3.6 Cathode coating .....	115
3.4 Performance analysis of Micro-Tubular Cells .....	117
3.4.1 Cells size .....	117
3.4.2 Current paths.....	118
3.4.3 Performance of current collector-supported cells.....	121
3.4.3.1 Carbon fibre sacrificial core.....	121
3.4.3.2 Pencil lead sacrificial core.....	122
3.4.4 Performance of cells with straight wire within the cell core ..	124
3.4.4.1 Carbon fibre sacrificial core.....	124
3.4.4.2 Pencil lead sacrificial core.....	125
4. Conclusions .....	127
4.1 Cell Supports .....	127
4.2 Production of Micro-Tubular Cells .....	128
4.3 Performance of Micro-Tubular Cells .....	129
4.4 Future work .....	129
References .....	131

# List of Tables

---

Table 1.1: Characteristics of main types of fuel cells .....	5
Table 2.1: Pyrolysis tests conditions for cell supports .....	60
Table 2.2: Conditions analysed for dip coating process in half cells.....	67
Table 2.3: Conditions analysed for the cathode deposition .....	74
Table 3.1: Characteristics of cell supports .....	82
Table 3.2: SSA and dispersant concentration for different powders .....	85
Table 3.3: Anode slurries composition at different pore former contents ...	93
Table 3.4: Amount of binder added to the anode and electrolyte slurries ...	97
Table 3.5: Porosity of cathode at different solid load contents.....	98
Table 3.6: Dip coating parameters for the anode, electrolyte and cathode .....	103
Table 3.7: Drying conditions for the anode, electrolyte and cathode .....	103
Table 3.8: Effect of solid loading content on the anode coating.....	105
Table 3.9: Effect of solid loading content on the electrolyte coating .....	108
Table 3.10: Dimensions of the micro-tubular cells produced.....	117

# List of Figures

---

Figure 1.1: Schematic diagram of a single fuel cell.....	4
Figure 1.2: Schematic diagram of the polarization curve of a fuel cell .....	10
Figure 1.3: Temperature dependence of electric conductivity for oxide ion conductors (high temperature range).....	14
Figure 1.4: Temperature dependence of electric conductivity for oxide ion conductors (low temperature range).....	15
Figure 1.5: Conductivity of yttria and scandia stabilized zirconia in air at 1000°C .....	16
Figure 1.6: Variation of electrical conductivity measured at 1000°C as a function of nickel concentration of Ni/YSZ cermet fired at different temperatures .....	22
Figure 1.7: Schematic diagram showing the location of the triple-phase boundary (TPB) at cathode/electrolyte interface .....	24
Figure 1.8: Schematic diagram of the SOFC single cell support- configurations.....	29
Figure 1.9: Schematic diagram of the planar SOFC design.....	30
Figure 1.10: Schematic diagram of the tubular SOFC design .....	31
Figure 1.11: Schematic diagram of the conventional and electron current flow notation .....	45
Figure 1.12: Schematic diagram of a tubular cell and current path with Siemens cells configuration .....	46
Figure 1.13: Schematic diagram of a tubular cell and current path with a straight metal wire as current collector .....	47
Figure 1.14: Schematic diagram of a tubular cell with a spring coil as current collector .....	49
Figure 1.15: Schematic diagram of the current path in radial and axial direction with a spring coil as current collector .....	50

## List of Figures

---

Figure 1.16: Schematic diagram of a tubular cell and current path with the current collector wound at both ends .....	52
Figure 1.17: Schematic diagram of planar multi-cell array with interconnectors at ends .....	53
Figure 2.1: Schematic flow chart followed for the experimental procedure .....	56
Figure 2.2: Schematic diagram of the coiling system .....	59
Figure 2.3: Schematic diagram of the zones detected in sedimentation tests .....	64
Figure 2.4: Schematic flow chart to produce cells by dip coating .....	66
Figure 2.5: Thermal cycle for the sintering of half-cells .....	72
Figure 2.6: Thermal cycle for the sintering of cathode multi-layered .....	75
Figure 2.7: Schematic diagram of the setup apparatus for current collector-supported cells .....	77
Figure 2.8: Schematic diagram of the setup apparatus for a straight wire current collection method .....	78
Figure 3.1: Photograph of current collector supports with pencil leads and different wire diameter .....	82
Figure 3.2: Photograph of current collector supports with carbon fibre and different wire diameter .....	83
Figure 3.3: Photograph of current collector supports length .....	84
Figure 3.4: Photograph of 0.1 and 0.05 mm nickel wires after core elimination process .....	84
Figure 3.5: Dilatometric curves for anode cermet combinations .....	86
Figure 3.6: Dilatometric curves for electrolyte combinations .....	87
Figure 3.7: Photograph of NiO/(YSZS/YSZ)-YSZ half-cell sintered at 1380°C .....	89
Figure 3.8: Photograph of NiO/(YSZS/YSZ)-(YSZS/YSZ) half-cell sintered at 1380°C .....	90
Figure 3.9: Photograph of NiO/(YSZS/YSZ)-YSZS half-cell sintered at 1380°C .....	90
Figure 3.10: Photograph of NiO/YSZS-YSZS half-cell sintered at 1380°C .....	91
Figure 3.11: Photograph of NiO/YSZS-(YSZS/YSZ) half-cell sintered at 1380°C .....	92

## List of Figures

---

Figure 3.12: Photograph of NiO/YSZS-YSZS half-cell sintered at 1380°C .....	92
Figure 3.13: Effect of graphite content on the porosity of the anode cermet sintered at 1380°C .....	94
Figure 3.14: Micrograph of the anode microstructure without pore former sintered at 1380°C .....	95
Figure 3.15: Micrograph of the anode microstructure with 5 wt% of pore former sintered at 1380°C .....	95
Figure 3.16: Micrograph of the anode microstructure with 8 wt% of pore former sintered at 1380°C .....	96
Figure 3.17: Micrograph of the anode microstructure with 10 wt% of pore former sintered at 1380°C .....	96
Figure 3.18: Micrograph of the cathode microstructure with LSM pure at 20 wt% sintered at 1150°C .....	99
Figure 3.19: Micrograph of the cathode microstructure with LSM/YSZ at 20 wt% sintered at 1150°C .....	100
Figure 3.20: Micrograph of the cathode microstructure with LSM/YSZ at 30 wt% sintered at 1150°C .....	100
Figure 3.21: Micrograph of the cathode microstructure with LSM/YSZ at 40 wt% sintered at 1150°C .....	101
Figure 3.22: Micrograph of the cathode microstructure with LSM/YSZ at 50 wt% sintered at 1150°C .....	101
Figure 3.23: Photograph of the anode layer deposited with the slurry at 60 wt% (green state).....	105
Figure 3.24: Photograph of the anode layer deposited with the slurry at 70 wt% (green state).....	106
Figure 3.25: Photograph of the anode layer deposited with the slurry at 80 wt% (green state).....	106
Figure 3.26: Photograph of the anode layer deposited with the slurry at 85 wt% (green state).....	107
Figure 3.27: Photograph of the anode layer deposited with the slurry at 90 wt% (green state).....	107
Figure 3.28: Photograph of the electrolyte deposited with the slurry at 70 wt% (green state).....	109
Figure 3.29: Micrograph of the half-cell length with the electrolyte at 60 wt% sintered at 1380°C .....	110

## List of Figures

---

Figure 3.30: Micrograph of the half-cell diameter with the electrolyte at 60 wt% sintered at 1380°C .....	110
Figure 3.31: Micrograph of the half-cell length with the electrolyte at 70 wt% sintered at 1380°C .....	111
Figure 3.32: Micrograph of the half-cell diameter with the electrolyte at 70 wt% sintered at 1380°C .....	111
Figure 3.33: Micrograph of the half-cell length with the electrolyte at 80 wt% sintered at 1380°C .....	112
Figure 3.34: Micrograph of the half-cell diameter with the electrolyte at 80 wt% sintered at 1380°C .....	112
Figure 3.35: Photograph of the half-cells with pencil lead and carbon fibre as sacrificial inner core sintered at 1380°C .....	113
Figure 3.36: Micrograph of the remains deposited onto the inner anode surface .....	114
Figure 3.37: Micrographs of the complete current collector-supported cell .....	116
Figure 3.38: Photograph of the complete current collector-supported and common micro-tubular cell .....	118
Figure 3.39: Schematic diagram of the effect of a superficial and integrated current collector on the percolation paths in the anode cermet .....	119
Figure 3.40: Schematic diagram of the current path in radial and axial direction by using the current collector-supported method.....	120
Figure 3.41: Photograph of the longitudinal-section view of the current collector-supported cell .....	121
Figure 3.42: Performance of current collector-supported micro-tubular cell with carbon fibre as sacrificial inner core .....	122
Figure 3.43: Performance of current collector-supported micro-tubular cell with pencil lead as sacrificial inner core .....	123
Figure 3.44: Photograph of the longitudinal-section view of the cell tested with a common current collector.....	124
Figure 3.45: Performance of the micro-tubular cell with carbon fibre as sacrificial inner core and straight wire within the cell core as current collector .....	125

List of Figures

---

Figure 3.46: Performance of the micro-tubular cell with pencil lead as  
sacrificial inner core and straight wire within the cell core as  
current collector ..... 126

# Preface

---

This thesis is the second stage of a research project about the production of micro-tubular solid oxide fuel cells developed by the ceramics group at Department of Materials Engineering of the University of Trento.

A couple of years ago, the first stage of this research involved a conceptual novel current collection method. The results showed the potentiality of the concept and many observations were done to the development of these devices.

In the current research activity different approaches in design and production were considered for the development of the innovative current collection method and after many attempts its efficacy has been demonstrated.

Despite all the research related to the development of micro-tubular cells there are still some areas that can be improved upon. Specifically, the current collection method from the inner electrode has been one of the most concerned issues. The current collection methods frequently used by many researchers around the world involve techniques with low electric contact between the electrode and current collector, thus causing considerable ohmic losses due to longer current paths inherent to the tubular cell

## Preface

---

geometry. Furthermore, the electrical connections involve an extra step during assembly which becomes much more arduous when scaling down the diameter of the cells.

The current collection method described in this thesis offers an easy and effective way to integrate the current collector within the inner electrode during the production process. The main benefits are an homogeneous current collector along the cell length and the reduction of current paths. Additionally, the terminals of the cells completed are available to be connected easily without putting in risk the integrity of the cell or depending of the skills of an assembler.

This thesis is divided into 4 chapters; in the first chapter an introduction of the importance and motivations for micro-tubular cells interest among scientists from different fields as the next power system source for portable and mobile applications is given.

In chapters 2 and 3 the techniques, approaches and results accompanied by a discussion to understand the effect of the integrated current collector within the anode on the processing and performance of the micro-tubular cells are described.

Finally, in chapter 4 the most significant achievements are summarized and other current issues under analysis are reported.

Although further analysis should be required for the optimization of the proposed current collection method, this research represents a significant and tangible improvement in the development and overall knowledge of micro-tubular solid oxide fuel cells.

# **1. Literature Review**

## **1.1 Fuel Cell: General Aspects**

### **1.1.1 Definition of a fuel cell**

Fuel cells are electrochemical energy conversion devices which can continuously convert the chemical energy of a fuel and an oxidant into electrical energy and heat, without involving direct combustion as an intermediate step [1]. Since fuel cells convert chemical energy directly into electricity, they offer many advantages over traditional power sources such as improved efficiency, greater fuel diversity, high scalability, and have a lower impact on the environment [2-4]. Theoretically, fuel cells can produce electricity for as long as fuel (hydrogen, ethanol, methanol, or gaseous fossil fuels like natural gas) and oxidant (oxygen or air) are fed, but its degradation on service limits the practical life of the devices.

The basic structure of a fuel cell as shown in figure 1.1 consists of two electrodes electrically connected with a consumer load and separated by an electrolyte. The operating principle is based on the flux of electrons from

the anode to the cathode while the ions (positives or negatives) move through the electrolyte.

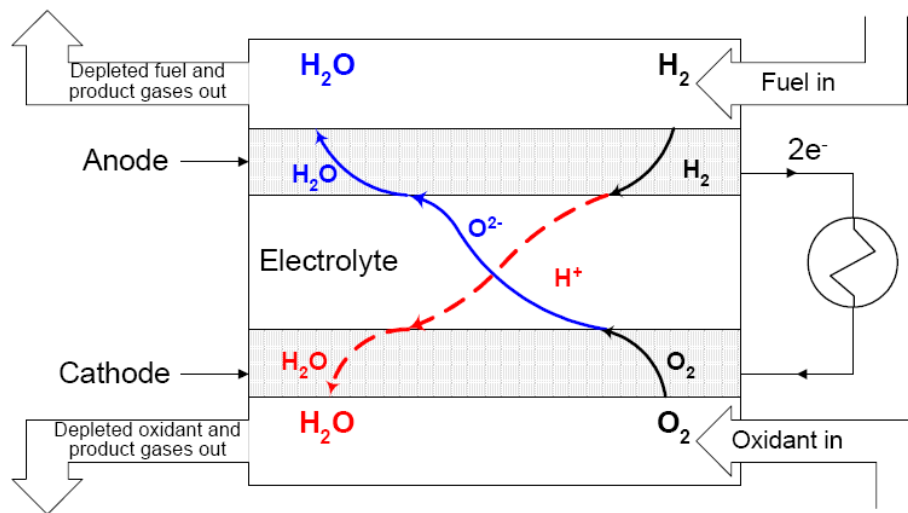


Figure 1.1. Schematic diagram of a single fuel cell (oxygen ion conductor - solid line, proton conductor - dashed line) [5].

### 1.1.2 Types of fuel cells

Many types of fuel cells have been developed; the most common classification is by the type of electrolyte (aqueous/liquid, polymeric and ceramic) and includes: Polymeric Electrolyte Membrane (PEMFC), Alkaline (AFC), Phosphoric Acid (PAFC), Molten Carbonate (MCFC), and Solid Oxide (SOFC) fuel cells. The main characteristics of fuel cells are summarized in Table 1.1.

Table 1.1. Characteristics of main types of fuel cells

	<b>PEMFC</b>	<b>AFC</b>	<b>PAFC</b>	<b>MCFC</b>	<b>SOFC</b>
Electrolyte	Polymeric membranes	Potassium hydroxide	Phosphoric acid	Molten carbonate	Ceramic
Charge carrier	H <sup>+</sup>	OH <sup>-</sup>	H <sup>+</sup>	CO <sub>3</sub> <sup>2-</sup>	O <sup>2-</sup>
Catalyst	Platinum	Platinum	Platinum	Electrode material	Electrode material
Operating Temperature (°C)	40-80	65-220	150-205	650	600-1000
Fuel	Pure H <sub>2</sub> , CO intolerant	Pure H <sub>2</sub> , CO intolerant	Relatively pure H <sub>2</sub>	Flexibility	Flexibility

The most important advantage of low and medium temperature fuel cells (PEMFC, PAFC and AFC) is a short start-up time which gives a great potential for mobile and portable electrical systems, though they have low impurities tolerance and require precious metal catalyst that raises the costs of the device.

For high temperature fuel cells (MCFC and SOFC), characteristics such as higher electrical efficiency and continuous electrical production allow stationary applications, but long start-up times and periodical maintenance must be considered.

The solid oxide fuel cells have exceptional potential for use as electric power generation systems, because of their high energy conversion efficiency which can reach up to 65%. In addition, the use of a solid and non corrosive electrolyte in SOFC is another advantage compared to the other high temperature fuel cell (MCFC).

## **1.2 Solid Oxide Fuel Cell**

### **1.2.1 Overview**

Solid oxide fuel cells (SOFCs) are the most efficient devices yet invented for conversion of chemical fuels directly into electrical power. These fuel cells provide many advantages over traditional energy conversion systems including high efficiency, reliability, modularity, fuel adaptability, and very low levels of SO<sub>x</sub> and NO<sub>x</sub> emissions. Quiet, vibration-free operation of solid oxide fuel cells also eliminates noise usually associated with conventional power generation systems. Furthermore, because of their high operation temperature (800-1000°C), some hydrocarbon fuels such as natural gas can be reformed within the cell stack eliminating the need for an expensive, external reformer [6,7]. In addition, the recovering heat of the hot gas exhausted from SOFC makes it possible to integrate with conventional heat engines such as gas turbine. Earlier theoretical studies show that synergic effect of these integrated

systems results in higher efficiencies (70%) than that of any power generation system constructed till today [8,9].

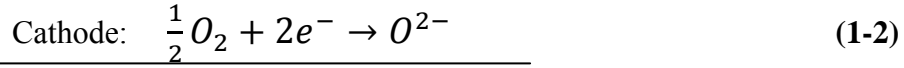
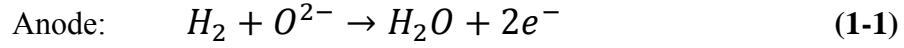
SOFCs are potentially used in many areas, such as residential, communicational commercial, industrial and military services [10]. In the last decade, considerable efforts have been focused on SOFCs all over the world, and kilowatt range SOFC plants have been successfully constructed and are being designed for demonstration [11]. Currently, SOFC are being preferred with respect to PEM fuel cells for automotive auxiliary power units (APUs). This happens despite the slow start-up and beside the fuel flexibility, because of the following benefits: cogeneration and internal reforming opportunities; no need of water management; simple reformer technology; high electrical efficiency; no noble catalyst and low noise [12,13]. However, in order to achieve commercialization of SOFC technology, the cell costs have to be reduced remarkably, which can be achieved by; using less expensive materials, increasing the output density, improving the cell performance and reliability and more importantly by improving fabrication techniques [14].

### **1.2.2 Principle of operation**

As shown in figure 1.1, a single cell consists of three main components: an anode, a cathode and a solid electrolyte separating the two electrodes. In the case of SOFCs the air and hydrogen flow through cathode and anode, respectively. Under electrical load at the cathode surface the presence of perovskite catalyst enables oxygen ionization. The solid electrolyte allows

oxygen ions flux to the anode, where they electro-oxidize hydrogen, thus releasing heat, water and electrons. Since electrolyte materials ensures quasi-zero electronic conductivity, electrons are forced to flow through interconnect and external load towards the cathode, thus closing the electrical loop [15].

The overall electrochemical reaction for SOFC is given by:



### **1.2.3 Polarization curve**

#### ***1.2.3.1 Nernst potential***

When the SOFC is not connected to an external load, there is no current flow outside of the cell and the operating voltage is equal to the open-circuit voltage (OCV). The OCV is typically assumed to the equilibrium Nernst potential for the overall electrochemical reaction [16].

$$V_{Nernst} = -\frac{\Delta G^o}{nF} - \frac{RT}{nF} \ln \left( \frac{p_{H_2O}}{(p_{H_2})(\sqrt{p_{O_2}})} \right) \quad (1-4)$$

Where  $n$  is the number of electrons participating in the electrochemical reaction,  $R$  is the universal gas constant,  $F$  is the Faraday constant,  $T$  is the cell temperature and  $p$  the partial pressure for respective species.

As the cells to supply current to an external load, it moves away from a state of equilibrium and the operating voltage drops due to irreversibilities associated with internal charge transfer, conduction and diffusion process. These irreversibilities are individually categorized as ohmic, activation and concentration polarizations. These polarizations can be considered as voltage losses and are given as follows:

$$V_{loss} = V_{ohm} + V_{act} + V_{conc} \quad (1-5)$$

Accordingly, cell voltage can be expressed as:

$$V_{Cell} = V_{Nernst} - V_{loss} \quad (1-6)$$

Figure 1.2 shows the polarization curve of a fuel cell. In it, cell voltage is plotted against current density. Higher current densities induce higher losses. Ohmic losses dominate the central range of current, whereas activation and concentration losses are predominant at low and high current densities, respectively.

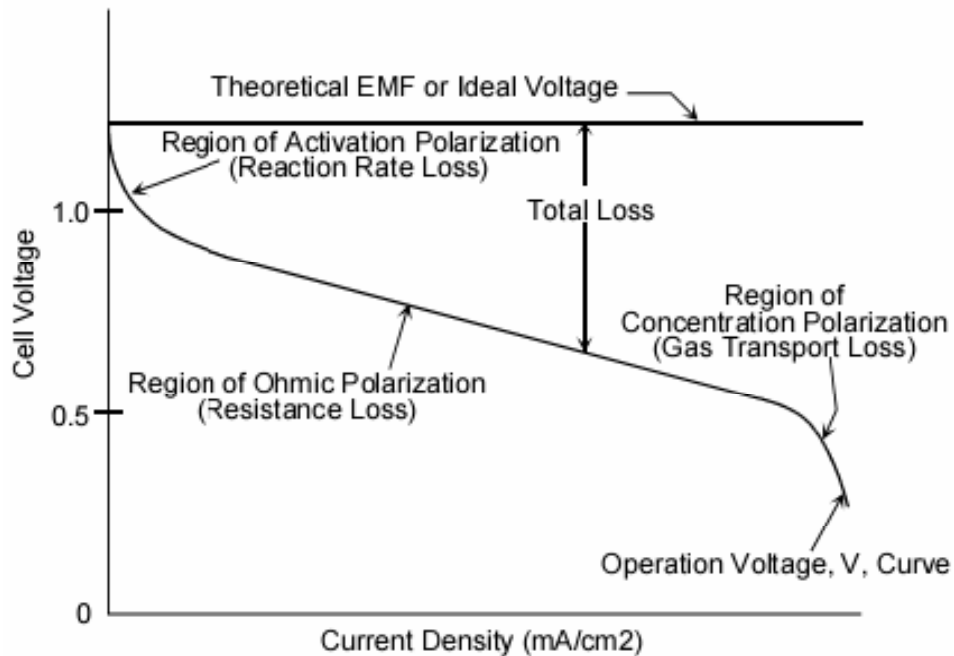


Figure 1.2. Schematic diagram of the polarization curve of a fuel cell [17].

### 1.2.3.2 Ohmic polarization

Ohmic losses occur because of resistance resulting from the flow of ions in the electrolyte and the flow of electrons through the electrode (interfaces between the electrodes and the electrolyte and between the electrode and the current collectors (contact resistance)). The cell ohmic resistance depends on the anode, cathode and electrolyte resistances [18,19]. Ohmic polarization is expressed by Ohm's law:

$$\eta_{ohm} = i\Sigma R_i \quad (1-7)$$

Where  $R_i = \frac{\rho_i \delta_i}{A_i}$  is the ohmic resistance of anode, cathode and electrolyte;  $A_i$  is the respective area of the section where the current flows,  $\delta_i$  is the correspondent flow length and  $\rho_i$  is the material resistivity, which is a strong function of temperature.

In most fuel cells the ohmic polarization is mainly caused by the electrolyte, though the cell resistance related to interconnectors or bipolar plates can also be important [20]. This kind of polarization can be reduced using highly conductive materials, thin electrolytes, and better performing interconnectors [21].

### **1.2.3.3 Activation polarization**

Chemical reactions, including electrochemical reactions, involve energy barriers that must be overcome by reacting species. This energy barrier is called the activation energy and results in activation polarizations, which is due to the transfer of charges between the electronic and ionic conductors [22]. Although it is generally supplied as heat, in fuel cells it is subtracted to the ideally available electromotive force and it is dissipated as heat. In general, activation overpotential depends on material properties and microstructure, temperature and pressure of the reactants and current density [23].

This type of polarization is mostly due to the cathode electrode because the rate of oxygen reduction at the cathode is orders of magnitude slower than the rate of hydrogen oxidation reaction at the anode.

### **1.2.3.4 Concentration polarization**

As fuel is depleted, hydrogen and oxygen partial pressures decrease at anode and cathode, respectively. The depletion rate depends on average current density drawn from the cell. As the current density increases, the partial pressures decrease and eventually an insufficient amount of reactants are transported to the electrodes [19]. When the electrode process is governed completely by diffusion, the limiting current,  $i_L$ , is reached. The limiting current can be calculated from the diffusion coefficient of the reacting species,  $D$ , their concentration,  $C_M$ , the number of electrons involved in the reaction to convert a single fuel molecule,  $z$ , and the thickness of the diffusion layer,  $\delta$ , by applying Fick's law as:

$$i_L = \frac{zFD\Delta C_M}{\delta} \quad (1-8)$$

For an electrode process free of activation polarization, the diffusion or concentration polarization can be expressed as:

$$\eta_D = \frac{RT}{zF} \ln \left( 1 - \frac{i}{i_L} \right) \quad (1-9)$$

In general, mass transport is a function of temperature, pressure and concentration of the species involved. In SOFCs the reactants must diffuse through the porous anode and cathode, emphasizing the importance of the microstructure and design of electrodes [24].

The main source of this polarization is again the cathode, because oxygen diffusivity is significantly lower than that of hydrogen due to the larger oxygen molecule size.

## **1.2.4 Materials for SOFC**

### ***1.2.4.1 Electrolyte***

The electrolyte in SOFC should satisfy numerous requirements, including fast ionic transport, negligible electronic conduction, thermodynamic stability over a wide range of temperature and stability under oxidizing and reducing atmospheres. In addition, it must possess thermal expansion compatible with that of the electrodes and other construction materials, high density, negligible volatilization of components, suitable mechanical properties and negligible interaction with electrode materials under operation conditions [25,26].

The conductivity of the electrolyte determines the operating temperature of SOFCs. The temperature dependence of conductivity in typical solid oxide ion conductors is summarized in figures 1.3 and 1.4 for the high and lower temperature ranges, respectively.

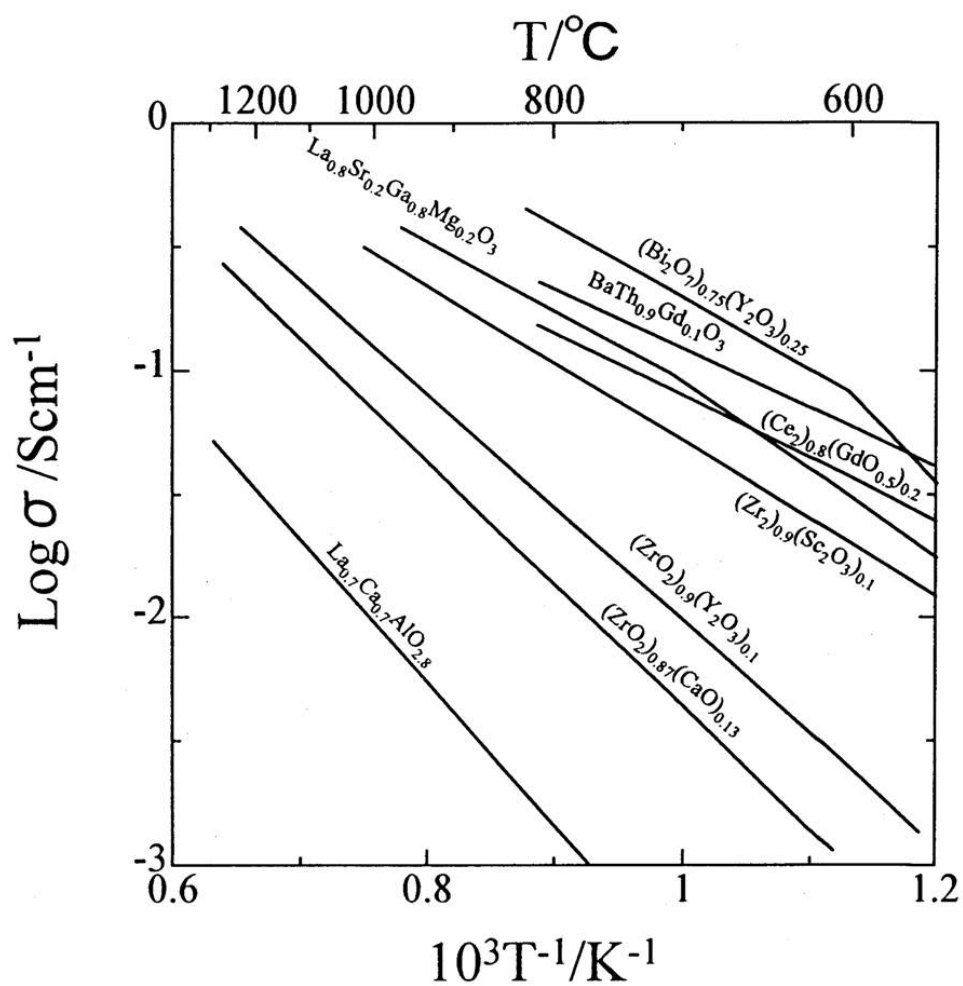


Figure 1.3. Temperature dependence of electrical conductivity for oxide ion conductors (high temperature range) [26].

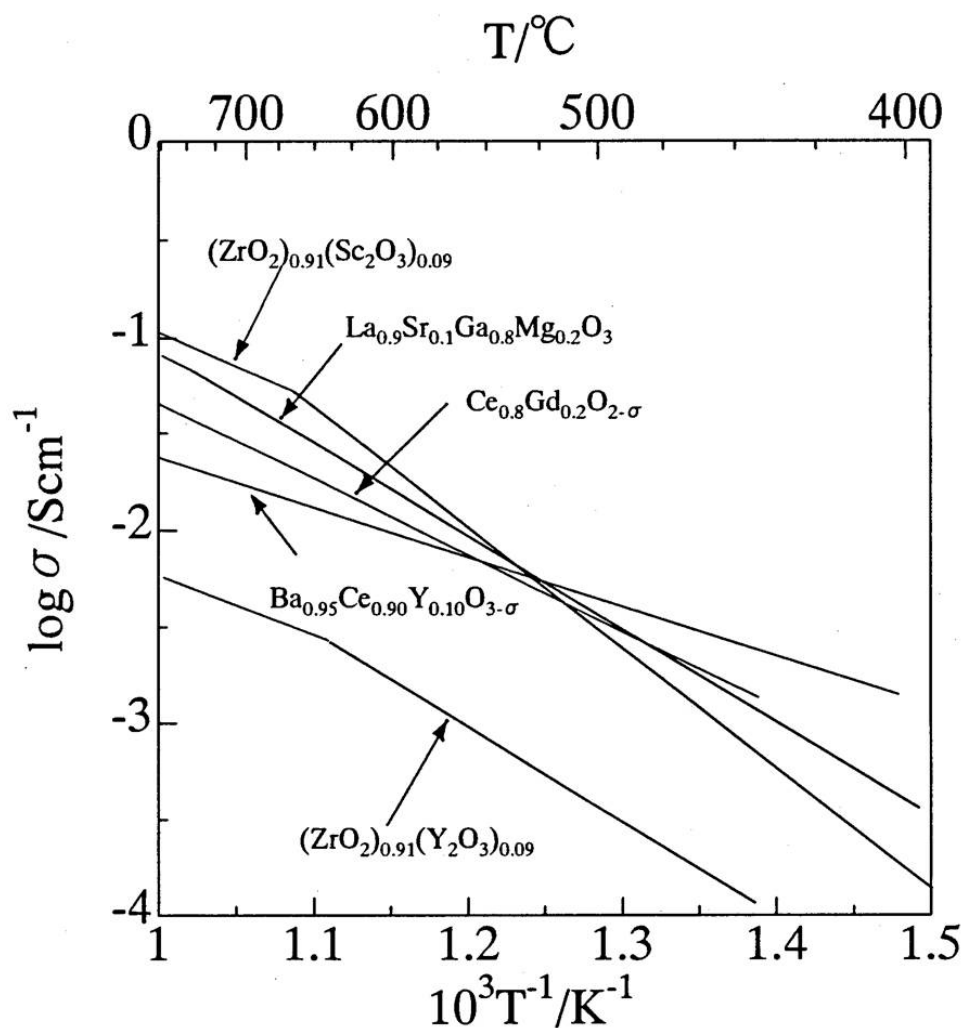


Figure 1.4. Temperature dependence of electrical conductivity for oxide ion conductors (low temperature range) [26].

### i) Stabilized zirconia

The most common solid electrolyte material used in solid oxide fuel cells is yttria-stabilized zirconia (YSZ). Yttria is added to stabilize the conductive cubic fluorite phase, as well as to increase the concentration of oxygen vacancies, and thus increasing the ionic conductivity. Figure 1.5 shows that the conductivity of YSZ increases for yttria additions of up to about 8 mole% and then decreases for higher yttria contents. The decrease at higher dopant contents is due to association of point defects, which leads to a reduction in defect mobility and thus conductivity [27].

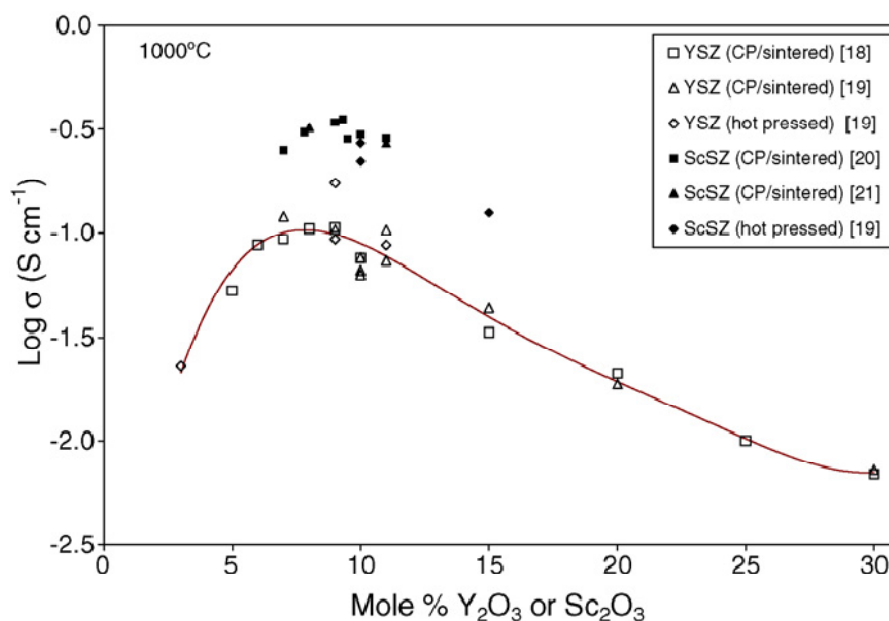


Figure 1.5. Conductivity of yttria and scandia stabilized zirconia in air at 1000°C [27 and references therein].

A promising, although less widely used, dopant for zirconia is scandia, which, as shown in figure 1.5, has a higher conductivity than YSZ. The higher conductivity of the scandia-stabilized zirconia (ScSZ) is attributed to the smaller mismatch in size between  $Zr^{4+}$  and  $Sc^{3+}$ , as compared to that between  $Zr^{4+}$  and  $Y^{3+}$ , leading to a smaller energy for defect association, which increases mobility and thus conductivity [28-31]. However, this material has not been used as an electrolyte in SOFC, because of high temperature reduces its stability and because of high cost of scandia.

## **ii) Doped ceria**

Gadolinia-doped ceria (CGO) have also attracted considerable interest as electrolyte materials for SOFC operating at intermediate temperature [32,33]. The major advantages of SOFC with  $Ce_{0.8}Gd_{0.2}O_{1.9-x}$  (CGO) electrolyte are (i) the four to five times higher ionic conductivity at intermediate operating temperatures compared with YSZ [34-36], and (ii) the reduced ohmic losses resulting in higher fuel cell power outputs [37]. One of the major disadvantages of CGO compared with YSZ is its mixed ionic-electronic conductivity, which becomes dominant especially for high fuel cell operating temperature between 800 and 1000°C. In this temperature regime, electronic leakage through the fuel cell electrolyte leads to short circuiting and decreased power performance [38].

Doped ceria is relatively unreactive towards potential electrode materials. At the present time reasonable performance has been reported

with Ni/ceria anodes and LSCF cathodes. Because doped ceria is only viable for operating temperatures below 600°C, it must be used in a supported thick-film form.

### iii) Strontium/magnesium-doped lanthanum gallate

The perovskite, LaGaO<sub>3</sub>, can be doped with strontium and magnesium, La<sub>1-x</sub>Sr<sub>x</sub>Ga<sub>1-y</sub>Mg<sub>y</sub>O<sub>3</sub> (LSGM), to produce a material with good low-temperature oxygen-ion conductivity [38]. The conductivity of LSGM is higher than those of YSZ and ScSZ and similar to that of CGO. However, LSGM does not have an easily reducible ion, like Ce<sup>4+</sup>, and thus is superior to CGO for use in low oxygen partial pressures. The conductivity of LSGM depends on dopant concentration and comparison of 27 different compositions indicated the maximum conductivity was for La<sub>0.8</sub>Sr<sub>0.2</sub>Ga<sub>0.85</sub>Mg<sub>0.15</sub>O<sub>3</sub> and La<sub>0.8</sub>Sr<sub>0.2</sub>Ga<sub>0.8</sub>Mg<sub>0.2</sub>O<sub>3</sub> [39].

One of the approaches to increasing the conductivity of LSGM is to add transition metal dopants, such as cobalt [40-44] and iron [40,41,45]. However, both dopants also decrease the hole conductivity, which is detrimental to fuel cell performance.

The reaction of LSGM with SOFC cathodes is different from that of zirconia or ceria, because most of the common cathode materials form the perovskite structure. Thus, rather than forming a separate phase, the interaction typically occurs through interdiffusion. For example, when used with a La<sub>1-x</sub>Sr<sub>x</sub>MnO<sub>3</sub> (LSM) cathode, some diffusion of manganese into

LSGM occurs [46]. In contrast, the most common anode material is the Ni/YSZ cermet, so interaction anode-electrolyte interaction is not a problem with YSZ electrolytes. However, for a LSGM electrolyte, a resistive phase can form between the LSGM and a Ni-containing anode [39].

#### **iv) Other electrolytes**

Other materials which possess the characteristics to be considered as solid electrolyte materials are currently investigated, some of them includes:

- $\delta$ -Bi<sub>2</sub>O<sub>3</sub> and Bi<sub>4</sub>V<sub>2</sub>O<sub>11</sub> based ceramics.
- Materials based on La<sub>2</sub>Mo<sub>2</sub>O<sub>9</sub> (LAMOX).
- Perovskite- and brownmillerite-like phases derived from Ba<sub>2</sub>In<sub>2</sub>O<sub>5</sub>.
- Perovskites based on LnBO<sub>3</sub> (B=Al, In, Sc, Y).
- Solid electrolytes with apatite structure (La<sub>10</sub>Si<sub>6</sub>O<sub>27</sub> or Nd<sub>10</sub>Si<sub>6</sub>O<sub>27</sub>).
- Pyrochlores and fluorite-type (Y, Nb, Zr)O<sub>2- $\delta$</sub> .

#### **1.2.4.2 Anode**

The function of the anode in SOFCs is to facilitate the oxidation of the fuel and the transport of electrons from the electrolyte to the fuel/electrode interface.

To minimize the polarization losses of the H<sub>2</sub> oxidation reaction, anode materials should meet the basic requirements of high electronic

conductivity, sufficient electrocatalytic activity for fuel oxidation reactions, chemically stable and thermally compatible with other cell components. In addition, it must allow diffusion of fuel gas to this interface and exhaust gases in high temperature reducing environment [47-49].

Porous Ni/YSZ cermet is currently the most common anode material for SOFC applications because of its low cost. It is also chemically stable in reducing atmospheres at high temperatures and its thermal expansion coefficient is close to that of YSZ-electrolyte. More importantly, the intrinsic charge transfer resistance that is associated with the electrocatalytic activity at Ni/YSZ boundary is low. More than 30%, by volume, of continuous porosity is required to facilitate the transport of reactant and product gases. Nickel serves as an excellent reforming catalyst for electrochemical oxidation of hydrogen. It also provides predominant electronic conductivity for anode. The YSZ constitutes a framework for the dispersion of Ni particles and acts as inhibitor for the coarsening of Ni powders during both consolidation and operation. Additionally, it offers a significant part of ionic contribution to the overall conductivity [2,50].

Ni/YSZ cermet is currently a preferred anode since, Ni and YSZ are essentially immiscible in each other and non-reactive over a very wide temperature. This enables the preparation of a NiO-YSZ composite via conventional sintering followed by reduction upon exposure to fuel gases. The subsequent development of a very fine microstructure can be maintained during service for relatively a long period of time [4].

The electrical conductivity of Ni/YSZ cermet is strongly dependent on its nickel content. The conductivity of the cermet as a function of the nickel content shows the S-shaped curve predicted by percolation theory (figure 1.6) [51-53]. Below this threshold, the cermet exhibits predominantly ionic conducting behaviour. Above 30 vol% nickel, the conductivity is about three-orders of magnitude higher, corresponding to a change in mechanism to electronic conduction through metallic phase. The percolation threshold is revealed to be influenced by many variables such as the porosity, pore size, size distribution and size of raw powders as well as contiguity of each constituent component. The electrical behaviour of Ni/YSZ cermet is, therefore, a strong function of these factors [54-56].

The disadvantages of the Ni/YSZ anode material are its poor redox stability, low tolerance to sulphur [57], carbon deposition when using hydrocarbon fuels and the tendency of nickel agglomeration after prolonged operation [58,59]. Especially, the low tolerance for carbon deposition makes this material inappropriate for operation with available hydrocarbon fuels [60-63]. Since nickel is an excellent catalyst for both steam reforming and hydrogen cracking, carbon deposition occurs rapidly when hydrocarbon was used as the fuel. The mechanism involves carbon chemisorption on the nickel surface, carbon dissolution into the bulk nickel, and precipitation of graphitic carbon from some facet of the nickel particle after it becomes supersaturated in carbon [64]. Unless sufficient amounts of steam are present along with the hydrocarbon to remove carbon from the nickel

surface at a rate faster than that of carbon dissolution and precipitation, the anode will be destroyed.

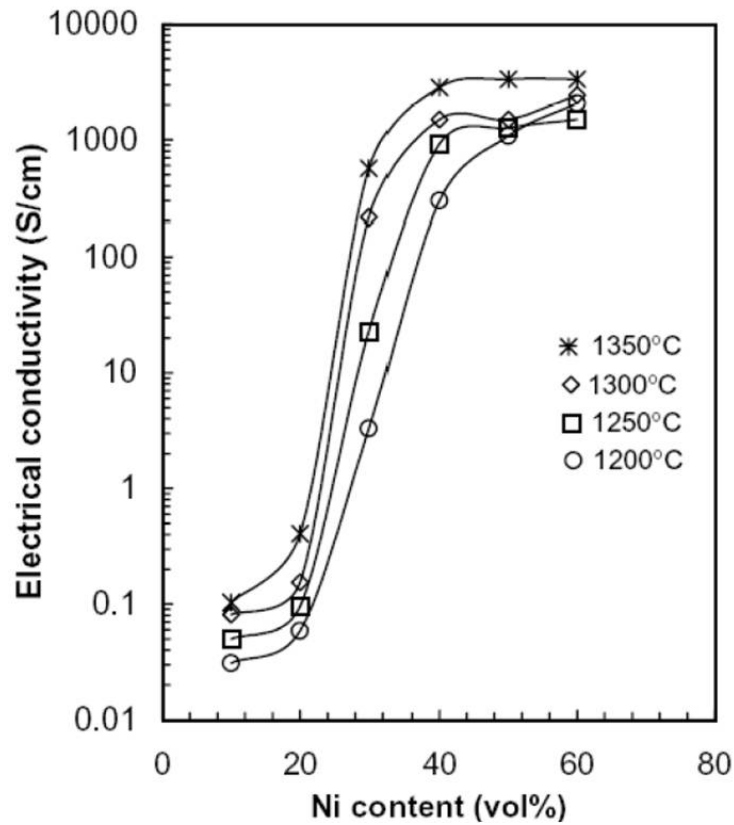


Figure 1.6. Variation of electrical conductivity measured at 1000°C as a function of nickel concentration of Ni/YSZ cermet fired at different temperatures [53].

The composition of the anode, particle sizes of the powders and the manufacturing method are crucial to achieving high electronic conductivity,

adequate ionic conductivity, and high activity for electrochemical reactions, reforming and shift reactions [65].

For the anode, there are also alternative materials under analysis [66], mainly including some fluorite (ceramics based on  $\text{CeO}_2$  [33,67] and  $\text{Bi}_2\text{O}_3$  [68]), perovskite ( $\text{La}_{0.75}\text{Sr}_{0.25}\text{Cr}_{0.5}\text{Mn}_{0.5}\text{O}_{3-\delta}$  (LSCM) [69],  $\text{La}_{0.8}\text{Sr}_{0.2}\text{Cr}_{0.97}\text{V}_{0.03}\text{O}_3$  (LSCV) [70], etc), tungsten bronze ( $\text{Sr}_{0.2}\text{Ba}_{0.4}\text{Ti}_{0.2}\text{Nb}_{0.8}\text{O}_3$ ) [71], and pyrochlore ( $\text{Gd}_2\text{Ti}_2\text{O}_7$  (GT) [72-74]) structure materials.

### 1.2.4.3 Cathode

The cathode is the material where pure oxygen or oxygen from air combining electrons externally from the cell, is reduced to oxygen ions. On the cathode, the oxygen reduction corresponds to the reaction 1-2.

Some characteristics needed for cathode materials include [75]:

- (1) High electronic conductivity.
- (2) A matched thermal expansion coefficient (TEC) and chemical compatibility with the electrolyte and interconnect materials.
- (3) Adequate porosity to allow gaseous oxygen to readily diffuse through the cathode to the cathode/electrolyte interface.
- (4) Stability under an oxidizing atmosphere during fabrication and operation.
- (5) High catalytic activity for the oxygen reduction reaction.
- (6) Low cost.

The electrochemical reactions are quite different from normal heterogeneous catalytic reaction in many aspects [67]. For instance, it is widely believed that the electrochemical reactions can only occur at the triple-phase boundary (TPB), which is defined as the confluence of sites where the oxygen ion conductor, electronic conductor, and the gas phase come in contact.

A schematic illustration of the region between the electrolyte and the cathode where the TPB exists is shown in figure 1.7. If there is a breakdown in connectivity in any one of the three phases, the reaction cannot occur [76].

- Triple-phase boundary (TPB)

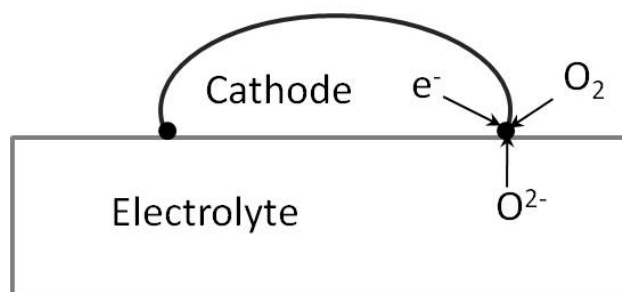


Figure 1.7. Schematic diagram showing the location of the triple-phase boundary (TPB) at cathode/electrolyte interface.

Among various cathode materials, lanthanum strontium manganite (LSM)-based perovskites are, till today, the most investigated cathode

materials for SOFCs. The sustained interest and enthusiasm about this material arises from the fact that LSM has distinctive advantages as cathode of high temperature SOFCs: its high electrical conductivity, high electrochemical activity for the O<sub>2</sub> reduction reaction, high thermal stability and compatibility with the common SOFC electrolytes of YSZ, GDC and LSGM at SOFC operating conditions.

The electronic conductivity of LSM increases approximately linearly with increasing Sr concentration up to a maximum around 50 mol% [77]. At high temperature, LaMnO<sub>3</sub> undergoes a solid-phase reaction with YSZ to form La<sub>2</sub>Zr<sub>2</sub>O<sub>7</sub> at the electrode/electrolyte interface [78,79-81]. A little amount of Sr substitution decreases the reactivity of LSM compound with YSZ. However, SrZrO<sub>3</sub> forms when Sr concentration is above about 30 mol% [81-84]. Therefore, a Sr content of 30 mol% is considered as optimal against the formation of unwanted electronically insulating phases.

Generally, the electrical properties of manganite-based perovskite compounds are not sufficient for operation at temperatures below 800°C. The absence of oxygen vacancies in LSM restricts the reduction of oxygen to the three-phase boundary regions. This limitation is the primary reason why LSM does not have acceptable performance at lower temperatures. Usually, two approaches have been taken to improve the performance of LSM cathodes so that they may be used at lower temperatures [85]. The first is to add a second ionically conducting phase to LSM and the second has been to replace La with other rare earth elements or dope LSM with a cation (such as, Co, Fe, or Ni) that promotes the formation of oxygen vacancies.

Increasing the electrode ionic conductivity, oxygen reduction becomes possible in a wider interface area around the TPB. Using a mixed ionic-electronic conductor (MIEC) cathode, the electrochemical reaction zone is enlarged over the entire cathode-gas interfacial area. Extending the active region, oxygen reduction kinetics is improved. In the case of a pure electronic conducting cathode material, the TPB can be increased adding an ionic conducting phase (usually YSZ) to form a porous composite microstructure (LSM/YSZ composite) [76].

Other cathode materials with mixed conductivity have been considered, such as (La, Sr)Co<sub>3</sub> (LSC) and (La, Sr)(Co, Fe)O<sub>3</sub> (LSF/LSCF) for low operating temperatures.

Usually, LSC cathodes display higher ionic and electronic conductivities than other cathode materials. Therefore, the use of cobalt-containing cathode materials should result in a decreased cathode polarization resistance. La<sub>1-x</sub>Sr<sub>x</sub>CoO<sub>3-δ</sub> has a marked electrode activity due to high oxygen diffusivity and high dissociation ability of oxygen molecules [86]. However, a large amount of cobalt results in an increased thermal expansion coefficient, which may result in a delamination at the cathode/electrolyte interface or cracking of the electrolyte [87].

LSF/LSCF cathodes have shown promising performance with respect to the power density and stability at 750°C [88-90]. In iron-based cathodes, reactivity with YSZ electrolyte is significantly reduced. In addition, TECs of the ferrite-perovskite are relatively close to those of the YSZ and CGO electrolyte.

#### **1.2.4.4 Interconnectors/current collectors**

To enable higher voltage outputs (and, thus, power outputs) the single cell must be stacked into multi-cellular units. Stacking of the single cells is carried out using an electronically conducting interconnecting/current-collector for series or parallel connections. Depending of the SOFC design, the interconnect must be both chemically and physically stable in reducing and oxidizing environments, have good electronic conductivity, have sufficient strength to support other cells, and be easily fabricated into the required configuration [91]. The literature shows many forms of the interconnect/current collector as determined by the cell design. These vary from metal wires connected with metal gas separator plates [92,93], Ni felts used in combination with metal plates [94], Ni/Cr wires [95], doped LaCrO<sub>3</sub> [96] and chromia forming metal plates [97]. Of these, doped LaCrO<sub>3</sub> and chromia forming alloys (or a combination) are the most widely employed [96]. However, the evaporation of chromium from the surface of the metal interconnect on the cathode side have been shown to be detrimental to the cell performance. The chromium evaporation can be suppressed, however, by surface treatment of the alloy separator [98,99]. Furthermore, the coating of the metal interconnect with a perovskite has been shown to decrease the contact resistance and improve the stability of cell performance over time [95,99-101].

The design and material component of the interconnect are highly dependent on its application with respect to the type of SOFC. For example,

interconnects have been designed with reduced thermal stresses which overcome problems associated with thermal cycling, mismatches in thermal expansion coefficient and improved electrical contact [102].

### **1.2.5 SOFCs design**

For the scope of this thesis a special attention will be paid on the description of the tubular design and more specifically on the micro-tubular architecture.

#### **1.2.5.1 *Basics***

At present, there are many possibilities of SOFC geometric configurations. The two most common designs of SOFCs are the planar and the tubular. Each design offer advantages and drawbacks depending of the application requirements. Both planar and tubular single cells SOFC are classified based on its support-configuration into two broad categories [103]:

- 1) Self-supporting.- One of the cell components (often the thickest layer) acts as the cell structural support. Thus, single cells can be designed as electrolyte, anode or cathode-supported.

- 2) External-supporting.- The single cell is configured as thin layers on the interconnect or a porous substrate.

The various cell support-configurations for SOFC are schematically shown in figure 1.8.

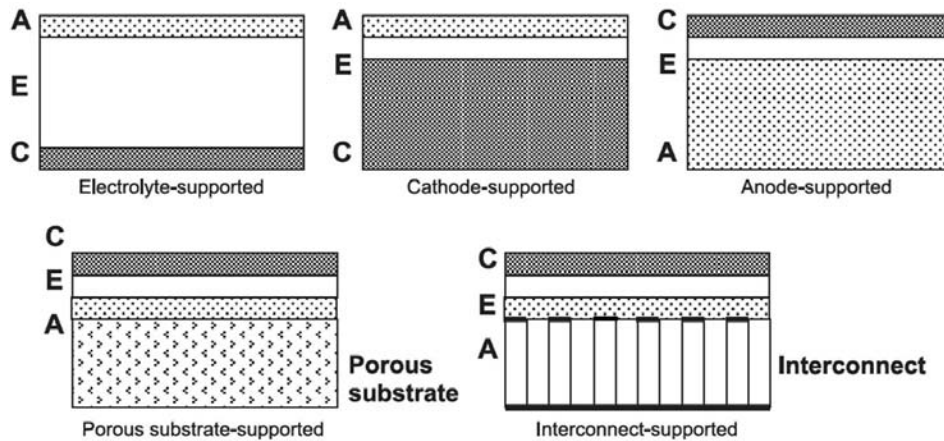


Figure 1.8. Schematic diagram of the SOFC single cell support-configurations; anode (A), cathode (C), electrolyte (E) [103].

### 1.2.5.2 Planar design

In the planar design configuration, the single cell is configured as flat plates which are connected in electrical series. Common plate shapes are rectangular (square) or circular. Figure 1.9 shows the planar SOFC design.

Planar SOFC design has a low physical component volume profile and short current path between single cells, which is perpendicular to the cell

plane. Relatively low ohmic losses in the whole stack can be reached. Consequently, specific power densities are higher in planar cells than in tubular ones. However, gas tight and electrically insulating seals are required to separate the interior of the manifold and the outside environment. Therefore, sealing becomes quite difficult, especially at the high temperatures and the extreme operating conditions of a SOFC [5,104].

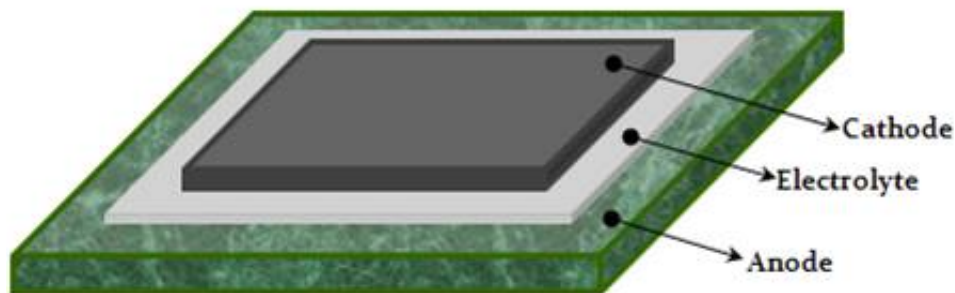


Figure 1.9. Schematic diagram of the planar SOFC design.

### ***1.2.5.3 Tubular design***

In the tubular design, the cell components are deposited in the form of thin layers on a cylindrical tube which can be one or both open ends depending of processing method used to fabricate it. Figure 1.10 shows the tubular SOFC design.

In comparison with planar design, the tubular design has many desirable characteristics, including high thermo-mechanical properties, simple sealing

requirements, rapid start-up/shut-down time, good thermal shock resistance, and excellent power cycling [105-107].

Disadvantages of the tubular design include a higher cost of manufacture and longer current paths which results in significant ohmic losses.

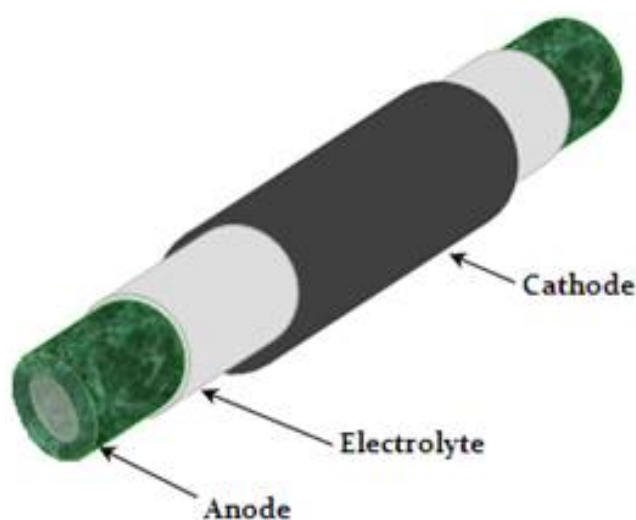


Figure 1.10. Schematic diagram of the tubular SOFC design.

One of the most prominent tubular SOFC design was developed for Westinghouse Electric Corporation (now Siemens Westinghouse Power Corporation). It originally consisted of an extruded porous tube made of calcia-stabilized zirconia as structural support and as a porous media to the passage of air to the cathode. Subsequent improvements in this design were the reduction in the wall thickness of the porous support and later replaced by a doped  $\text{LaMnO}_3$  tube which worked as the cathode electrode. The

dimensions of the cells were about 30 cm in length and 1.6 cm in diameter, but these were also adjusted to 150 and 2.2 cm, respectively. On this last configuration, a long term operation over 30,000 h with a power density of about 0.25-0.3 W/cm<sup>2</sup> at 1000°C was successfully conducted (less than 0.1% per 1000 h performance degradation). However its size is too large to be considered for compact SOFC applications [6,7,91].

Efforts have been done in recent years to enhance the overall performance of tubular cells. The much longer current path in a tubular SOFC than in planar cell becomes one of the most concerned issues.

At present, improvements of tubular SOFC are progressing towards development mini- or micro-tubular cells aimed at the portable and mobile power generation devices market [108].

#### ***1.2.5.4 Miniaturization of SOFC***

Because direct conversion of chemical energy into electrical energy does not suffer from the thermodynamics efficiency restrictions of conventional thermo-mechanical energy production methods, in principle it is possible to scale down to the micrometre level the size of the whole device without affecting the SOFC overall efficiency [109].

The power density of tubular cells scales with the reciprocal of tube diameter which is not possible with planar SOFC design. Therefore, a 2 mm diameter micro-tubular SOFC could provide ten times more power per stack volume than a 20 mm diameter tubular cell. Another order of magnitude

could be achieved by going to 0.2 mm diameter tubes, but this becomes difficult because the connections are then more numerous and problematic to apply. The most significant issue in micro-tubular cells is connecting the metal current collector inside of a very small-diameter tube [6].

Several studies showed that the thermo-mechanical properties are improved by using small-sized tubular SOFCs which leads to the quick start-up time and high thermo-cycling resistance. Furthermore, small SOFC size can bring a substantial increase in the net electrode area per unit of volume, resulting in an enhancement of volumetric power density which enables the realization of SOFC systems for portable devices and auxiliary power units for automotive [110,111]. Therefore, micro-tubular SOFC have been drawn considerable interest and attention recently.

## **1.2.6 Micro-tubular SOFC**

### ***1.2.6.1 Fabrication techniques for micro-tubular SOFC***

The demonstration in the early '90s of the extrusion of thin YSZ ceramic tubes, with wall thicknesses of between 100 and 200  $\mu\text{m}$ , which could be used as the electrolyte for SOFC operation, opened up the micro-tubular SOFC research field [112].

Since then, micro-tubular cells have been constructed into anode-supported [113-118], cathode-supported [119-121], or electrolyte-supported configurations [105,122].

Currently, the most commonly used cell architecture for the micro-tubular SOFCs is the anode supported micro-tubular SOFC. This is because of the difficult in preparing a dense electrolyte layer on a porous cathode support surface (mainly for the reactivity of them during sintering) and to the relatively high ohmic losses in the electrolyte-supported cells [123].

There are many techniques and methods for the fabrication of micro-tubular SOFCs. These are carefully selected according to the design, materials, configuration, etc. The techniques more frequently used for the production of micro-tubular cells are:

#### **a) Extrusion/co-extrusion**

Plastic extrusion is the main method for producing micro-tubular cells. This is an economic process, which can lead to high-quality ceramics with good strength and Weibull modulus. Additionally, the use of co-extrusion has many advantages over single layer extrusion methods, including minimizing fabrication steps and time, hence decreasing production cost. Co-extrusion has the promising possibility that could produce one-step processing of cells [124]. The most typical method for the production of micro-tubular cells involves the extrusion of the support tube and its

subsequent coating with the other components by using slurry coating techniques.

### **b) Dip coating**

The dip coating process is widely used to produce thin ceramics coating on a variety of substrate materials. In this process, the substrate is partially or fully immersed in the precursor solution and then withdrawn from the liquid. In comparison to other fabrication methods, the dip-coating process is an easy and low cost method for preparing thin films and makes the process very attractive and economical for potential large-scale commercial fabrication [125,126]. The layer thickness is defined by the suspension conditions and the time and speed for the dipping. However, the drop geometry limits its application in long tubes. The dip coating technique is generally used to deposit the electrolyte and the outer electrode on the support tubes.

### **c) Electrophoretic deposition (EPD)**

EPD is a simple and fast deposition technique to produce thin films from colloidal particles. Powder particles are charged and suspended in a colloidal system. Under the forces of an externally applied electric field, the particles move to the substrate surface and coagulate in a dense layer [125].

Additionally, the EPD technique offers the possibility of multi-layered arrangement before sintering.

#### **d) Spray coating**

This method involve the generation of a fine aerosol of a colloidal suspension, which is then directed towards the substrate surface. Moreover, spray coating is very suitable for complex shapes and mass production. Heat and an external electric field are variations for this method [125,127]. This technique is commonly used for coating the sintered half-cells with the last electrode layer.

#### **e) Brush painting**

The brush painting is a technique in which a suspension is applied directly on the substrate surface with a brush. This technique is also easy and economic coating technique, but the thickness and composition of the layer deposited are poorly controlled. Although this technique is regularly employed in the production of micro-tubular SOFCs its use is only for the outer electrode.

### ***1.2.6.2 Current status of the performance of micro-tubular SOFCs***

In recent years many efforts have been doing to improve the overall performance of micro-tubular cells by many groups around the world. Different issues have been concerned such as develop new materials, alternative processing techniques, novel cell designs, and so on. The progress of micro-tubular SOFC has been reviewed in very recent papers [109,112, 124].

The main parameter to evaluate the performance of the cells produced in this work was based on the power density achieved in each micro-tubular cell configuration. Therefore, an overview of the performance of micro-tubular SOFCs achieved by diverse current research groups is presented.

One of the most important research groups who have contributed to the development of micro-tubular cells in recent years has been the National Institute of Advanced Industrial Science and Technology (AIST) jointly with the Fine Ceramics Research Association (FCRA) of Nagoya, Japan.

Under the project of “Advanced ceramic reactor”, Suzuki et al. [113] have developed a micro-tubular cell of 1.6 mm in diameter and 10 mm in length (cathode length of 7 mm), which consists of NiO-Gd doped ceria (GDC) as anode (support tube), GDC as electrolyte and (La, Sr)(Fe, Co)O<sub>3</sub> (LSCF)-GDC as cathode. The power density of single micro-tubular cell was estimated to be 400, 857 and 1000 mW/cm<sup>2</sup> at 500, 550 and 570°C,

respectively. The fabrication of bundles composed of 25 cells was also developed.

In another study by Suzuki et al. [117] a stack consisted of 9 cells (three bundles in series connection) of 2 mm in diameter was produced. The material used for the production of these anode-supported cells was based on the NiO-GDC/GDC/LSCF-GDC configuration. The total electrode area of the stack was  $5.65 \text{ cm}^2$  and thus, the power density of  $180 \text{ mW/cm}^2$  was obtained at  $484^\circ\text{C}$ . The relative low performance was attributed to high interfacial resistances and low sealing technology.

Fabrication of needle-type micro SOFC and its potentially bundling has been also studied by Suzuki et al. [114]. NiO-GDC/GDC/LSCF configuration was used to produce cells with 0.4 mm in diameter. The power density of the cell was estimated from the area of cathode ( $0.06 \text{ cm}^2$ ), which were 80, 160 and  $300 \text{ mW/cm}^2$  with wet  $\text{H}_2$  fuel at 450, 500 and  $550^\circ\text{C}$ , respectively.

More recently, Suzuki et al. [128] produced a micro-module using three micro-SOFC bundles (connected in series) which consisted of five anode-supported micro-tubular SOFC (connected in parallel) of 0.8 mm diameter and porous cathode matrices. The materials used were the NiO-GDC/GDC/LSCF configuration for single cells and LSCF as porous cathode matrix. The total electrode area of the cells was  $3.77 \text{ cm}^2$  and therefore, a maximum power density of 130, 240 and  $370 \text{ mW/cm}^2$  was obtained at 450, 500, and  $550^\circ\text{C}$ , respectively. Considering that the volume of the module

was about  $0.6 \text{ cm}^3$  the maximum volumetric power density were 830, 1500, and  $2330 \text{ mW/cm}^3$  at 450, 500, and  $550^\circ\text{C}$ , respectively.

Funahashi et al. [115] showed a significant improvement in the performance of its micro-tubular cells increasing the porosity in the anode from 20 to 40 vol%. The cells of 2 mm in diameter and 15 mm in length with cathode length of 6 mm, whose effective cell area was  $0.38 \text{ cm}^2$  were fabricated using NiO-GDC as anode, GDC as electrolyte and LSCF as cathode. The maximum output power density of single cells at  $550^\circ\text{C}$  was improved from 280 to  $460 \text{ mW/cm}^2$ . Fabrication technology to integrate 36 micro-tubular cells in a cathode matrix bundle of  $3 \times 3 \times 3 \text{ cm}$  was also studied.

Micro-tubular solid-oxide fuel cell consisting of a  $10 \text{ }\mu\text{m}$  thick ScSZ electrolyte on a support (NiO/ScSC) anode with a GDC buffer-layer and a LSCF/GDC functional cathode has been developed for intermediate temperature by Liu et al. [129]. The complete cells (1.8 mm in diameter and cathode length of 2 cm) were impregnated with Ag by immersion into a solution containing  $\text{AgNO}_3$ . The peak power densities of cell without impregnation were significantly improved from 110, 310 and  $540 \text{ mW/cm}^2$  to 490, 980 and  $1060 \text{ mW/cm}^2$  at 550, 600 and  $650^\circ\text{C}$ , respectively, after Ag impregnation.

The influence of tube length on the micro-tubular cell performance was also analysed by Liu et al. [119]. For the production of the cells a GDC layer was deposited on a cathode supported extruded tubes based LSCF-GDC. Next, the anode based NiO-GDC was applied by dip coating on the

sintered tubes to complete the cell. In this analysis, the power density of cells with different length as 1.5 and 2 cm was practically measured and compared. The effective reactive anode areas for the cells with tube length of 1.5 and 2cm were 0.07 and 0.22 cm<sup>2</sup>, respectively. A decrease in the maximum power density was noticeable with increasing the tube length. The power output achieved at 500, 550 and 600°C was 110, 130 and 160 mW/cm<sup>2</sup> for the 1.5 cm cell and 30, 49 and 90 mW/cm<sup>2</sup> for the 2 cm cell. The results clearly suggested that the cell performance was strongly limited by the tube length due to the low effectiveness of the current collector used for the cathode support.

A micro-tubular cell composed of a dense GDC as electrolyte and a porous LSCF-GDC as cathode deposited on a NiO-GDC anode support were produced and tested by Yamaguchi et al. [110]. The prepared tubular cell of 1.5 mm diameter and a length of 15 mm, with an active cathode length of 6.3 mm, present an active cathode area of 0.29 cm<sup>2</sup>. The peak power densities of 100, 200 and 400 mW/cm<sup>2</sup> were achieved at 450, 500 and 550°C, respectively, in wet H<sub>2</sub> fuel flow.

In another study by Yamaguchi et al. [130], a cathode supported micro-tubular of 1.6 mm in diameter and 20 mm in length were produced and tested in a wide range of temperatures. Cathode tube (LSM) was uniaxially extruded and coated with GDC and ScSZ as interlayer and electrolyte, respectively. The anode slurry based NiO-GDC was applied to sintered tubes to complete the cells. The anode active length of cells was 10 mm whose active electrode area is 0.5 cm<sup>2</sup>. The maximum power densities were

4.1, 8.8, 16.6, 35.9, 67.3, 116.5 and 197.2 mW/cm<sup>2</sup> at 450, 500, 550, 600, 650, 700 and 750°C, respectively, using wet H<sub>2</sub> (3% H<sub>2</sub>O) as fuel and O<sub>2</sub> as oxidant. In addition, the LSM-supported small SOFC showed sufficient durability to permit a rapid start-up operation with a heating rate of 60 °C/min.

In a recent study developed in the School of Mines at Colorado in USA, Sin et al. [131] produced and tested micro-tubular cells with an outside diameter of 1.6 mm and length of 12 mm. The anode-supported cells were produced using traditional extrusion and dip coating techniques with a NiO-GDC/GDC/LSCF configuration. The maximum power densities obtained were 263, 518, and 1310 mW/cm<sup>2</sup> at 450, 500, and 550°C, respectively.

In an approach proposed by the University of Science and Technology of China, Yang et al. [132] developed another anode-supported micro-tubular cell with a NiO-YSZ/YSZ/LSM configuration. The dimensions of the cell were 1.7 mm in diameter and 10 cm in length with a cathode length of 1.18 cm whose active cathode area was 0.63 cm<sup>2</sup>. The thickness of the YSZ electrolyte was about 12 μm and the maximum power densities reach were 124, 284 and 377 mW/cm<sup>2</sup> at 600, 700 and 800°C, respectively, using wet H<sub>2</sub> as fuel and static air as oxidant gas.

The production of co-extruded electrolyte-anode hollow fibre (HFs) has been studied by Droushiotis et al. [133] at the Imperial College London, in UK. NiO-CGO/CGO dual-layer HF was fabricated in a single-step co-extrusion and co-sintering process. LSCF-CGO cathode layer was then deposited by slurry coating onto the dual-layer HF to complete the cell. The

outer diameter of the whole dual layer HF was about 1.4 mm distributed with 220 and 80  $\mu\text{m}$  for the anode and electrolyte, respectively. The maximum power densities achieved were 42 and 80  $\text{mW}/\text{cm}^2$  at 450°C and 550°C, respectively, with fluxes of hydrogen for anode and air for cathode. Optimization of the cathode deposition and development of an improved current collection method were suggested to improve the performance of cells.

Almost one year later Droushiotis et al. [134] reported significant performance improvements for the HF cells achieved by modification of anode and cathode porosities, anode current collection design and cathode electronic conductivities. The materials and size of the half-cells for this study were the same than the previous analysis, but in this case the cathode consisted of a LSCF-CGO (50/50) functional layer followed by a pure LSCF layer to enhance the electronic conductivity. Although the cathode active length for both studies was 20 mm only 10 mm were used for the current collection. The improved HF cells produced maximum power densities of about 118 and 586  $\text{mW}/\text{cm}^2$  at 450 and 570°C, respectively.

A different processing procedure using electrophoretic deposition was proposed by the Alberta Research Council in Canada. Micro-tubular cells produced with EPD were produced and tested by Sarkar et al. [135]. NiO-YSZ cermets with coarse and fine NiO particles were used for anode and anode functional layer, respectively. The last layer deposited with EPD was a fine YSZ electrolyte layer. After the co-sintering of half of cells at 1400°C for 4 h the second electrode was applied by brush painting, this time a

compound of LSM/YSZ (50/50) and LSM pure were used as cathode functional layer and cathode, respectively. Cell with less than 2 mm in diameter and 2 cm of cathode length showed a maximum power density of 530 mW/cm<sup>2</sup> at 800°C. Later, these cells were modified with a Sm<sub>0.6</sub>Sr<sub>0.4</sub>CoO<sub>3-δ</sub> (SSC) as cathode material and the power density was enhanced to 742 mW/cm<sup>2</sup> at 650°C using hydrogen and air as combustible and oxidant gases, respectively.

In spite of the satisfactory performances in micro-tubular SOFCs achieved by many researchers one of the unsolved issues for such micro-tubular SOFCs is the ohmic loss when collecting the electrical current.

For further development in the performance of the micro-tubular SOFCs (single cell and stacks), a more efficient current collection mode need to be developed. However, the current collection becomes much more difficult when the diameter of tube is scaled down, especially within the inner electrode. Therefore, many alternative configurations have been proposed to increase the effectiveness of current collectors in micro-tubular SOFC.

### **1.2.7 Methods of current collection in tubular/micro-tubular SOFCs**

It is generally recognized that one of the main disadvantages of the micro-tubular SOFCs is the high ohmic loss caused by the long current path (the way by which the electrons reach the surface of the current collector)

distinctive of the tubular geometry. It has been concluded by many studies that increasing the contact area between the electrode and the current collector the ohmic loss is decreased as effect of shorter current paths [136-138]. In the case of the outer electrode this is relatively easy to solve due to its exposed surface area (most groups generally use a winding of silver around the whole area), but this becomes much more difficult for the inner electrode where almost all the surface area available for the electric connections is located into the tube/micro-tube. Hence, more attention has been paid to improve the current collection from the inner tube; some configurations are reviewed in this section.

In order to compare the effect of the current collector configuration on the micro-tubular cells their respective current path is also schemed. For convention, the current path flow direction described in this thesis corresponds to the conventional notation (from positive to negative terminals) and not to the proper electron current flow direction (from negative to positive terminals). Figure 1.11 shows the conventional and the electron current flow directions. It is important notice that the current path defined by a specific current collection configuration is not dependent of the current flow direction.

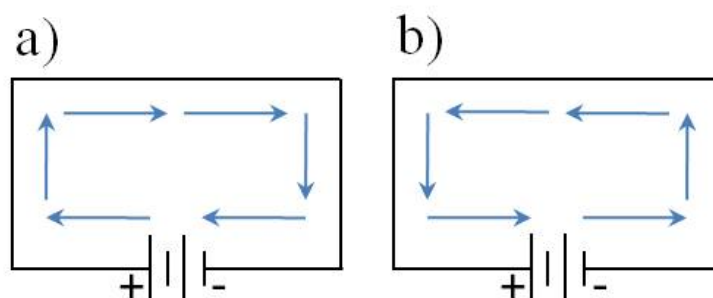


Figure 1.11. Schematic diagram of the conventional (a); and electron current flow (b) notation.

### 1.2.7.1 *Current collector placed along the cell*

This is the configuration which offers more possible combinations for the current collection in tubular/micro-tubular cells.

The first method described regards to the tubular cell produced by Siemens Westinghouse (Figure 1.12). In this method cell to cell contact is made along the cell using a nickel felt along the cell. Thus, current flow through the support electrode cathode is ideally circumferential (radial direction). In this current collector configuration a significant active area of the cell is sacrificed for the interconnector strip. Furthermore, long current paths are clearly seen. This current collection method is restrictive to one-closed end tubular cells of some centimetres in diameter. The fabrication involves high cost deposition techniques but offer an easy way for cell series interconnection. In general, this current collection mode is not attractive for micro-tubular cells due to the difficult fabrication process.

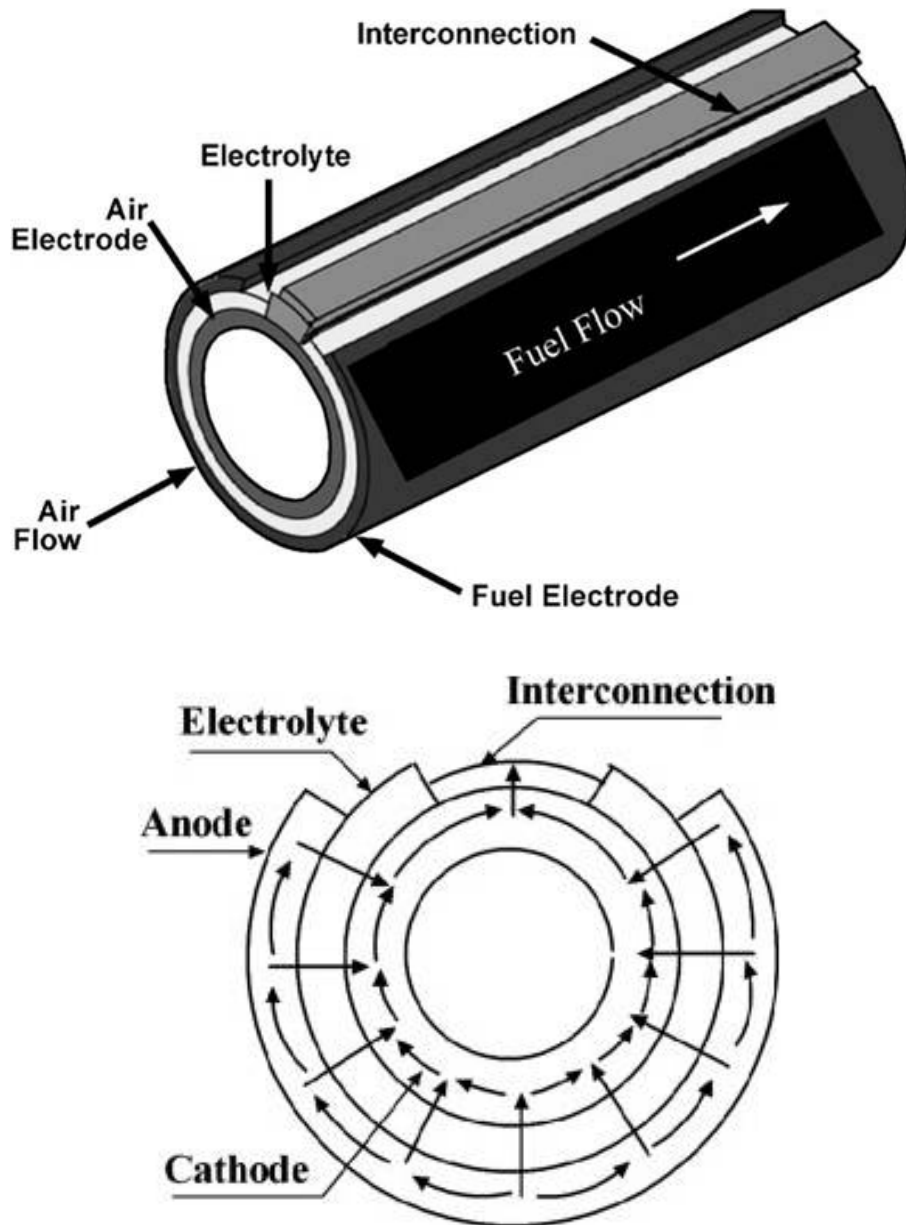


Figure 1.12. Schematic diagram of a tubular cell and current path with Siemens cells configuration [7,19].

In figure 1.13 a current collection configuration in which a straight metal wire is inserted into the tube to make contact with the electrode is shown.

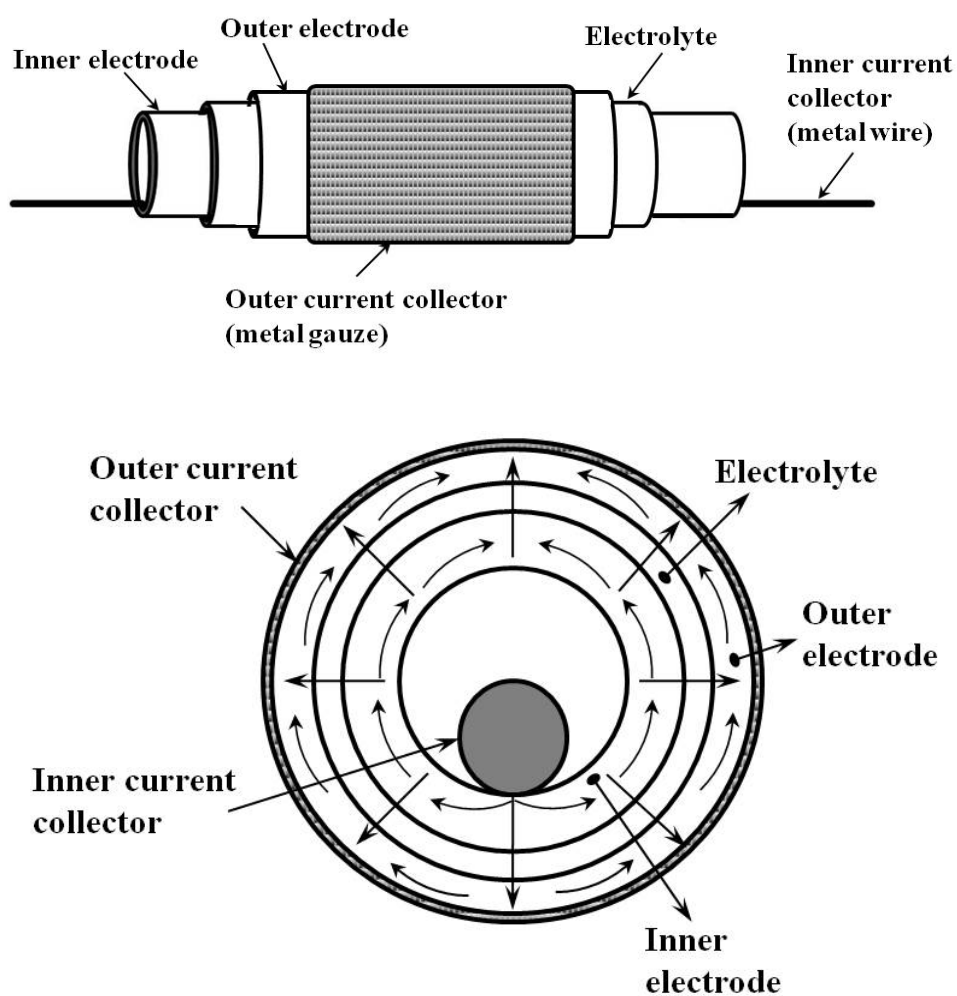


Figure 1.13. Schematic diagram of a tubular cell and current path with a straight metal wire as current collector.

The straight wire configuration is a relatively easy and effective current collection configuration for micro-tubular cells but the inner channel may be compromised. This configuration is mainly used in cell with both open ends [91,102,105,139]. In this case, the current path along the circumference (axial direction) is divided in two. The low electric contact between the inner electrode and the metal wire cause high ohmic losses, which in addition to the longer current paths reduce the overall performance of the cell. From this configuration many variations have been proposed. Materials such as springs, pastes and metallic wool are employed as substitutes for the straight wire. These configurations have increased the electric contact between the inner electrode and current collector but the channel for flux of gases is significantly decreased. In addition, complex assembly process is evident when the diameter of tubes is scaled down.

Figure 1.14 shows a tubular cell with a current collector as spring coil geometry. In this configuration the current collector is disposed concentrically within the inner electrode such that when sprung back to its normal state during assembly, the spring current collector is forced into firm uniform tangential electrical contact with the inner surface of the inner electrode [140].

As a result of a shorter current path this current collector mode is more effective than the previous case. Although the current path in the radial direction seems linear the current path in the axial direction is divided into the number of coils in contact with the inner electrode (figure 1.15).

Despite the difficulties during assembly satisfactory results have been reported by using this current collection mode in micro-tubular cells [133].

The current path in the case of pastes and metallic wool are slightly shorter than the spring coil configuration due to the homogeneous electric contact along the inner diameter of the tube. On the other hand, the porosity of the electrode and the volume for the flux of gases are decreased. High performances have been achieved using these configurations in micro-tubular cells [131,134].

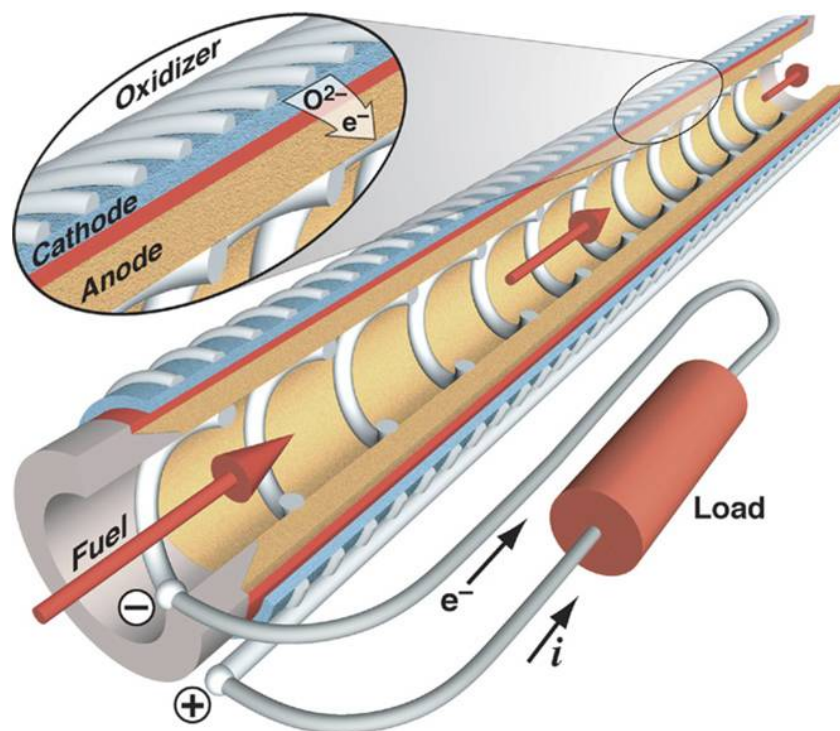


Figure 1.14. Schematic diagram of a tubular cell with a spring coil as current collector [141].

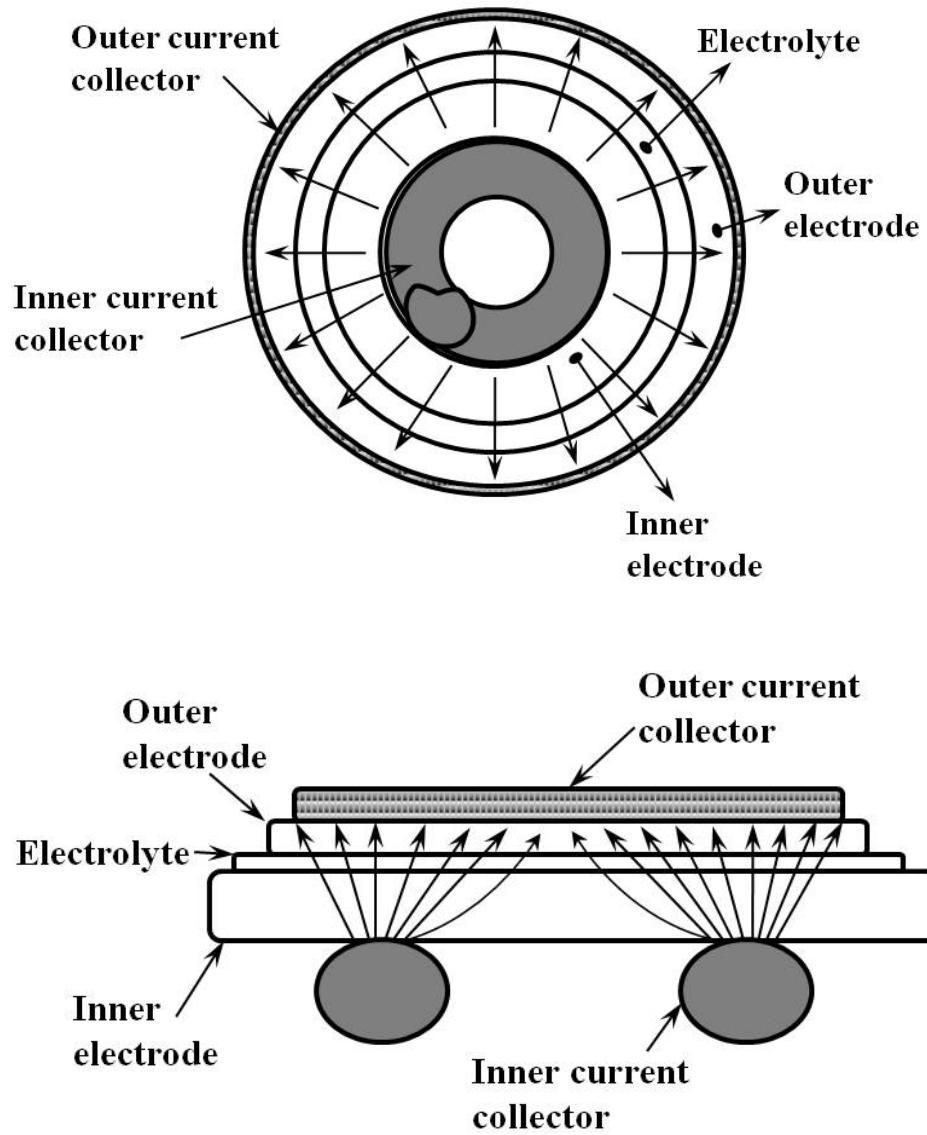


Figure 1.15. Schematic diagram of the current path in radial and axial direction with a spring coil as current collector.

### **1.2.7.2 *Current collector placed at one/two ends***

Currently, this is the most frequently method used to connect single and stacks micro-tubular SOFCs.

In this method wires are well wound and fixed with a metallic paste (usually silver paste) around the outside of one or two exposed ends of the inner electrode. Collection from the two ends brings the same benefits than those mentioned in the straight wire inserted into the tube, but in this case ohmic losses are caused by longer current paths in the axial direction (figure 1.16).

The main advantages of this current collector method are an easy assembly process and a gas flux channel without obstructions. On the contrary, a gradual loss of electric contact due to a rapid degradation of the paste occurs at high temperatures. Moreover, studies have shown that the efficiency of this method is strongly dependent of the tube length due to an increasing ohmic resistance [136,137].

Following the same principle than show in figure 1.16 a different version of the current collection at ends was proposed using a planar multi-cells array which connects in series tubular SOFCs. The interconnector and the multi cell-stack array used in this method are shown in figure 1.17. This system was developed for a 40 cell-stack with tubular cells of 1.32 cm in diameter [118].

The main benefit of this design is the elimination of wires in the cells when stacking. Conversely, longer current paths are recognized due to the

current collection from single terminals at each electrode. Moreover, the interconnectors are joined to the single cells using an arduous brazing technique at high temperatures. Currently, this method is not feasible for tubes in millimetre range.

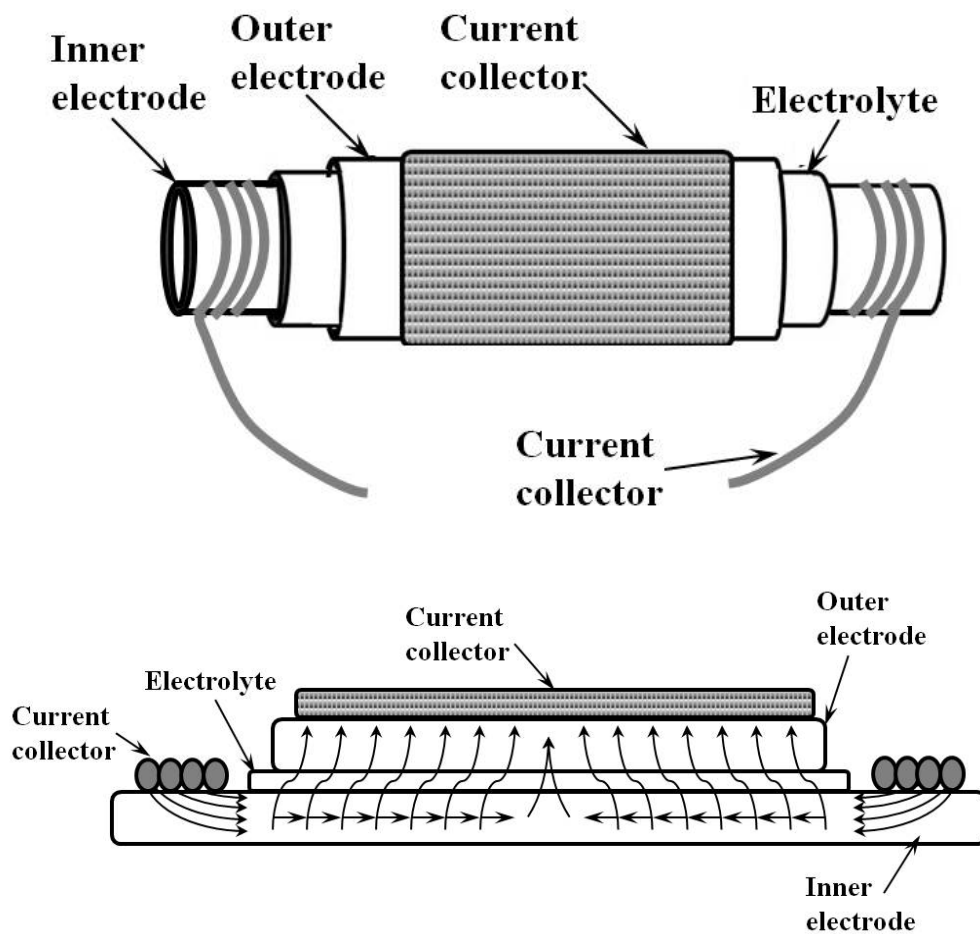


Figure 1.16. Schematic diagram of a tubular cell and current path with the current collector wound at both ends.

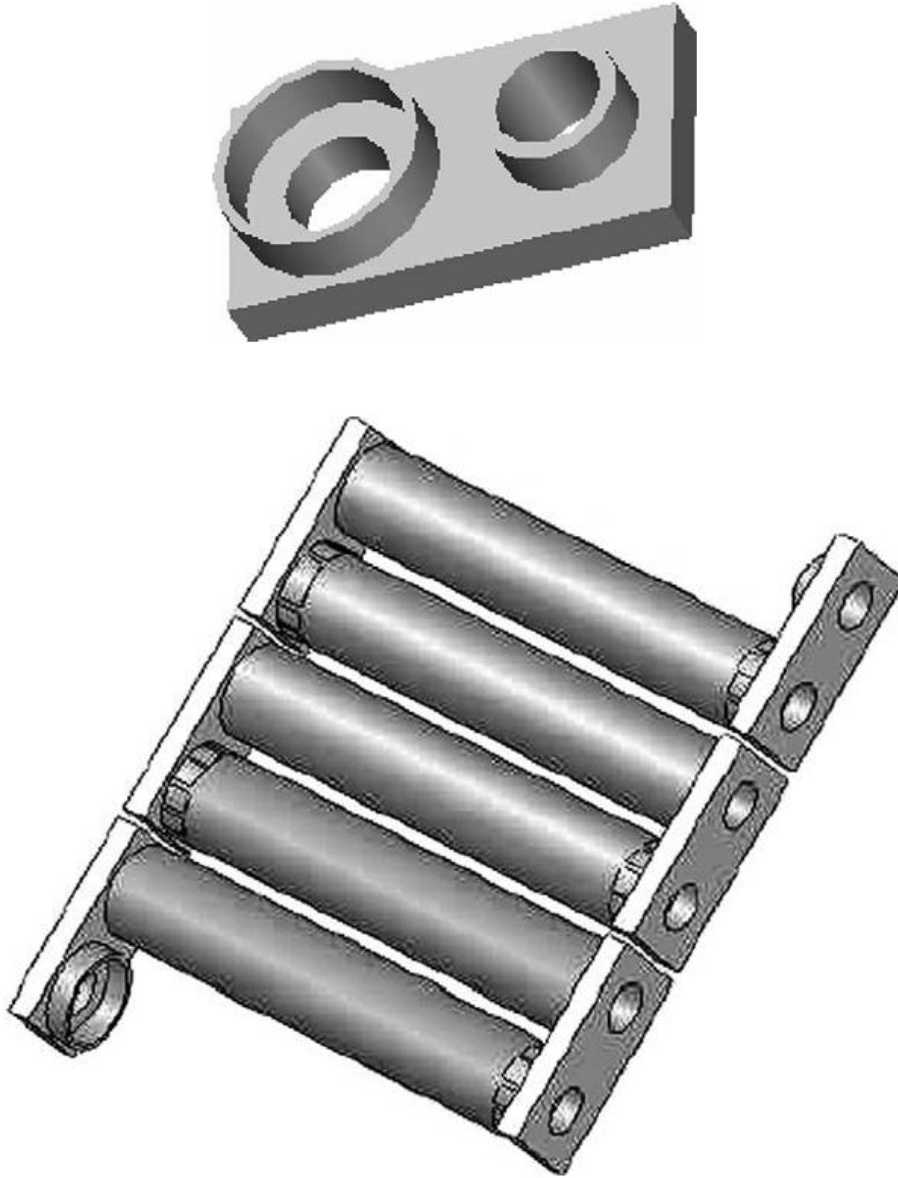


Figure 1.17. Schematic diagram of planar multi-cell array with interconnectors at ends [118].

## **1.3 Aim of the Thesis**

The present research work is focused on the development of an alternative method of current collection for micro-tubular SOFCs. Aspects such as well defined geometry, good reproducibility and high power density represent the main concerns.

As mentioned in previous sections, many current methods offer advantages and drawbacks when collecting current from the inner electrode. The current collection method described in this thesis is addressed to the reduction of the longer current paths in tubular cells. Additionally, a feasible and effective way to integrate the current collector into the inner electrode during the cell production process is presented.

The most important parameters in the design, processing and characterization of the current collector-supported micro-tubular cells produced are analysed and discussed in the subsequent chapters.

# **2. Experimental Procedure**

---

The experimental procedure followed for the production and characterization of micro-tubular cells is reported in this section. The techniques and methodology are listed according to the experimental progressive order show in figure 2.1.

## **2.1 Cell Supports**

The devices described in this thesis are fabricated using a current collector as support. The design of the supports is based on the coiling of a metal wire along of a sacrificial inner core which for the base case is directly used as support. Many aspects have been considered for the design of the cell supports such as: the selection of the sacrificial inner core material, diameter and length of the supports, material and diameter of the wire, number of turns along the length, cell configuration and deposition technique.

## 2 – Experimental Procedure

---

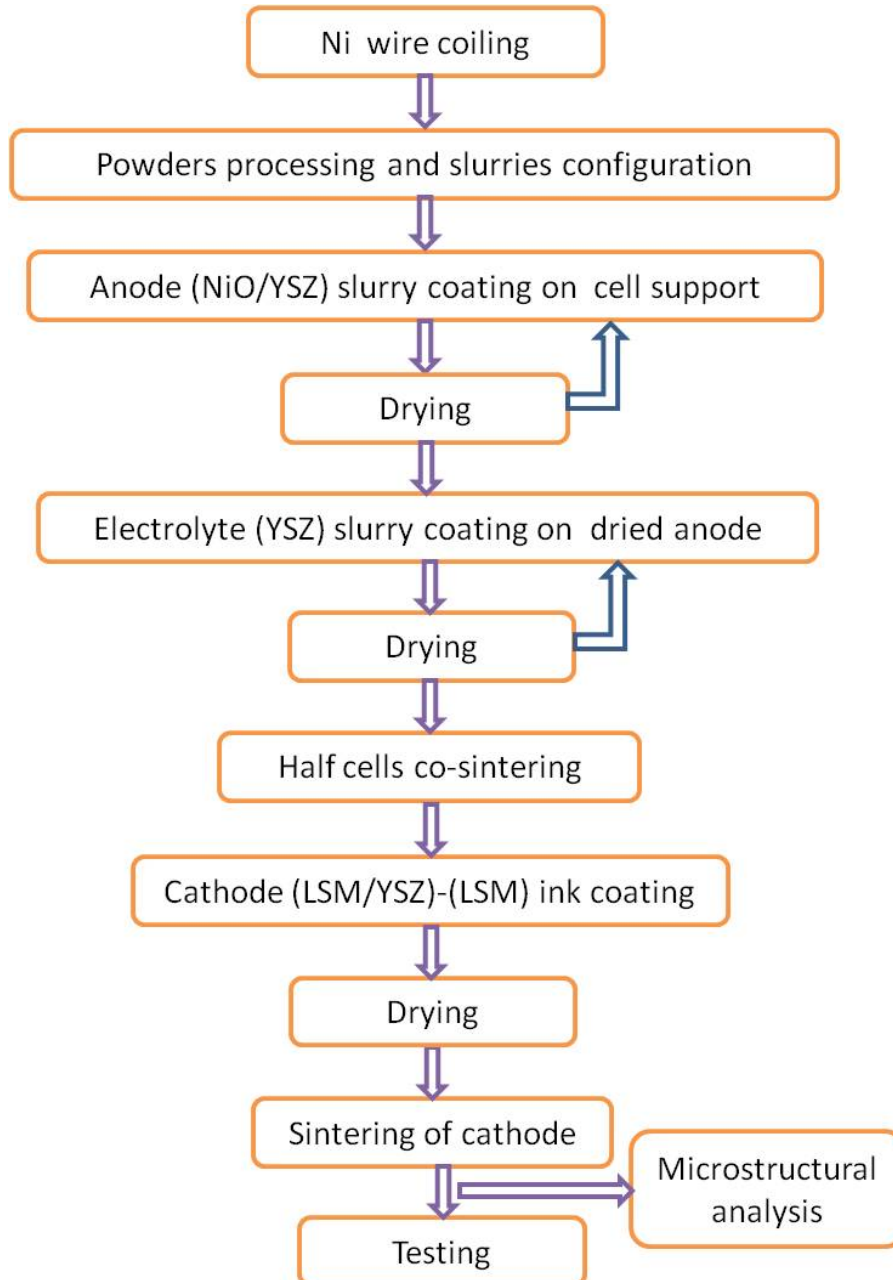


Figure 2.1. Schematic flow chart followed for the experimental procedure.

## **2.1.1 Cell support materials**

### ***2.1.1.1 Current collector***

The material selected for current collection should have properties such as high electric conductivity, a higher melting point to resist the sintering of the NiO/YSZ cermet (about 1400°C) and high mechanical resistance. Among the materials available, nickel and platinum are outstanding as excellent candidates for the purpose. At the same time, the properties of the platinum stand up over those of nickel; however, the cost of platinum is relatively prohibitive. Therefore, Ni wire was chosen as the current collector material for this study.

Nickel wires (99.994%, Alfa Aesar, Germany) with diameters of 0.05 mm and 0.1 mm were considered for coiling.

### ***2.1.1.2 Sacrificial inner core***

In the case of the material for sacrificial inner core, characteristics such as good mechanical resistance, pyrolyzation and null reactivity with the other cell components during processing and sintering are desired. The material frequently used as fugitive material is the graphite in its different configurations (powders, pellets rods, etc.).

In some studies, graphite rods have been used as support for the production of micro-tubular SOFCs [135,142]. However, graphite in its pure

form has not enough mechanical resistance to be used as coiling core. Therefore, carbon composites such as carbon fibre and pencil leads seemed a better option for the purpose. On the other hand, when carbon composites are used some remains after pyrolysis should be expected.

The sacrificial inner core materials used for this research consisted of commercial pencil leads (Faber Castell, Super polymer, 9065 S-2B, Germany) and carbon fibre (Carbon-Composite Technology, Waldstetten, Germany) with 0.5 mm in diameter and a length of 50 mm.

The effect of the remains from carbon composites is considered in the characterization of cells.

### **2.1.2 Production of cell supports**

In order to coil the Ni wire homogeneously along the coil cores (carbon composites), the metal wire was attached to one end of the core and placed on the shaft of an in-house-built electric engine able to fix the number of turn per centimetre in each support. The spring coil was finally pulled along the core to ensure intimate contact between surfaces. A schematic diagram of the coiling system is shown in figure 2.2.

The number of turns per centimetre is determined by the distance between the attachment point and the nickel reel. A balance between a high number of turns along the core to increase the electric contact surface (shorter current paths) without affect the permeability of the electrode was hypothesized.

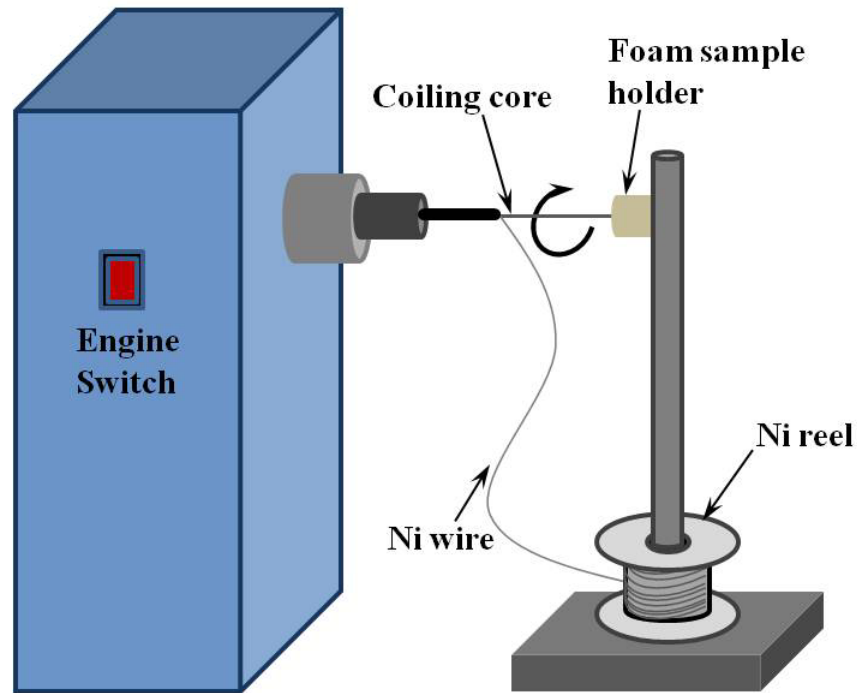


Figure 2.2. Schematic diagram of the coiling system.

### **2.1.3 Pyrolization tests**

The conditions to eliminate the core from the supports cells during successive heating treatments were analysed through pyrolization tests. Temperatures, heating rates, atmospheres and holding times were conjunctly analysed in order to eliminate the core completely without affect the metallic current collector. As the pyrolization of the cores is carry out in air atmosphere the integrity of the metallic spring coil was evaluated after the heat treatment.

## 2 – Experimental Procedure

---

The conditions of the thermal treatments are summarized in table 2.1. The thermal treatment and sintering of cells was done in a tubular furnace (HTRH 100-300/18, GERO Hochtemperaturöfen GmbH, Germany). A protective atmosphere (Ar) was used upon free cooling.

Table 2.1. Pyrolysis tests conditions for cell supports

Temperature (°C)	Heating		Isotherm	
	Rate (°C/min)	Atmosphere	Time (h)	Atmosphere
800	5	Air	0	-
			1	Air
			2	Air
			3	Air
		Ar	0	-
			1	Air
			2	Air
			3	Air
	10	Air	0	-
			1	Air
			2	Air
			3	Air
		Ar	0	-
			1	Air
			2	Air
			3	Air

## 2.2 Powders Processing

The choice of materials for the electrolyte and electrodes used for the production of the micro-tubular SOFCs was based on the commercially available and relatively well-known materials currently used for the production of planar and tubular SOFCs [25,143].

Different techniques and methods were applied for the characterization of powders. According to the geometry of the cell supports the technique most appropriate for the coating deposition is dip coating. Therefore, the powders processing was focused on the establishment of the most convenient parameters for this technique.

### 2.2.1 Materials

NiO (J.T. Baker Inc., USA) and two different 8 mol% Y<sub>2</sub>O<sub>3</sub>-ZrO<sub>2</sub> (TZ-8Y and TZ-8YS, Tosoh, Japan) powders were used in this study. The difference of the YSZ powders is their specific surface area (SSA), which is in the order of 13 m<sup>2</sup>/g for the 8Y and 6 m<sup>2</sup>/g for the 8YS. Cermet based NiO-YSZ (58/42 wt% ratio) and YSZ were used as anode and electrolyte, respectively.

In order to increase the porosity of the cermet graphite powder (Flake, 7-10 μm, Alfa Aesar, Germany) was added in the range of 5-10 wt%. The

effect of the pore former on the microstructure of cermet was investigated using a Scanning Electron Microscope (JEOL, JSM 5500, Japan).

Finally,  $\text{La}_{0.8}\text{Sr}_{0.2}\text{MnO}_{3-\delta}$  (LSM, Fuel Cell Materials, USA) was used as cathode material. A bilayer-structured material consisted of a layer of LSM-YSZ (50/50 wt% ratio) as functional ionic layer and a second layer made of pure LSM as electronic layer was applied.

### **2.2.2 Powders characterization and suspensions optimization**

Characteristics such as the SSA and dispersant concentration were measured for each powder by means of nitrogen adsorption (BET) method (ASAP 2010, Micromeritics, USA) and sedimentation tests respectively. The powders were dispersed with a commercial dispersant of ammonium polyacrylate (Darvan 821A, R.T. Vanderbilt Company Inc., USA). The green strength of the layers deposited was increased with the addition of high molecular weight acrylic based polymers in aqueous emulsion (Duramax B-1000 and B-1014, Rohm and Haas Co., France) during the slurries preparation. The amount of binders was varied according to the results obtained in the dip coating.

Slurries with different YSZ powders were prepared for anode and electrolyte with the objective to find the best combination for the cells production.

### **2.2.2.1 Sedimentation tests**

The sedimentation tests are based on the comparison of sediment heights measured in function of time of slurries with different dispersant concentration poured into a test tube. After a period of time (usually 30 days) the most compact sediment would indicate the dispersant concentration required to stabilize that suspension.

The concentration of dispersant was calculated for the NiO, YSZ (8Y and 8YS) and graphite powders. The order in the addition of elements is determinant for the slurries fabrication. The way followed in this study was first put the grinding media (zirconia spheres) into a jar and subsequently the powder, water and the dispersant at the specific concentration. The concentrations analysed were 0, 0.005, 0.01, 0.03, 0.05 and 0.1 mL of dispersant/g of powder. The powder (4 wt%) with water (distilled) and dispersant is milled in a high energy vibratory mill (Turbula T2F, Bachofen, Switzerland) for 2 h. Then, the slurry is recuperated and poured into a test tube. The measurement of the height was periodically checked. Three zones are detected in sedimentation test:

1. Clear zone: Absence of particles due to a rapid sedimentation.
2. Diffuse zone: Smaller and well-dispersed particles are suspended for longer periods of time.
3. Compact zone or sediment: Bigger particles and agglomerates sediment faster and after a long period of time the dispersed particles

## 2 – Experimental Procedure

---

will sediment too. The sediment of a stable suspension is more compact than that with agglomerates due to better arrangement between particles (without the free spaces present in agglomerates).

Figure 2.3 shows the difference between the three zones present during sedimentation tests.

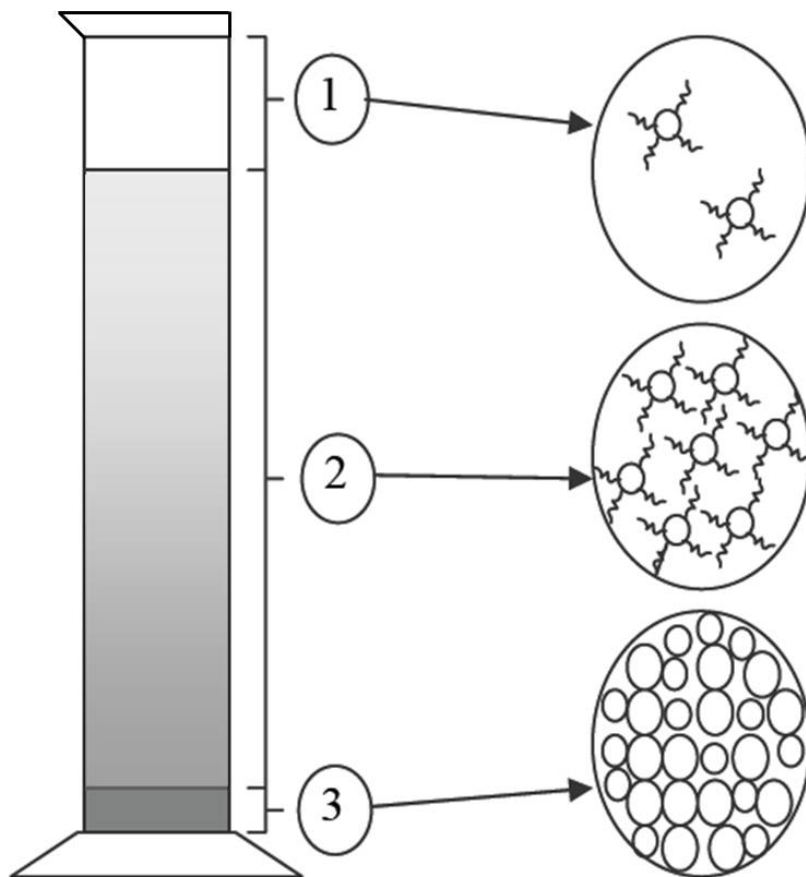


Figure 2.3. Schematic diagram of the zones detected in sedimentation tests [144].

### ***2.2.2.2 Slurries preparation***

Stable slurries were prepared for anode and electrolyte at different solid loading contents (from 60 to 90 wt% and 60 to 80 wt%, respectively). Combinations of anode and electrolyte powders were considered before analyze the effect of graphite on the anode microstructure.

The procedure followed for the fabrication of suspensions was similar to that reported for the sedimentation tests. In this case, the amount of dispersant was added in the respective concentration needed to deflocculate each powder. The suspension recuperated after milling was maintained in agitation with a magnetic stirrer during 1 h. Later, the first binder (B1014) was gradually added and maintained under a gently stirring for 30 min. Similarly, the second binder (B1000) was added to the slurry and maintained in agitation for 1 h before use it. Different amounts of binder were analysed in order to fabricate crack-free layers at green.

### ***2.2.2.3 Cathode ink preparation***

A suspension of cathode particles was done using  $\alpha$ -Terpineol as ink vehicle (V-006, Fuel Cell Materials, USA). The powder and the terpineol are put into a jar and mixed for 2 h. Then the suspension is recovered and poured into a container for dip. Solid loading contents between 20 and 50 wt% for the functional and conductive layers were analysed.

## 2.3 Production of Micro-Tubular SOFC

The production of micro-tubular cells includes the analysis and development of the most proper condition for the coating, characterization and sintering of anode, electrolyte and cathode materials. As the technique of dip coating was used for the production of electrodes and electrolyte many factors have been analysed such as solid loading in suspensions and the amount of binder needed to increase the green strength of the anode and electrolyte layers. In addition, by using an electric engine was possible change the dip coating parameters (dip/withdrawal speed and dwelling).

The flow chart to produce the micro-tubular cell by dip coating is schematic shown in figure 2.4.

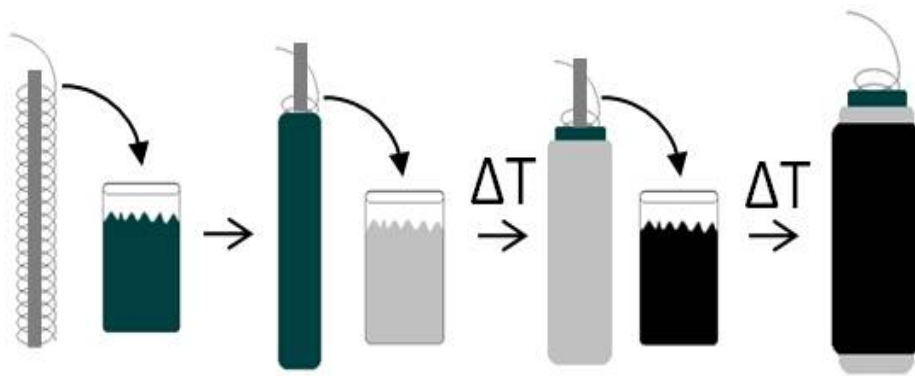


Figure 2.4. Schematic flow chart to produce cells by dip coating.

### **2.3.1 Dip coating process for half-cells**

Dip coating was an effective easy-technique to cover the support cells with the electrodes and electrolyte materials. In addition, a good control of thickness is achieved by manipulating the parameters of the process. Trials were done with different solid loads, binder content, dip and withdrawal speed, dwelling times and drying methods to produce half-cells with the characteristics desired. The conditions analysed for the dip coating process in half-cells are summarized in table 2.2.

Table 2.2. Conditions analysed for dip coating process in half-cells

		Anode	Electrolyte
Suspension	Solid loading (wt%)	60-90	60-80
	Binder content (wt%)	B1014	0.01-0.2
		B1000	0.01-0.2
Dip coating	Dip/withdrawal (mm/min)	10-80	10-80
	Dwelling (min)	0-2	0-2
Drying	Time (h)	0.5-24	0.5-24
	Temperature	RT-120°C	RT-120°C

## 2 – Experimental Procedure

---

The solid load contents of slurries were varied depending of the characteristics of layers deposited on the supports. It was distinguished that high solid loads will produce a thick layer with low volume contraction and faster drying time. On the other hand, at lower solid loads a thin layer with higher volume contraction and longer drying times will be obtained.

The amount of binder in slurries is another significant parameter for dip coating. Especially for long surfaces such as rods due to high axial stresses during drying. The main purpose of the additives in coating techniques is the enhancement of the mechanical properties before sintering. In the case of dip coating the high cohesion of particles produced by the additives improves the adhesion to the substrate which benefits the homogeneity of thickness along the length. However, a less control of thickness can result from the much more material deposited in each dip. Therefore, the importance to reach the thickness desired with a minimum number of dips. In this study, the amount of binders used in the slurries was defined empirically.

The inherent parameters of dip coating such as dip and withdrawal speed and dwelling time were studied. Generally, the dip speed has not an evident effect on the coating thickness whereas the withdrawal speed has a key role in the control of thickness. A low withdrawal speed allows a thinner coating with a more homogeneous thickness along the length. Finally, the effect of dwelling presents an increase in the thickness and is quite evident from the second dip.

The last step in the dip coating process corresponds to the drying method. This is the most critical parameter in the dip coating process since defects and cracks are generated during it. The most common defects in the coatings are cracks in the radial direction due to high axial stresses generated by differences in thickness along the length. The effect of temperature and time on drying was analysed in the range of room temperature to 120°C and from 30 min to 24 h, respectively.

The number of dips was defined by thickness obtained by using specific conditions combinations.

### **2.3.2 Thermal analysis of half-cells**

Due to the differences in SSA values of the two YSZ powders was possible formulate different combinations for anode and electrolyte. The thermal behaviour of each one of these combinations was investigated by means of thermo-mechanical analysis (Dilatometer Setaram, Setsys Evolution, France). Cylindrical-shaped samples of around 5 mm in diameter and 4 mm in height of each configuration were tested at 1400°C with heating rate of 5 °C/min in air atmosphere. Details regarding to the rate and maximum shrinkage were useful for the selection of the proper combination between the anode and electrolyte. The combinations of powders for anode and electrolyte are:

- Anode
  1. NiO/YSZS
  2. NiO/YSZ
  3. NiO/((YSZS/YSZ) (70/30 wt% ratio))
  
- Electrolyte
  1. YSZS
  2. YSZ
  3. YSZS/YSZ (70/30 wt% ratio)

The shrinkage observed in each combination will be with comparative purposes only due to the effect of graphite pyrolyzation, wire oxidation and argon atmosphere on the real sintering of cells. However, when cracks caused by thermal mismatches were present after sintering on half-cells the thermal behaviour of these combinations addressed the shrinkage tailoring.

### **2.3.3 Effect of pore former in anode**

After the choice of the most feasible combination of anode and electrolyte for the production of micro-tubular cells was preceded to the analysis of the graphite on the porosity and microstructure of anode.

As a support, anode is much thicker than other components. Therefore, the anode should provide enough open pores for transporting fuel and reactive products so that electrochemical reaction can be lasted. Otherwise,

great concentration polarization loss will make cell power decrease rapidly. There are two kinds of pores: open pores and close pores. The close pores are ineffective, so should be reduced. Higher porosity may reduce close pores; however, the strength and electrical conductivity is also decreased. According to the theory of seepage flow, more than 33% porosity is needed to form most open pores, so anode porosity should be controlled between 30 and 40% [145].

In order to reach the porosity needed in the anode, graphite was added as pore former and the content was in the range of 5-10 wt%.

The porosity at different graphite contents were measured by Archimede's method. A base case with no addition of graphite was also checked.

Due to the hydrophobic and non wetting nature of graphite, the addition of binder was readjusted to avoid the separation of graphite from the NiO/YSZ slurry.

### **2.3.4 Co-sintering of half-cells**

The co-sintering of half cells was developed in three consecutive stages:

- i) The elimination of additives below 600°C in air.
- ii) The pyrolyzation of the pore former and inner core around 700-800°C in air for 1 h.

## 2 – Experimental Procedure

---

- iii) The co-sintering of anode and electrolyte layers up to 1380°C for 2 h in argon.

The thermal cycle followed for the co-sintering of half cells is shown in figure 2.5. A constant heating rate of 5 °C/min was used for all the treatment. After the elimination of organics and fugitive materials an argon atmosphere is used to protect the nickel wire of excessive oxidation during sintering (including cooling).

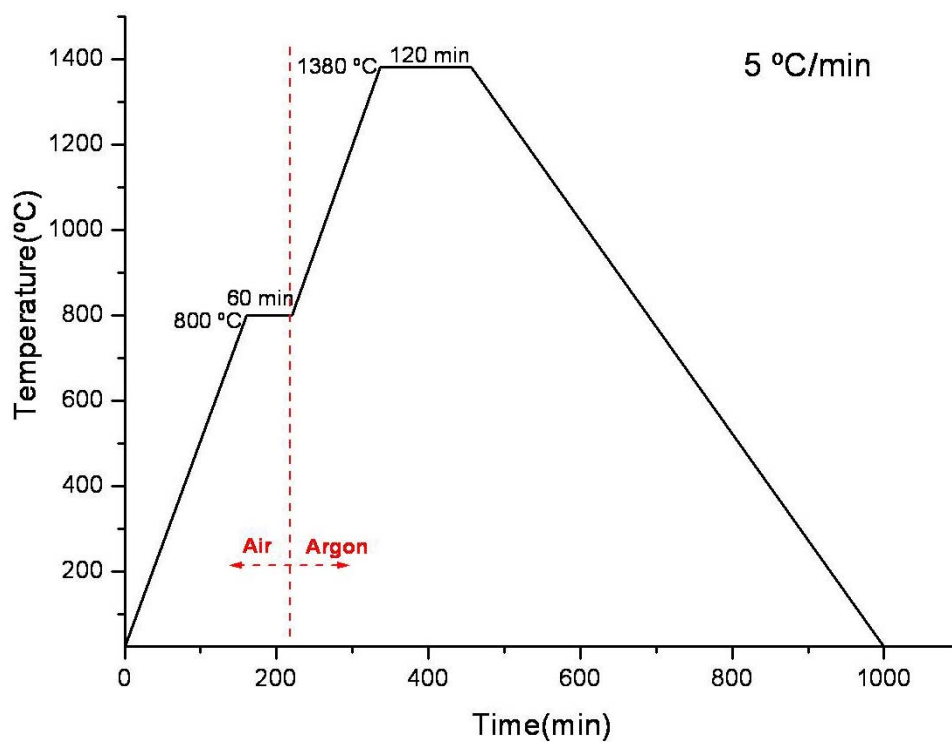


Figure 2.5. Thermal cycle for the sintering of half-cells.

### **2.3.5 Deposition and sintering of cathode**

The last step in the production of micro-tubular cells corresponds to the deposition of cathode. A bilayer-structured material was developed for cathode. The first layer is used as functional layer and the second one has the objective to increase the electronic conductivity. Both layers were deposited from cathode inks by dip coating. The use of ink as dispersant media has advantages such as high stability over time and good adhesion to the surfaces. Additionally, the microstructure generated is enough porous for the transporting of gas species to the reactive sites. The deposition of cathode is relatively easy, so less parameters were varied for its application.

#### ***2.3.5.1 Cathode deposition and characterization***

The sintered half-cells were dipped into the cathode inks with solid load contents in the range of 20 to 50 wt%.

The thickness of the coatings is majorly controlled by the solid loading content. At low solid contents the coating is thinner and more homogeneous than at high loading contents. On the other hand, the dip/withdrawal speed and dwelling time parameters have relatively low impact of the coating thickness.

## 2 – Experimental Procedure

---

The temperature of drying was analysed from room temperature to 120°C. It was observed that a fast drying cause severe cracking along the length which can be solved with low drying rates at room temperature.

The porosity of cathode was measured at the respective solid loads. Generally, the porosity is governed by the ink vehicle evaporation more than the solid loading content. Consequently, similar porosity was measured for the different solid loads studied.

In table 2.3 are summarized the conditions analysed for the deposition of cathode.

Table 2.3. Conditions analysed for the cathode deposition

		Functional and conductive layer
Suspension	Solid loading (wt%)	20-50
Dip coating	Dip/withdrawal (mm/min)	10-80
	Dwelling (min)	0-2
Drying	Time (h)	0.5-24
	Temperature	RT-120°C

### 2.3.5.2 Sintering of cathode

The thermal cycle for the sintering of cathode is quite similar to that for half-cells due to the protective atmosphere needed for the nickel wire. In this case (figure 2.6), a successive sintering process consisted of the elimination of organics at 800°C for 1 h in air followed by the sintering at 1150°C for 2 h in argon with a heating rate of 5 °C/min was done.

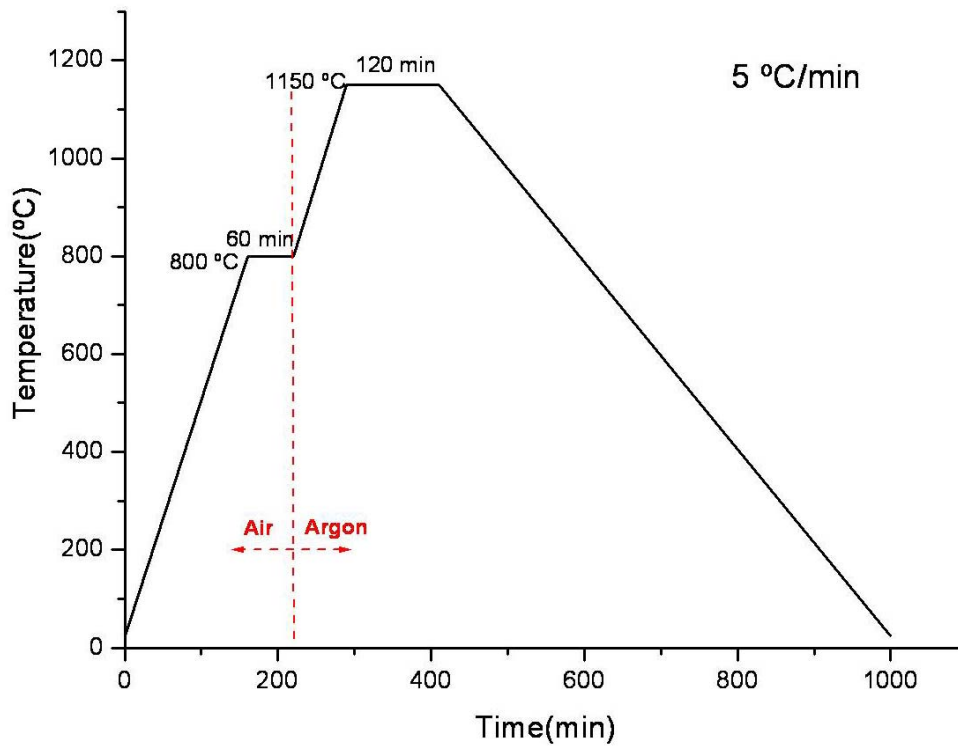


Figure 2.6. Thermal cycle for the sintering of cathode multi-layered.

## **2.4 Performance analysis of Micro-Tubular SOFC**

The performance of the current collector-supported micro-tubular cells was measured by means of electrochemical tests (I-V curves). The power density obtained by using the current collector-supported cells is compared with the performance of a micro-tubular SOFC produced and tested under similar condition but using one of the most common methods of current collection (straight wire along the core of cell).

### **2.4.1 Testing apparatus**

#### ***2.4.1.1 Current collector-supported cells***

The electrochemical performance was measured with a built-in-house test station. Figure 2.7 shows the schematic diagram of the test setup apparatus for the current collector-supported micro-tubular cells.

The two terminals of nickel wire used as coil current collector were directly attached to platinum wires (99.997%, Alfa Aesar, Germany) for the current collection on the anode side. While the current collection from the cathode side was conducted with a platinum gauze (99.9%, 0.1 mm diameter wire, 25 mm x 25 mm, Alfa Aesar, Germany) wrapped on the

## 2 – Experimental Procedure

whole external cathode area. Silver ink (99.997%, Alfa Aesar, Germany) was used to increase the electric contact between the gauze and the cathode surface and in the attachment points between the nickel and platinum wires.

The micro-tubular cell was then fixed and sealed with two alumina tubes via a ceramic sealant (Ultratemp 516, Aremco, Valley Cottage, NY) and placed into a tubular furnace. Finally, the current collecting wires were brought outside the furnace to achieve the electrical connections.

The I-V characteristics of the cells were measured using a potentiostat (Autolab PGSTAT302N, Eco Chemie, Netherlands) and a computer for data acquisition.

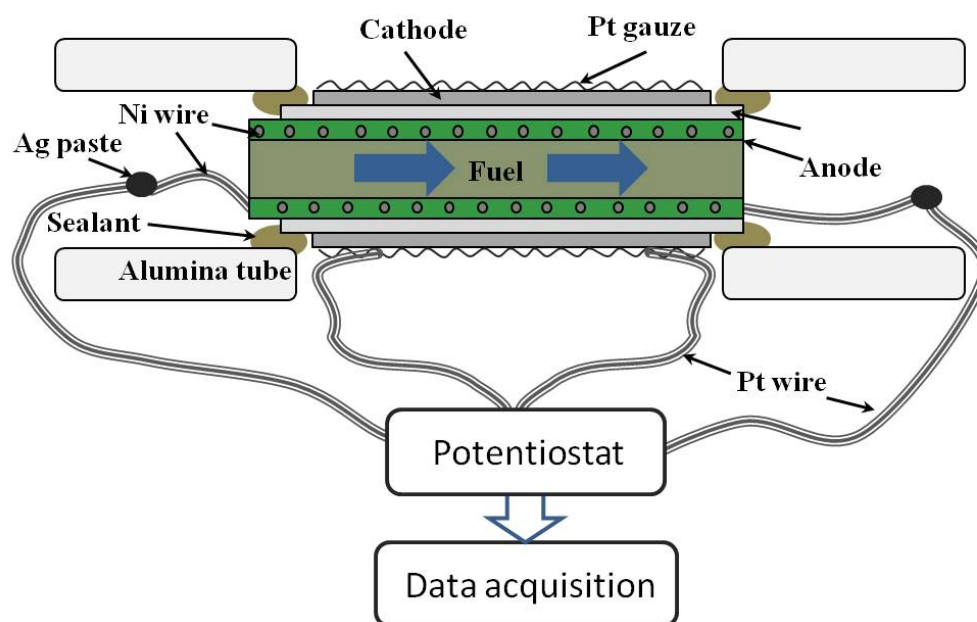


Figure 2.7. Schematic diagram of the setup apparatus for current collector-supported cells.

### 2.4.1.2 Straight wire within the core of the cells

The experimental apparatus and assembly process for the straight wire current collection method (figure 2.8) is similar to that described for current collector-supported cells.

The difference consists in the anode current collection method. In this case, a straight nickel wire (99.994%, Alfa Aesar, Germany) of 0.1 mm in diameter was inserted within the core of the micro-tubular cells for current collection. The nickel wire ends were then attached to the platinum wires.

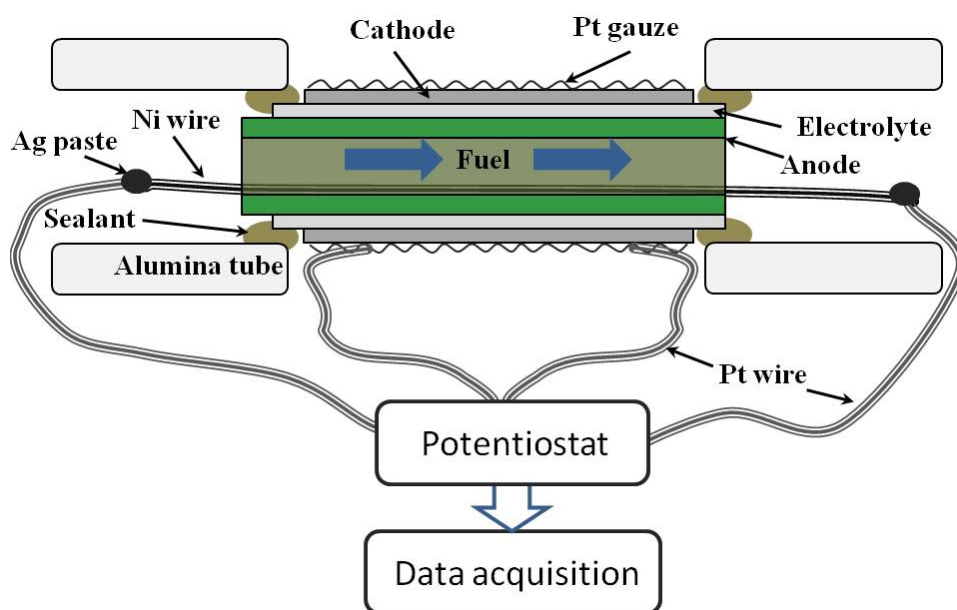


Figure 2.8. Schematic diagram of the setup apparatus for a straight wire current collection method.

## **2.4.2 Conditions of testing**

The conditions of the electrochemical testing reported in this section are identically for the two current collection methods. Moreover, the power density obtained in each cell is affected by its active cathode area. Therefore, the current collection method is in practical terms the only variable upon testing.

### ***2.4.2.1 Anode reduction***

The reduction of anode was achieved at high temperature. Therefore, the cells were heated at 10 °C/min in the furnace to their respective operative temperatures, which are 700, 750 and 800°C while nitrogen passed through the inner channel at 25 mL/min. After reach the target temperatures, nitrogen supply was gradually turned off as hydrogen was introduced. Anode reduction was achieved by passing hydrogen humidified by bubbling water at room temperature (97% H<sub>2</sub> and 3% H<sub>2</sub>O) with a flow rate of 25 mL/min through the cell for an exposure time of 25 min. The cathode of the tube was exposed to the ambient air without flowing gas.

### **2.4.2.2 *Electrochemical testing***

The current-voltage (I-V) curves were tested by linear sweep voltammetry at a scanning rate of 5 mV/s.

Nova 1.6 (Metrohm Autolab B.V) software was used to control the data acquisition process.

# 3. Results and Discussion

---

The results of the activities described in the experimental procedure are reported and discussed in this section. The results will show that the current collector-supported cells were successfully produced and tested with performances in good agreement with the state of art of the micro-tubular cells. In addition, the enhancement of the performance by using the current collection method proposed in this study will be justified in terms of shorter current paths in comparison with a common current collection method.

## 3.1 Cell Supports

The produced cell supports are shown in figures 3.1 to 3.3. It can be seen that although the coiling conditions were fixed for all cases, the number of turns per centimetre is also dependent of the type of core used. The useful length for the coiling was about 4 cm for both cores (figure 3.3). The characteristics of the produced support cells are summarized in table 3.1.

### 3 – Results and Discussion

Table 3.1. Characteristics of cell supports

Core type	Core diameter (mm)	Wire diameter (mm)	Turns per centimetre
Pencil lead	0.5	0.1	11-12
		0.05	
Carbon fibre	0.5	0.1	12-13
		0.05	

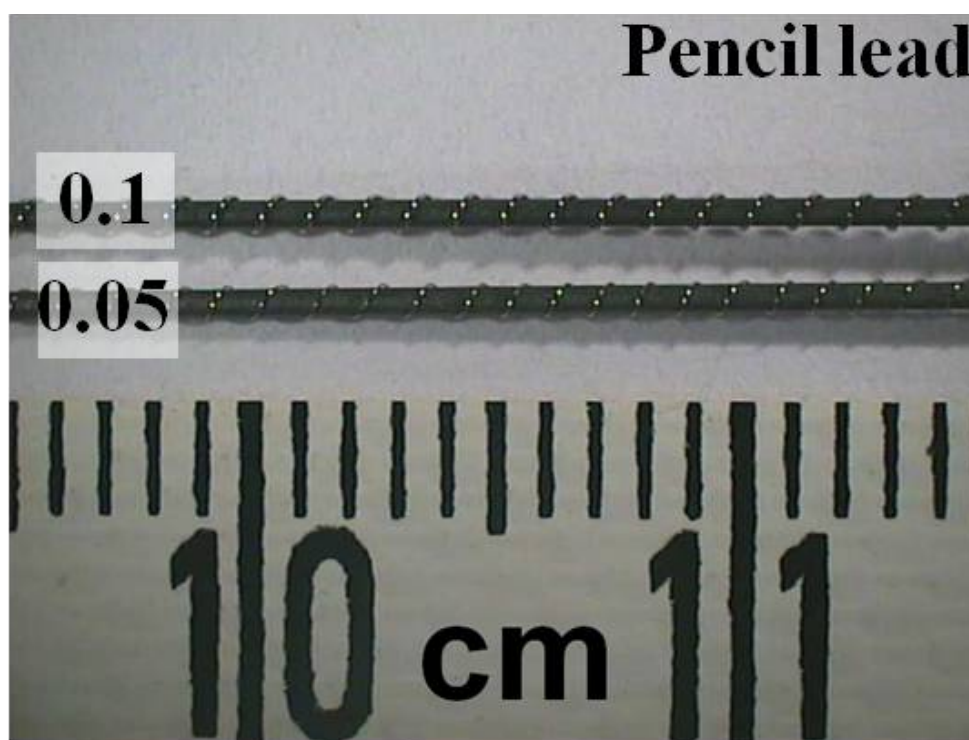


Figure 3.1. Photograph of current collector supports with pencil leads and different wire diameter.

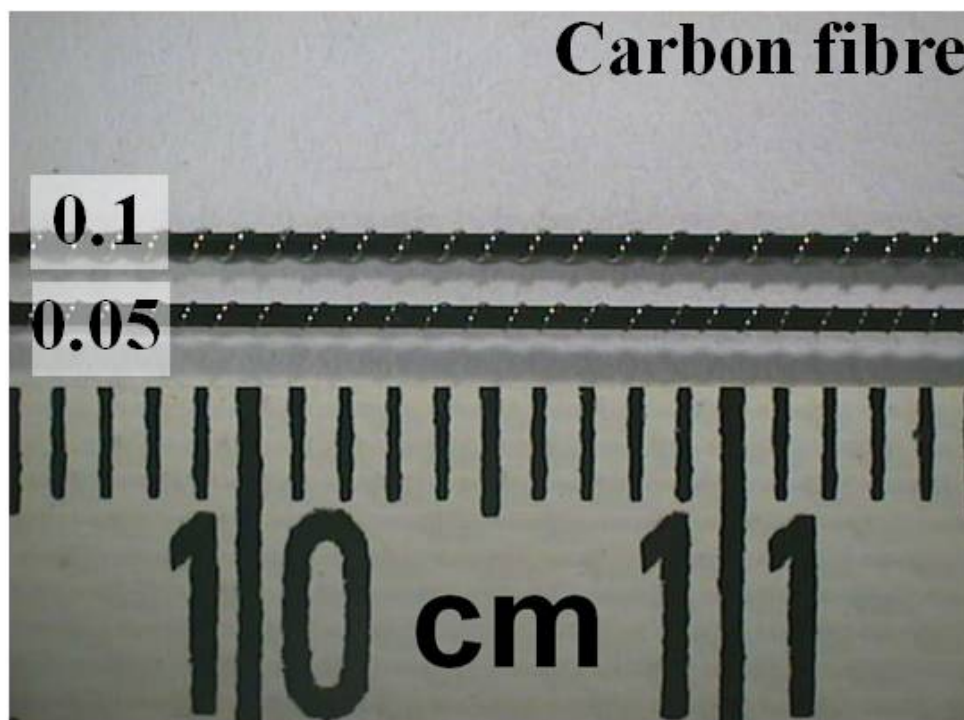


Figure 3.2. Photograph of current collector supports with carbon fibre and different wire diameter.

The thermal treatments performed on the support cells showed that the more convenient conditions for the elimination of the inner core were heating in air up to 800°C with heating rate of 5 °C/min, followed by an isotherm of 1 h in air. However, the two diameters were barely oxidized. While the thicker wire maintained enough mechanical resistance after the treatment, the thinner wire was not useful for subsequent processing steps. Figure 3.4 shows the 0.1 and 0.05 mm wires after core elimination.

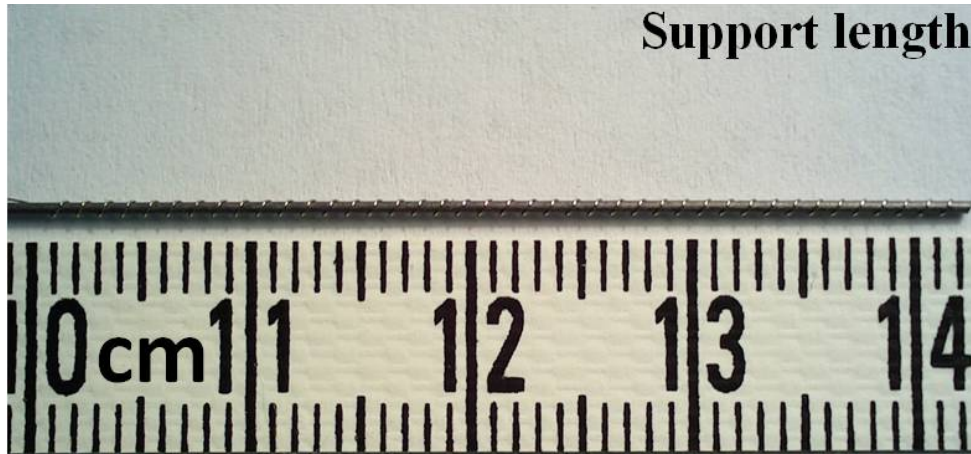


Figure 3.3. Photograph of current collector supports length.

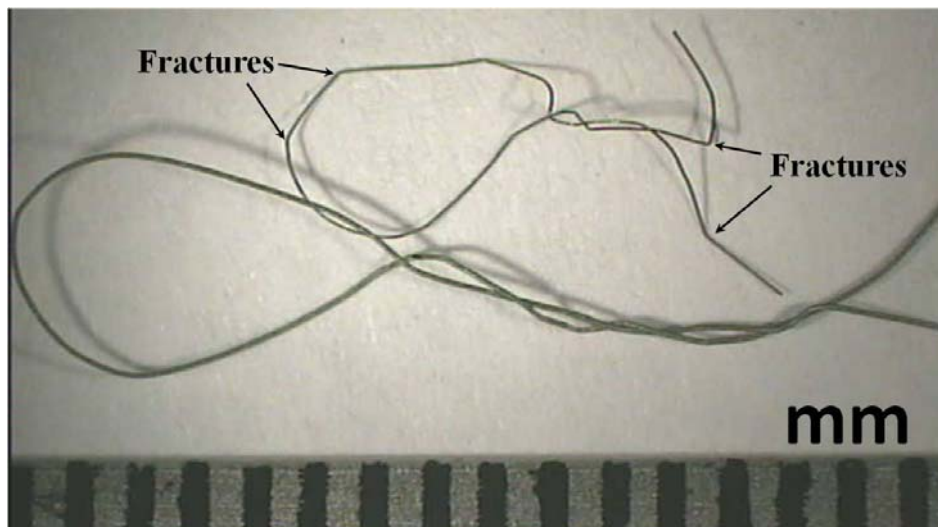


Figure 3.4. Photograph of 0.1 and 0.05 mm nickel wires after core elimination process.

## 3.2 Powders Processing

### 3.2.1 SSA and dispersant concentration

The results of specific surface area and dispersant concentration measurements are summarized in table 3.2. Although the dispersant acts only on the surface of the particles, a direct proportional ratio is not evident. This is due to the effect of characteristics such as porosity, geometry and size of particles in powder on the sedimentation.

Table 3.2. SSA and dispersant concentration for different powders

Powder	SSA (m <sup>2</sup> /g)	Dispersant concentration (mL Darvan/g of powder)
NiO	3.5	0.005
YSZS	6	0.005
YSZ	13	0.01
Graphite	12	0.01
LSM	5.6	-

### 3.2.2 Thermal analysis

Using the values reported in table 3.2, stable slurries of anode and electrolyte with a solid loading content of 80 wt% were produced to analyse

### 3 – Results and Discussion

the shrinkage behaviour of the different combinations. The addition of binder was not necessary for the production of samples used in dilatometric tests.

The main purpose of the dilatometric curves (figure 3.5 and 3.6) was to establish the best combination of anode and electrolyte layers to reduce thermal stresses upon sintering.

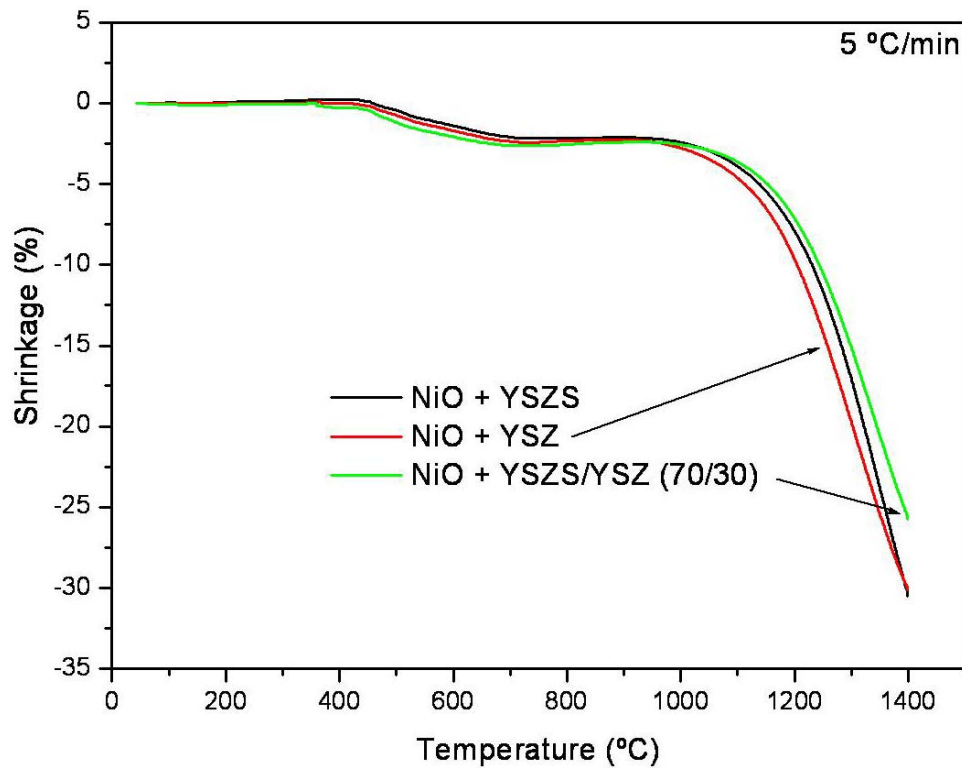


Figure 3.5. Dilatometric curves for anode cermet combinations.

### 3 – Results and Discussion

The dilatometric anode curves (figure 3.5) show a calcination step of 2.5% from 440°C to 700°C. Then the cermet NiO/YSZ presents a slightly increase in the sintering rate in comparison with the others two. On the other hand, the lowest sintering shrinkage (23.8%) was achieved by using the cermet NiO/(YSZ/YSZS) with the slowest sintering rate. The cermets NiO/YSZ and NiO/YSZS present the same shrinkage value (28.4%) at 1380°C with a slightly slower sintering rate of the second one. The main shrinkage step started at 1000°C for the three samples.

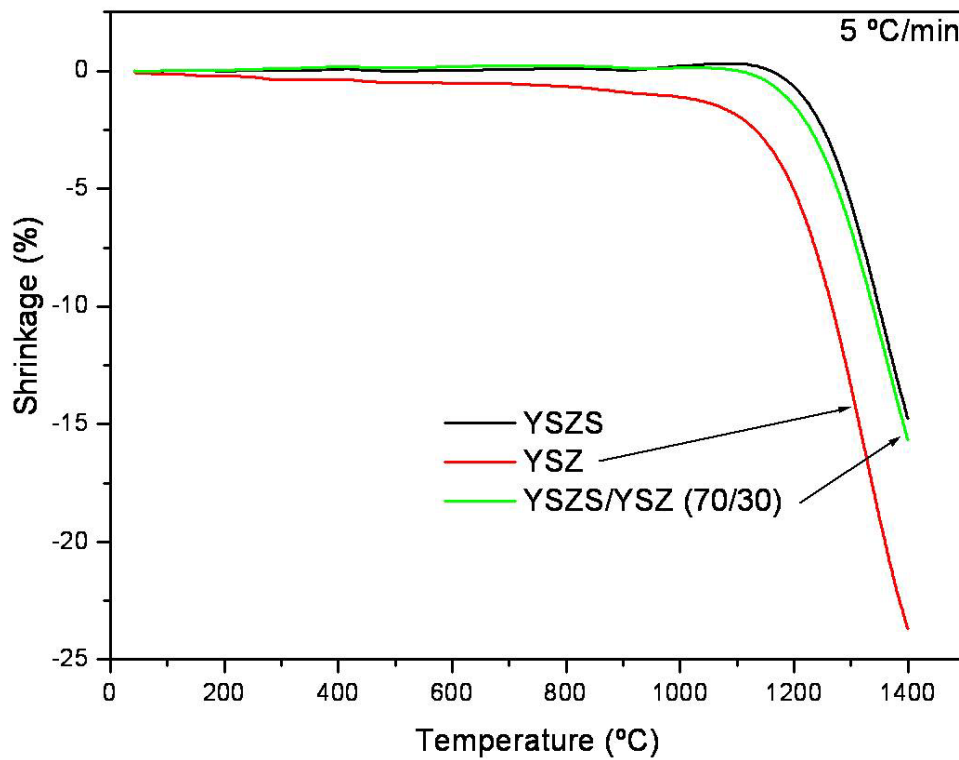


Figure 3.6. Dilatometric curves for electrolyte combinations.

In the dilatometric electrolyte curves (figure 3.6) only the YSZ sample started volume changes at low temperatures (around 300°C). Additionally, the highest shrinkage (22%) was also achieved with the fastest sintering rate by this sample. The behaviour of the other samples was quite similar between them. The main and only shrinkage step for these samples was started at 1100°C and the shrinkage at 1380°C was of 13%.

From the dilatometric curves shown in figures 3.5 and 3.6 a distinctive difference in shrinkage is observed in the respective anode cermets (around 5%) and electrolytes (9%) combinations. This suggests that the overall shrinkage of half-cells can be successfully tailored by changing the cermet/electrolyte combination.

Three different approaches were proposed for the selection of the most appropriate combination. In order to consider the effect of the nickel wire on the sintering of half-cells springs without cores or any specific conditions (early trials in the coiling of nickel wire) were used to deposit the anode and electrolyte layer for the respective combination.

1. Similar shrinkages between anode and electrolyte.

Only the combination of NiO/(YSZS/YSZ)-YSZ presents a relatively match between anode (23.8%) and electrolyte (22%). The samples sintered under this criterion were cracked and bended due to high thermal stresses. Figure 3.7 shows a sample after sintering.

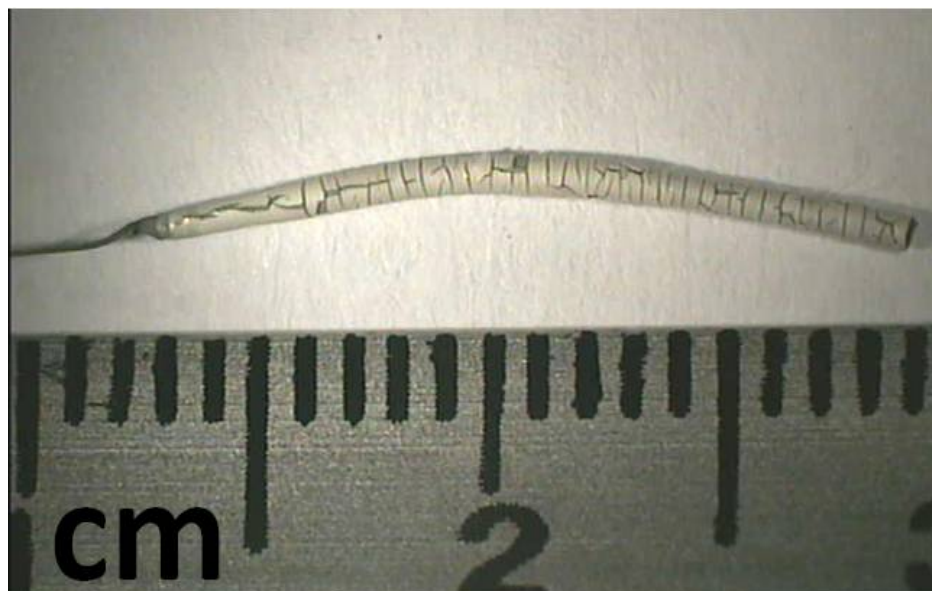


Figure 3.7. Photograph of NiO/(YSZS/YSZ)-YSZ half-cell sintered at 1380°C.

**2. Fix the lowest anode shrinkage and change the electrolytes.**

In this case, the cermet NiO/(YSZS/YSZ) was fixed to deposit the other two electrolytes with lower shrinkage. The results are basically the same than the previous case. Axial and radial cracks are present along the half-cell. Therefore, the cermet with the lowest shrinkage don not seems effective in the production of half-cells. Figures 3.8 and 3.9 shows the samples sintered with this principle.

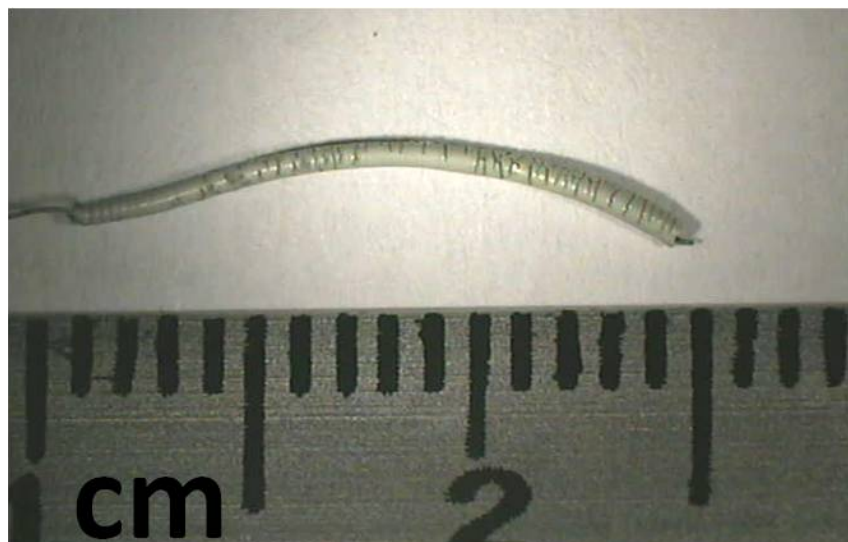


Figure 3.8. Photograph of NiO/(YSZS/YSZ)-(YSZS/YSZ) half-cell sintered at 1380°C.

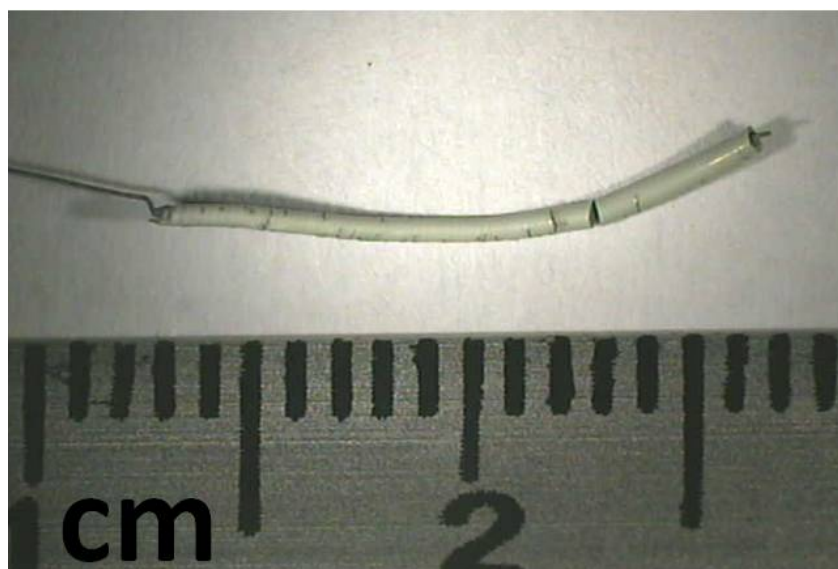


Figure 3.9. Photograph of NiO/(YSZS/YSZ)-YSZS half-cell sintered at 1380°C.

3. Fix the highest anode shrinkage and change the electrolytes.

In this case, the cermet made of NiO/YSZS was fixed and a better matching with the electrolytes was achieved. However, the combination with the YSZ continues present a slightly bending and cracking (Figure 3.10). On the other hand, a good thermal matching without bending nor cracks was obtained with the YSZS (Figure 3.11) and YSZS/YSZ (Figure 3.12), though for simplicity the YSZS was choice for the production of half-cells. The characteristics of this combination are the highest anode shrinkage (28.4%) with the lowest electrolyte shrinkage (13%).

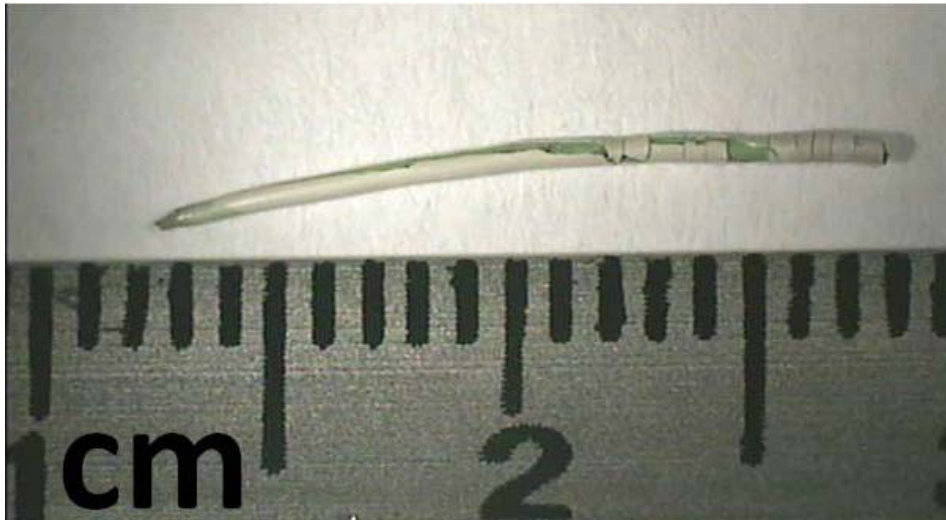


Figure 3.10. Photograph of NiO/YSZS-YSZS half-cell sintered at 1380°C.

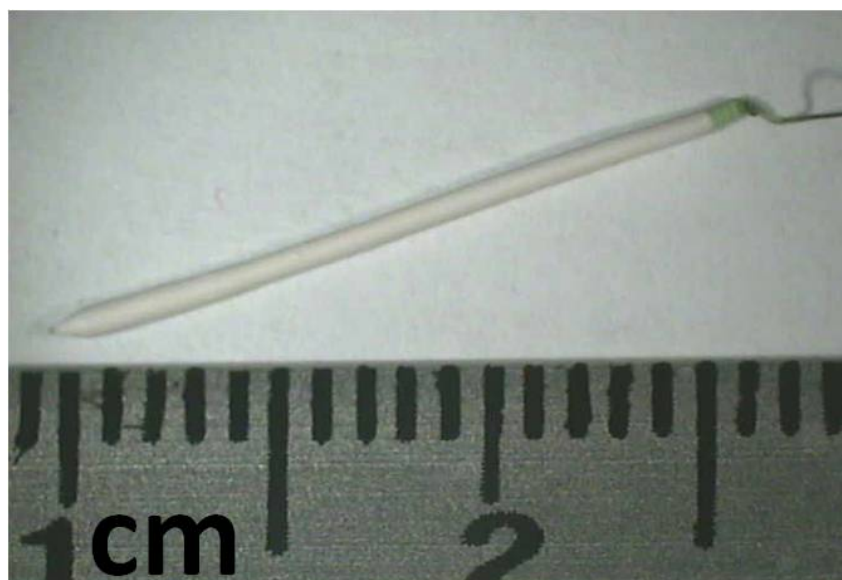


Figure 3.11. Photograph of NiO/YSZS-(YSZS/YSZ) half-cell sintered at 1380°C.

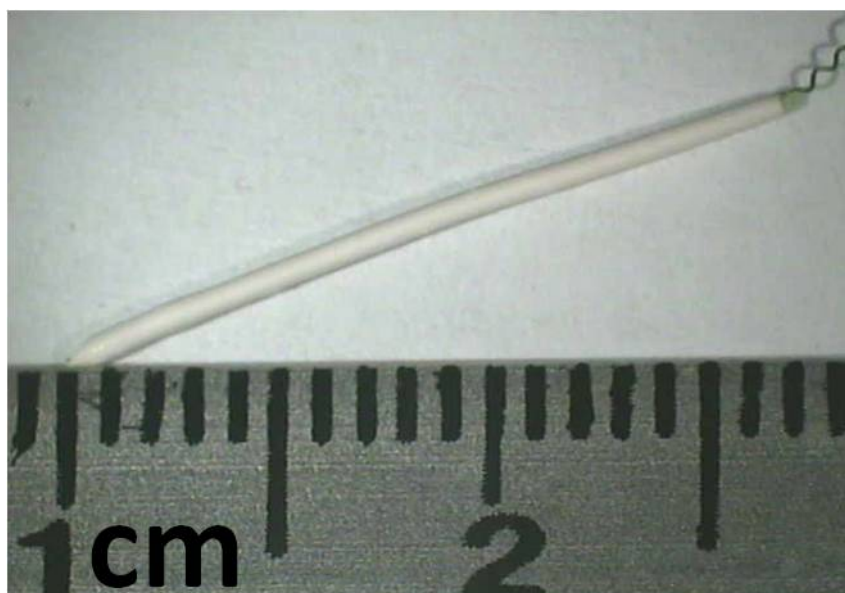


Figure 3.12. Photograph of NiO/YSZS-YSZS half-cell sintered at 1380°C.

### **3.2.3 Effect of pore former within the anode**

The pore former analysis was developed by using stable anode slurries with a solid loading content of 80 wt% (around 66.7 wt% after the addition of binders). The amount of each binder was fixed arbitrarily at 10 wt% of the slurry weight recovered after mixing to avoid the separation of graphite from the slurry. The slurries composition for different graphite contents is reported in table 3.3.

Table 3.3. Anode slurries composition at different pore former contents

Component (wt%)	Graphite content in the anode slurries (wt%)			
	0	5	8	10
NiO	46.4	43.5	41.76	40.6
YSZ (8YS)	33.6	31.5	30.24	29.4
Water	19.6	19.575	19.56	19.55
Dispersant	0.4	0.425	0.44	0.45

The slurries were deposited on a glass support and dried at 80°C for 5 h. The samples were finally sintered at 1380°C for 2 h. Successively, the porosity and microstructure of the samples were evaluated. The porosity measured by the Archimede`s method is shown in figure 3.13.

The addition of graphite into the anode slurries increases significantly the porosity of the anode cermet. The porosities obtained were 20, 33.5, 36.8 and 39.6% for 0, 5, 8 and 10 wt% of graphite, respectively. Thus, using

### 3 – Results and Discussion

---

5 wt% of graphite assures the porosity needed for the fuel flux through the anode thickness maintaining its mechanical and electrical properties.

The microstructure of the samples sintered at 1380°C is show in figures 3.14-3.17. A more porous microstructure is obtained as the graphite content is increased.

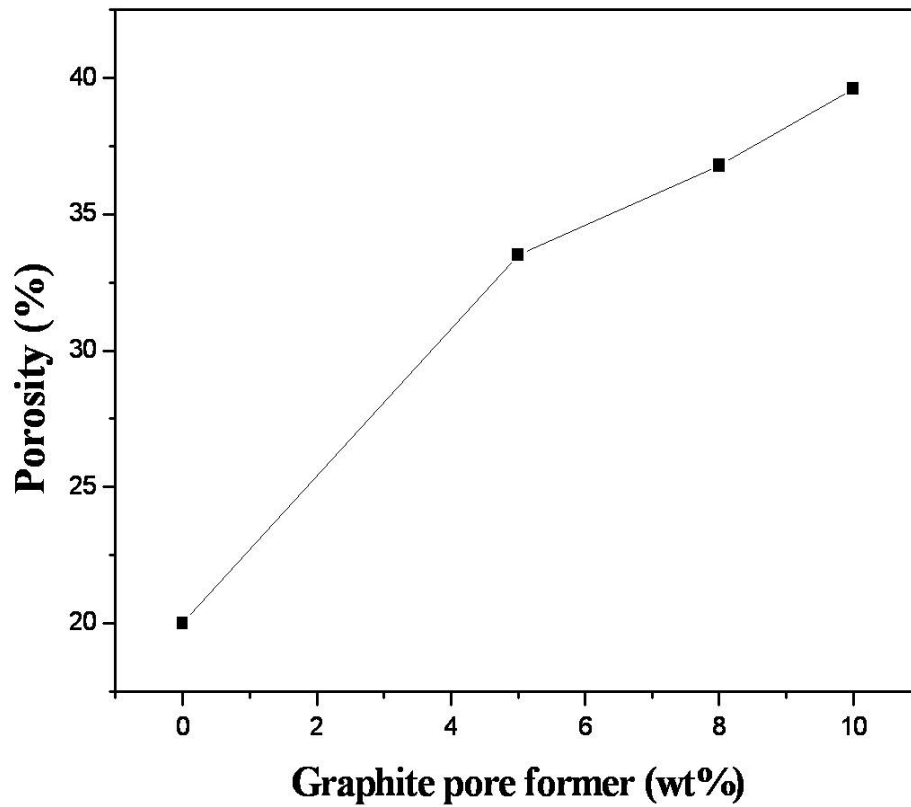


Figure 3.13. Effect of graphite content on the porosity of the anode cermet sintered at 1380°C.

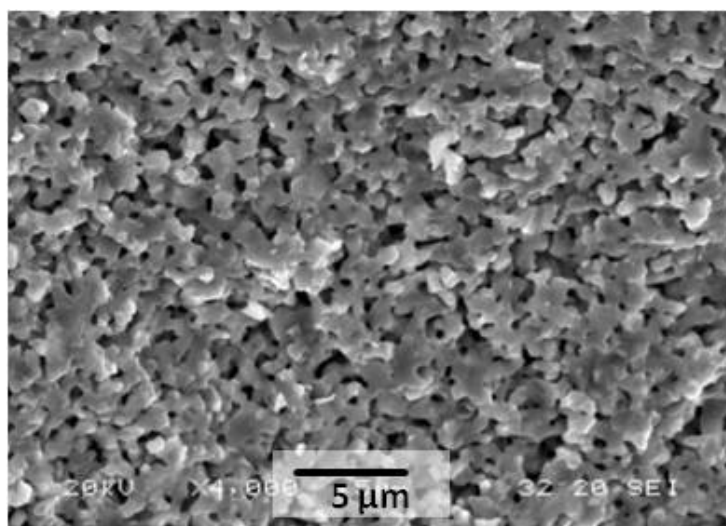


Figure 3.14. Micrograph of the anode microstructure without pore former sintered at 1380°C.

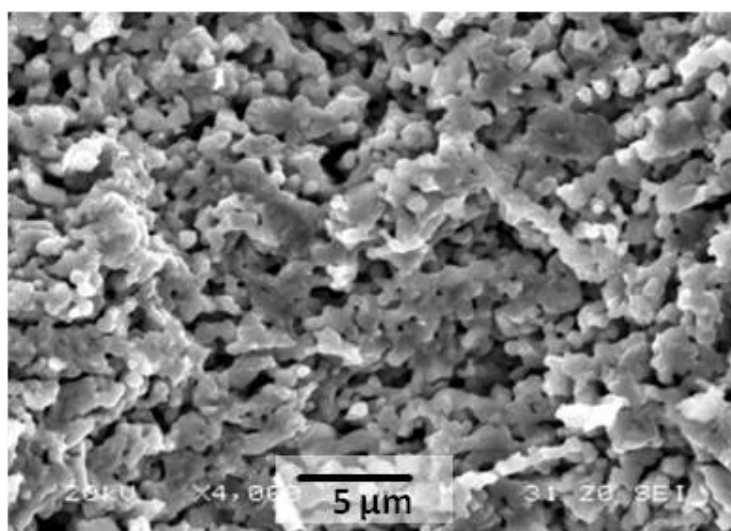


Figure 3.15. Micrograph of the anode microstructure with 5 wt% of pore former sintered at 1380°C.

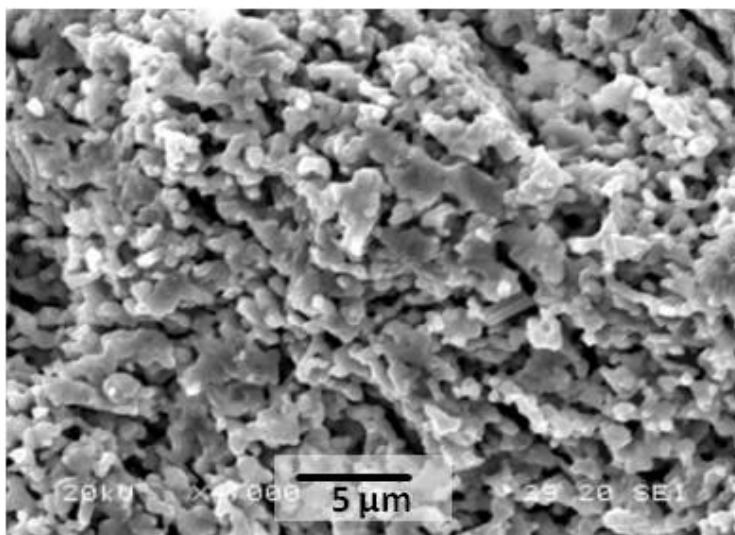


Figure 3.16. Micrograph of the anode microstructure with 8 wt% of pore former sintered at 1380°C.

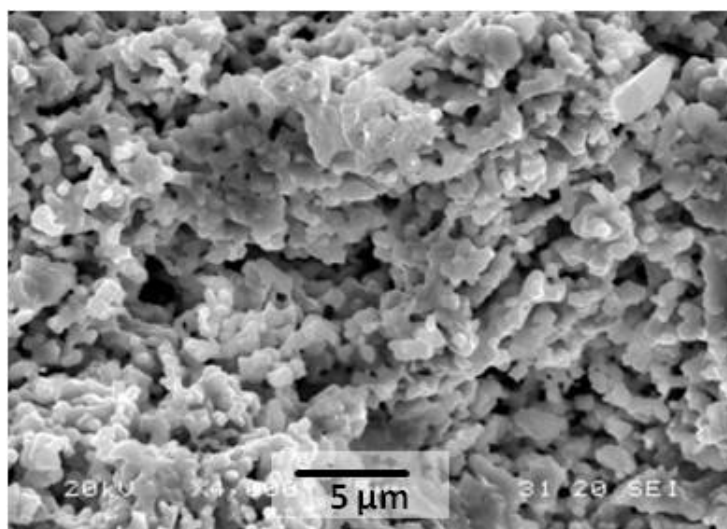


Figure 3.17. Micrograph of the anode microstructure with 10 wt% of pore former sintered at 1380°C.

### 3.2.4 Addition of binder

Due to the large length and complex geometry of the cell supports and the high stresses of layers during drying the addition of binders to the anode and electrolyte slurries was necessary to increase their mechanical strength in green. In addition, the use of binder avoids the separation of graphite in anode slurries.

The amount of binders in the anode and electrolyte slurries was determined in function of their adhesion to the substrates and the homogeneity of thickness along the cell length more than the viscosity.

Slurries with 80 wt% were used to determine the amount of binder in anode and electrolyte slurries. The quantity of binder used for the anode and electrolyte is reported in table 3.4. The amounts of binder can be increased, but a low control of thickness must take into account. On the other hand, if the amount of binder is decreased defects such as cracks and graphite separation can emerge.

Table 3.4. Amount of binder added to the anode and electrolyte slurries

	Binder (wt%)	
	B1014	B1000
Anode	0.02	0.1
Electrolyte	0.05	0.1

### **3.2.5 Cathode porosity**

The porosity of cathode inks was evaluated at different solid loading contents. The procedure to fabricate the samples is similar to that of anode cermet, but in this case the drying was developed at room temperature for 12 h and the sintering temperature was 1150°C for 2 h.

The porosity present in the cathode is generated from the evaporation of terpineol. Thus, the solid loading content has a low impact on the cathode porosity.

The porosity measured at different solid loading content is reported in table 3.5.

Table 3.5. Porosity of cathode at different solid load contents

Solid content (wt%)	Porosity (%)	
	Functional (LSM/YSZ)	Conductive (LSM)
20	36	42
30	36	41
40	38	42
50	38	41

### 3 – Results and Discussion

---

The relatively high porosity of cathode will facilitate the pass of air through the cathode thickness to reach the active sites which reduces the activation and concentration losses. However, ohmic losses should be expected due to the interrupted percolation paths and the lower electric conductivity of porous structures.

The microstructures of the cathode at different solid loads are shown in figures 3.18-3.22. As indicated in the table 3.5 the microstructures of the cathode confirm the similar porosity between the samples with different solid loading contents.

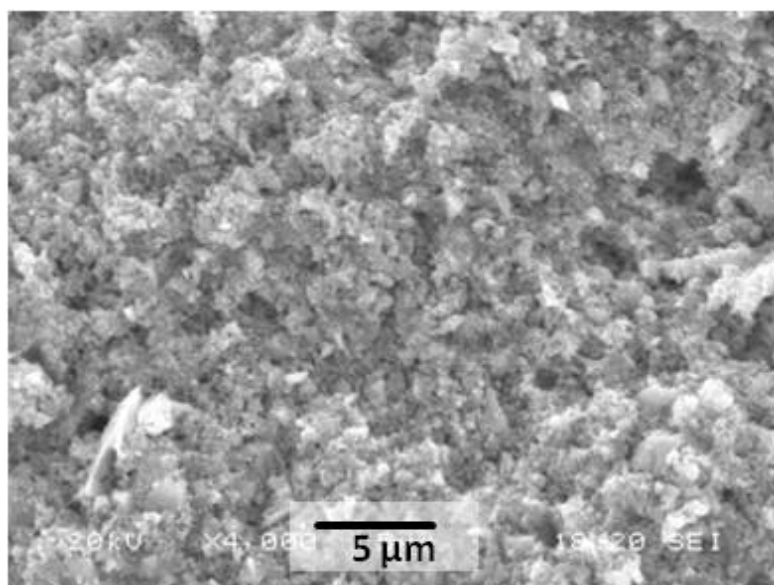


Figure 3.18. Micrograph of the cathode microstructure with LSM pure at 20 wt% sintered at 1150°C.

### 3 – Results and Discussion

---

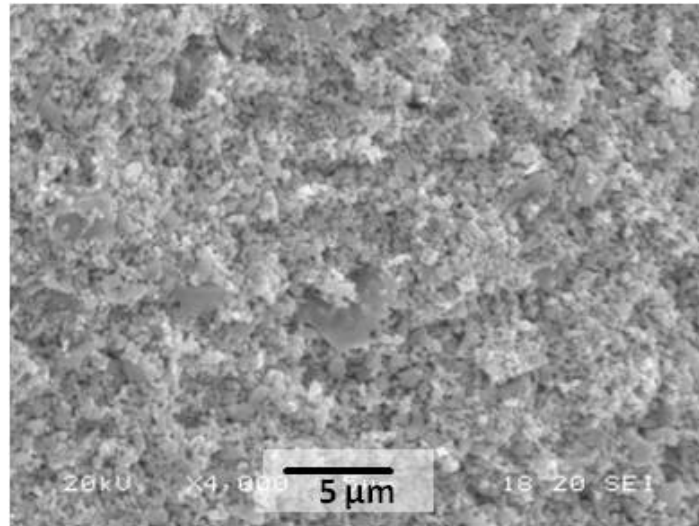


Figure 3.19. Micrograph of the cathode microstructure with LSM/YSZ at 20 wt% sintered at 1150°C.

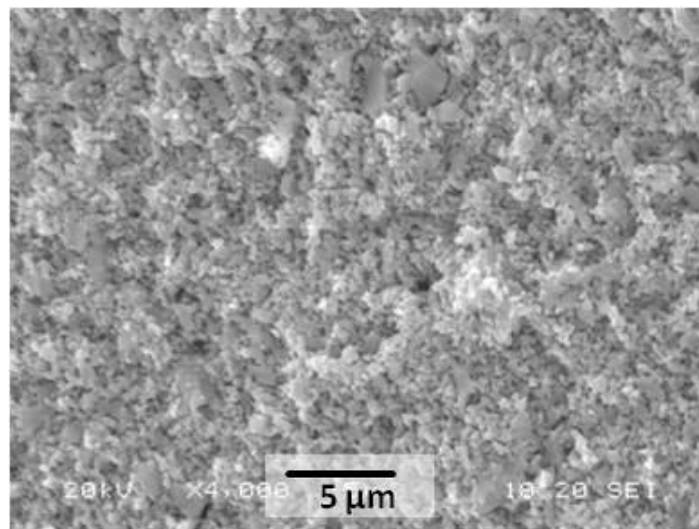


Figure 3.20. Micrograph of the cathode microstructure with LSM/YSZ at 30 wt% sintered at 1150°C.

### 3 – Results and Discussion

---

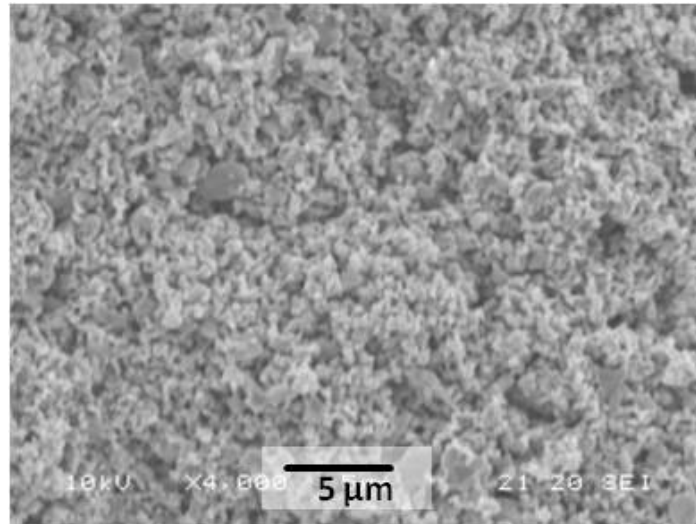


Figure 3.21. Micrograph of the cathode microstructure with LSM/YSZ at 40 wt% sintered at 1150°C.

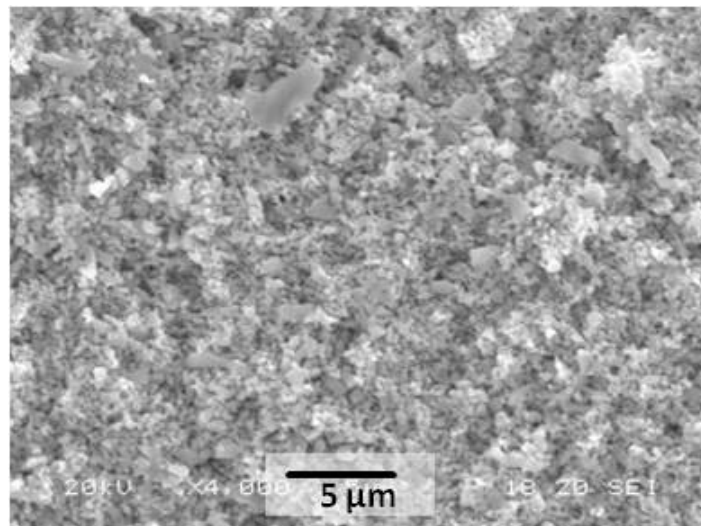


Figure 3.22. Micrograph of the cathode microstructure with LSM/YSZ at 50 wt% sintered at 1150°C.

## **3.3 Production of Micro-Tubular Cells**

### **3.3.1 Dip coating parameters**

The dip coating parameters has a significant effect of the coating thickness. It was confirmed the increase of thickness with high dip/withdrawal speed. On the other hand, at low speed the thickness of the coating is thinner, but the number of dips is increased which cause an accumulation of stresses during the drying step. An intermediate speed was fixed for the deposition of electrodes and electrolyte.

Dwelling time was also useful for the control thickness. In general, longer dwelling times will produce thicker coatings (starting from the second dip). However, large thicknesses show higher stresses during drying. Nevertheless, a dwelling time was benefit for lower solid loading contents. No dwelling time was used for the electrodes, but a dwelling time of 30 seconds was useful for the electrolyte.

Table 3.6 summarizes the dip/withdrawal speed and dwelling time conditions for the electrodes and electrolyte coating.

Table 3.6. Dip coating parameters for the anode, electrolyte and cathode

Parameter	Anode	Electrolyte	Cathode
Dip/withdrawal speed (mm/min)	50	50	50
Dwelling (s)	-	30	-

### 3.3.2 Drying conditions

The drying was the most critical step in the dip coating process. Times and temperatures were analysed for the electrodes and electrolyte. Due to longer rods used as substrate the stresses generated along the length are dependent of the thickness and the solvent content in the suspension. The drying should be fast as possible to avoid the wring of the material deposited. Additionally, a more homogeneous radial drying is favoured with high drying speed which in turns reduces the axial stresses. However, an excessive drying speed creates stresses due to the internal pressure generated by the liquids evaporation. The conditions more convenient for the electrode and electrolyte drying are reported in table 3.7.

Table 3.7. Drying conditions for the anode, electrolyte and cathode

Drying	Anode	Electrolyte	Cathode
Temperature (°C)	100	100	Room
Time (h)	1	1	12

### **3.3.3 Anode coating**

At this point the composition of the anode slurry and the parameters of the dip coating process have been defined, now its solid load content is analysed. It must be noticed that all the solid loads reported correspond to the slurry without additives. In the anode coating is also considered the different geometries of the cell supports used for the fabrication of the two micro-tubular cell configurations evaluated in this study.

Due to the simpler rod geometry of the carbon composite supports the number of dips is increased to reach the thickness desired. However, the more homogeneous thickness along the length facilitates the deposition and drying.

The effect of the solid loading on the anode thickness was the same for both supports. At solid load contents of 60 and 70 wt% many dips are required and cracks are generated for the high stresses produced by repeatedly dry steps. Conversely, at solid load content of 90 wt% only a few dips are required, but the drying of larger thicknesses generates cracks and bubbles too. The samples coated with slurries at solid load contents of 80 and 85 wt% do not present cracks for any of those supports. Furthermore, the number of dips can be decreased by using a solid load of 85 wt%. Therefore, the solid loading for anode slurries was fixed at 85 wt%.

The effect of the solid load contents on the anode coating is reported in table 3.8 and figures 3.23-3.27 show the most common defects on the layers deposited with the respective solid loading content.

### 3 – Results and Discussion

Table 3.8. Effect of solid loading content on the anode coating

Solid load content (wt%)	Number of dips				Observations
	Current collector-supported		Carbon composite-supported		
	Pencil lead	Carbon fibre	Pencil lead	Carbon fibre	
60	12	14	14	16	Radial cracks
70	9	10	11	12	Radial cracks
80	4	5	6	7	Free cracks
85	3	4	5	6	Free cracks
90	2	3	4	5	Radial cracks and bubbles

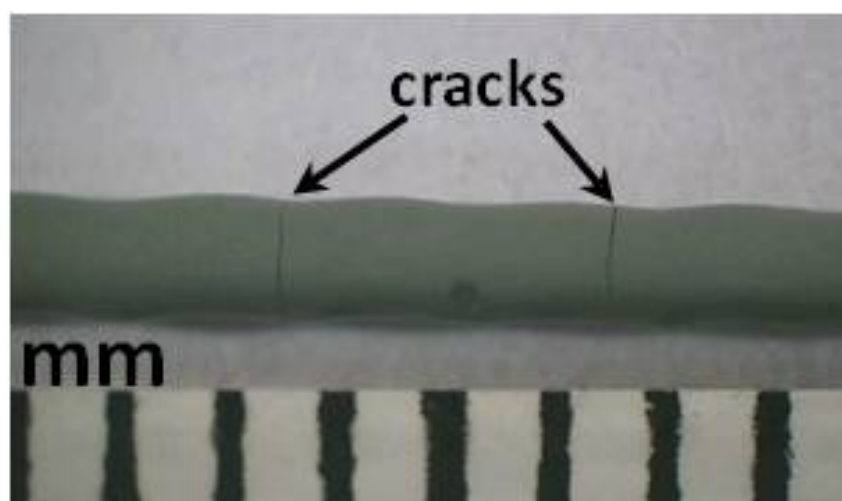


Figure 3.23. Photograph of the anode layer deposited with the slurry at 60 wt% (green state).

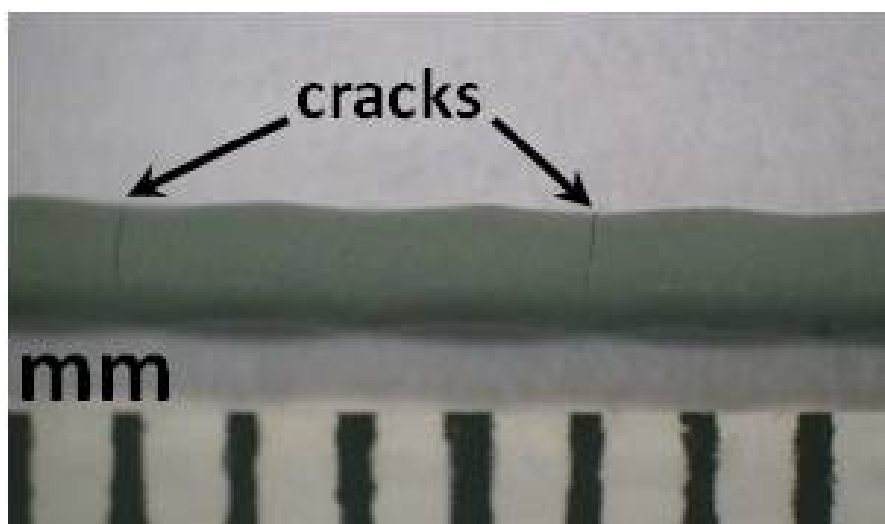


Figure 3.24. Photograph of the anode layer deposited with the slurry at 70 wt% (green state).



Figure 3.25. Photograph of the anode layer deposited with the slurry at 80 wt% (green state).



Figure 3.26. Photograph of the anode layer deposited with the slurry at 85 wt% (green state).

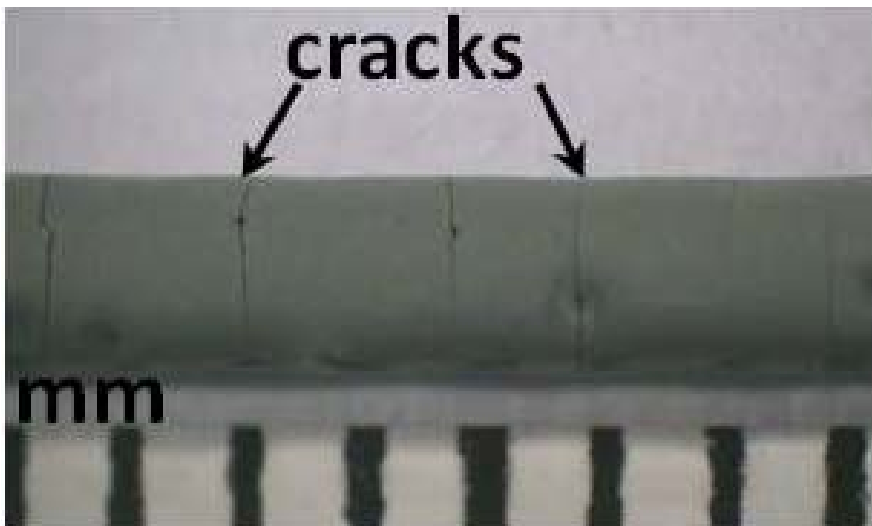


Figure 3.27. Photograph of the anode layer deposited with the slurry at 90 wt% (green state).

### 3.3.4 Electrolyte coating and half-cell co-sintering

The supports with the anode layer were dipped into electrolyte slurries at different solid load contents. The analysis of the electrolyte deposition was focused on the development of a gas tight and thinner electrolyte coating. The number of dips with slurries at different solid loading contents for each support is reported in table 3.9. The figure 3.28 shows the electrolyte layer deposited on the porous anode at green state.

Table 3.9. Effect of solid loading content on the electrolyte coating

Solid load content (wt%)	Number of dips				Observations (After sintering)
	Current collector-supported		Carbon composite-supported		
	Pencil lead	Carbon fibre	Pencil lead	Carbon fibre	
60	2	2	2	2	Cracks and poor adhesion
70	1	1	1	1	Free cracks and thin
80	1	1	1	1	Free cracks and wide

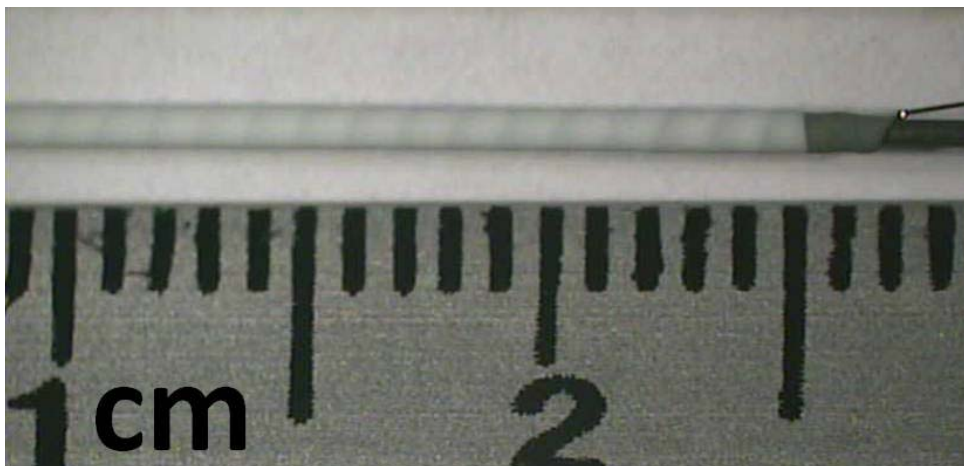


Figure 3.28. Photograph of the electrolyte deposited with the slurry at 70 wt% (green state).

The condition of the electrolyte coating was evaluated after the sintering at 1380°C. Figures 3.29-3.34 show the electrolyte deposited of different solid load contents after sintering. The inner coaxial diameter of the half-cells and the presence of the nickel wire within the anode are also clearly distinguished. The thickness of the electrolyte is increased as the solid loading content increase. At 60 wt% the thickness of the electrolyte is around 10-12  $\mu\text{m}$ , but was not effectively adhered to the porous anode and cracks. At 70 and 80 wt% the adhesion to the anode was good and the thickness was in the range of 25-30  $\mu\text{m}$  and 80  $\mu\text{m}$ , respectively. Thus, the solid loading content for the electrolyte coating was fixed at 70 wt%.

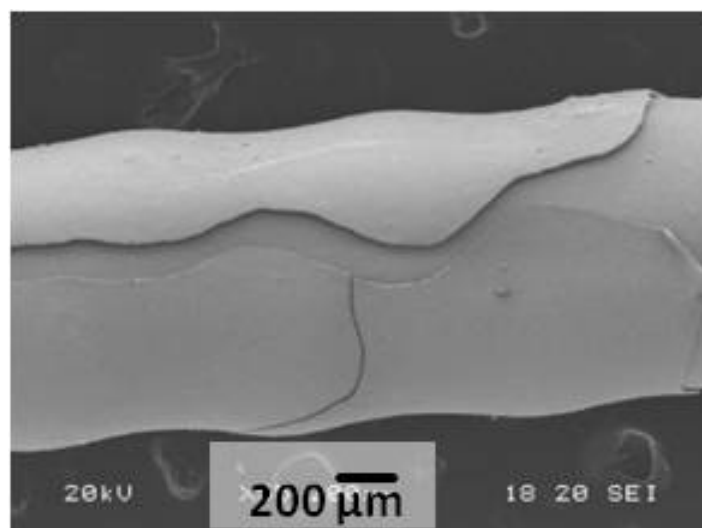


Figure 3.29. Micrograph of the half-cell length with the electrolyte at 60 wt% sintered at 1380°C.

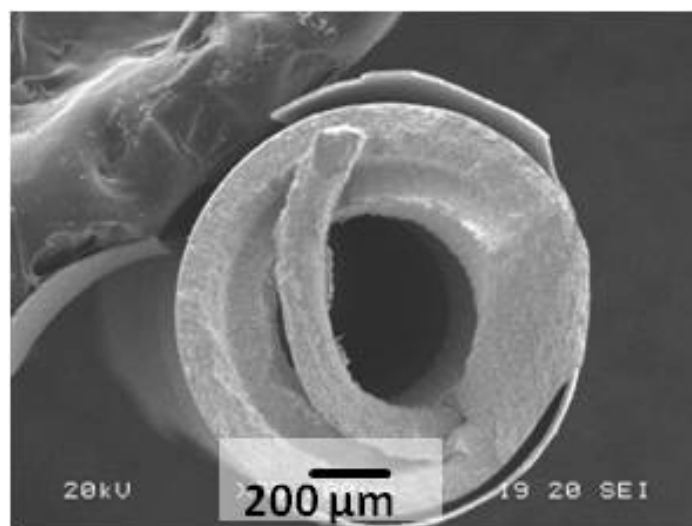


Figure 3.30. Micrograph of the half-cell diameter with the electrolyte at 60 wt% sintered at 1380°C.

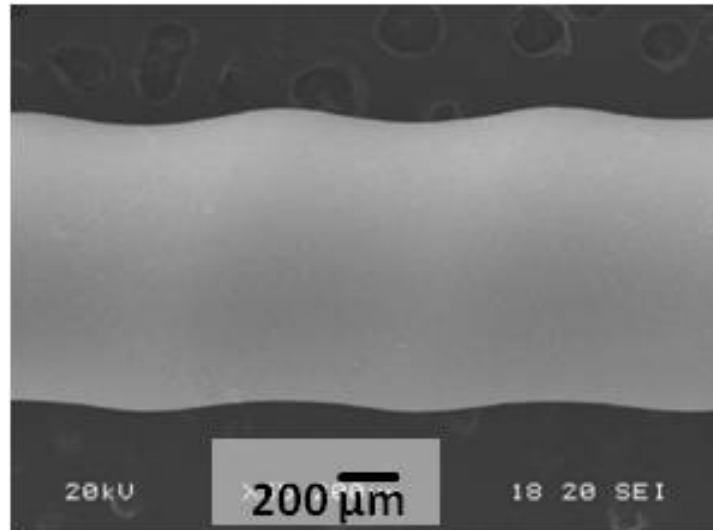


Figure 3.31. Micrograph of the half-cell length with the electrolyte at 70 wt% sintered at 1380°C.

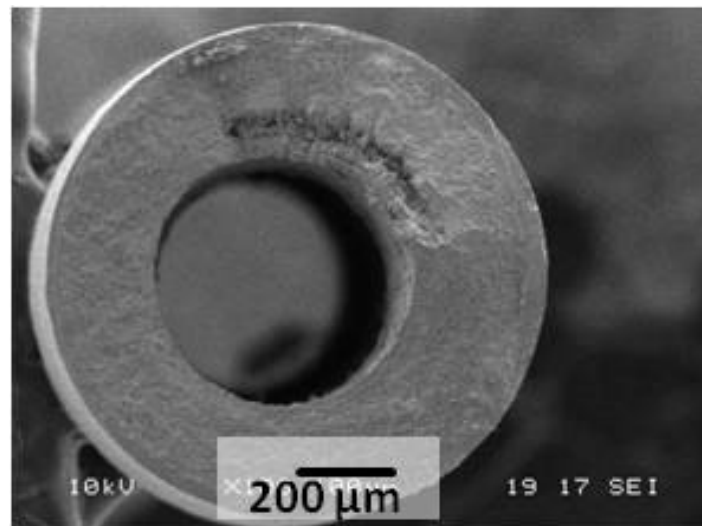


Figure 3.32. Micrograph of the half-cell diameter with the electrolyte at 70 wt% sintered at 1380°C.

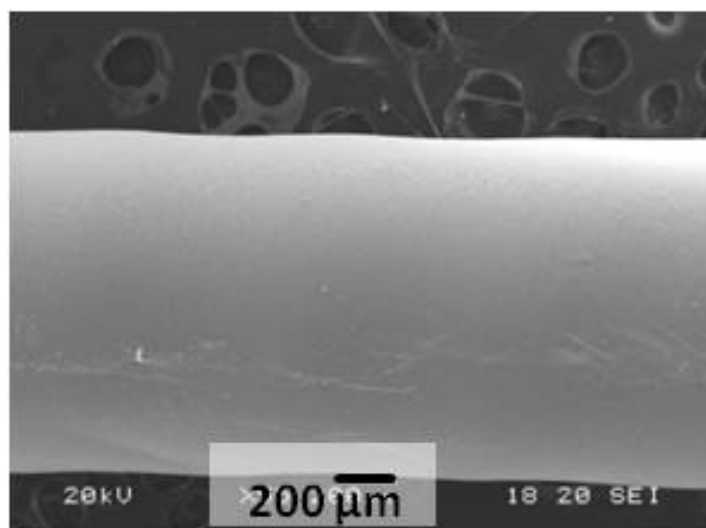


Figure 3.33. Micrograph of the half-cell length with the electrolyte at 80 wt% sintered at 1380°C.

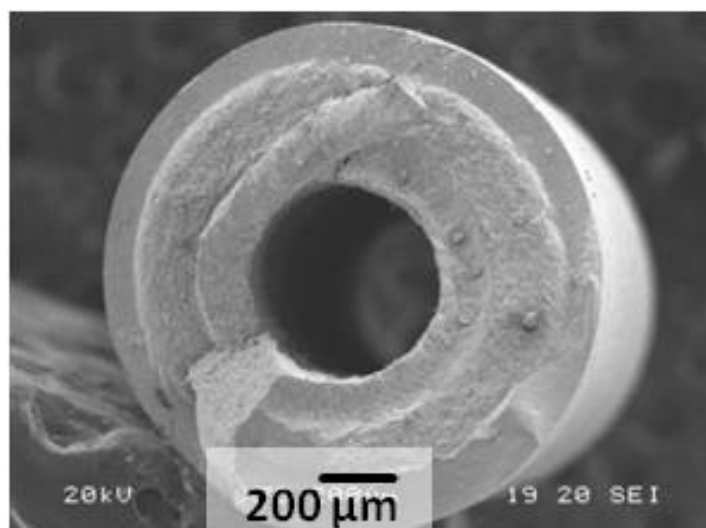


Figure 3.34. Micrograph of the half-cell diameter with the electrolyte at 80 wt% sintered at 1380°C.

### **3.3.5 Remains from carbon composites**

The remains from the pencil leads and carbon fibre after sintering were analysed microscopically. The half-cells produced with carbon fibre and pencil leads are compared in figure 3.35.

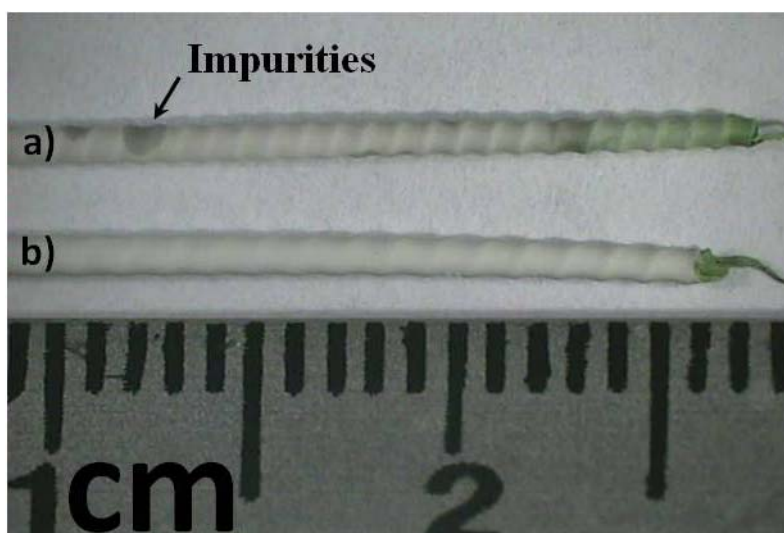


Figure 3.35. Photograph of the half-cells with pencil lead (a); and carbon fibre (b) as sacrificial inner core sintered at 1380°C.

The carbon fibres used in this study are based Polyacrylonitrile polymers (PAN) and after the pyrolysis treatment at 800°C any remain was detected (figure 3.35 (b)).

In the case of the pencil leads some remains are clearly seen in figure 3.35 (a). These impurities come from the “writing core” which is made from

### 3 – Results and Discussion

---

a mixture of graphite, wax, oils and clay, the latter of which is the binding agent [146].

The presence of the impurities remained from the pyrolysis of the pencil lead onto the inner anode surface is shown in figure 3.36.

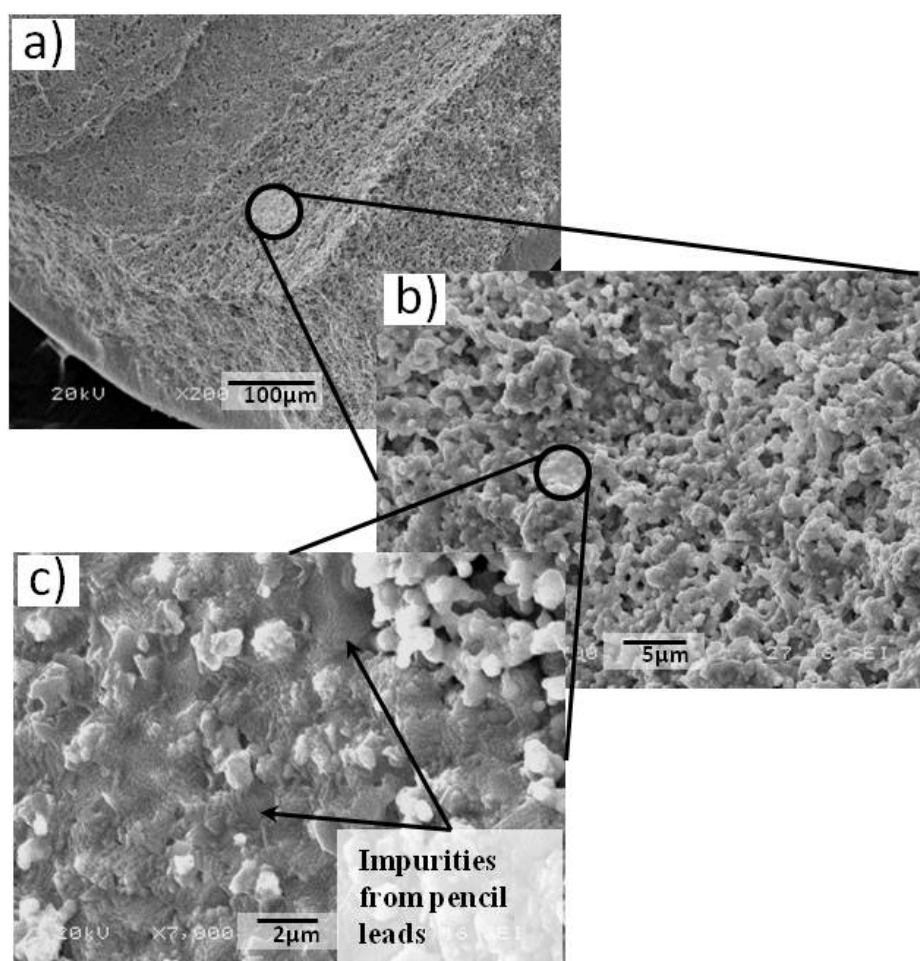


Figure 3.36. Micrograph of the remains deposited onto the inner anode surface: (a) longitudinal-section view; (b), (c) surface view at different magnifications.

The remains deposited onto the inner anode surface will cause a slight reduction in the porosity. As the remains are detected only in small areas along the cell length the effect in the reduction of porosity should not be significant. Nevertheless, ohmic losses should be expected in the electrochemical testing due to the low electric conductivity of the clay potentially present into the anode.

### **3.3.6 Cathode coating**

In order to complete the cells was proceeded to the cathode deposition onto the half-cell. The bilayer-structured cathode coating was achieved by using inks with different solid load contents.

The half-cells were dipped into the functional and conductive cathode inks once. Using solid load contents between 30 and 50 wt% the layers were heterogeneous along the length due to the wring caused for the longer drying times. At 20 wt% the layer was thinner and well controlled, thus this solid contend was fixed for the cathode deposition.

The cathode thickness after sintering was below 50  $\mu\text{m}$ . Figure 3.37 shows the complete current collector-supported micro-tubular cell after the cathode sintering.

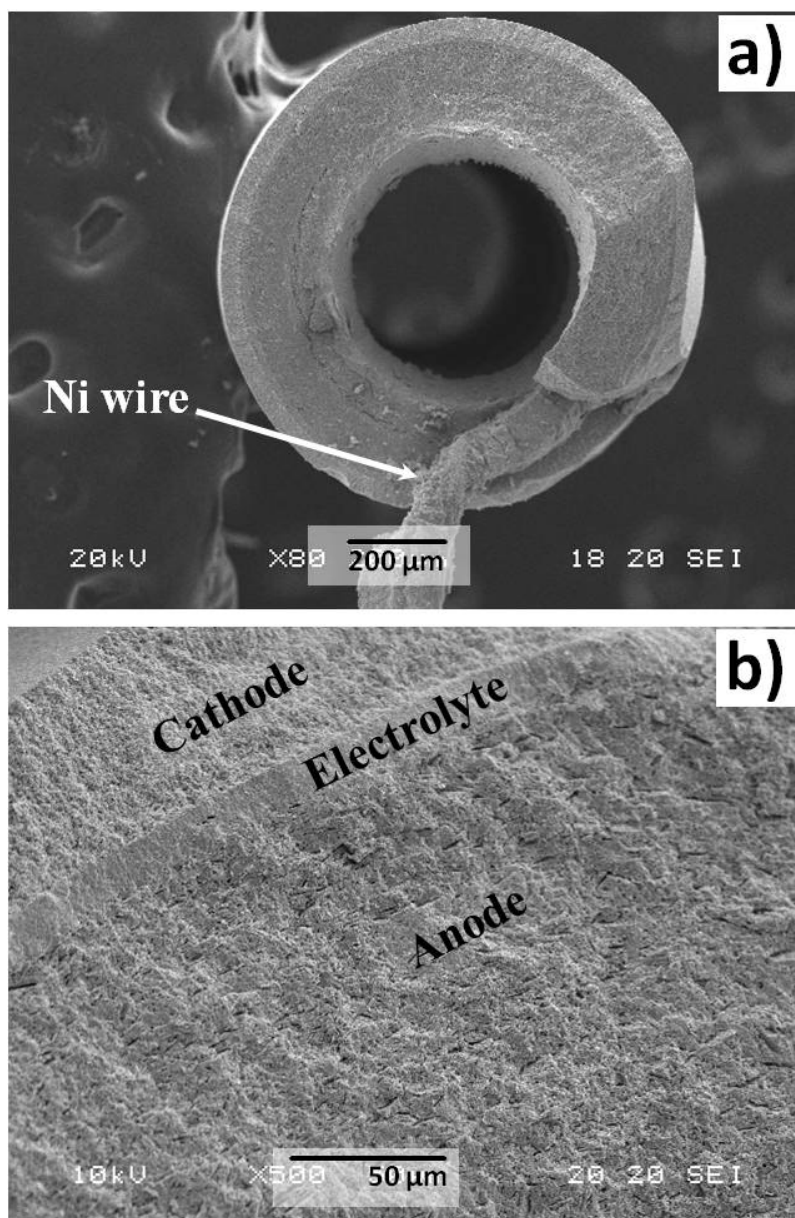


Figure 3.37. Micrographs of the complete current collector-supported cell: (a) cross-section overview; (b) surface view at higher magnification.

## 3.4 Performance analysis of Micro-Tubular Cells

### 3.4.1 Cells size

The dimensions of the cells used in the electrochemical testing are reported in table 3.10. The dimensions are analogous for both produced cells. Figure 3.38 shows the comparison of the two reported cells. It is clearly seen that the terminals of the coil-supported nickel wire (top) are available for the electrical connection; while the common tubular cell (bottom) needs the insertion of the straight nickel wire as current collector.

Table 3.10. Dimensions of the micro-tubular cells produced

	Average
Anode thickness ( $\mu\text{m}$ )	~200
Electrolyte thickness ( $\mu\text{m}$ )	20-30
Cathode thickness ( $\mu\text{m}$ )	<50
Inner diameter ( $\mu\text{m}$ )	~400
Outer diameter (mm)	<1.2
Cell length (mm)	~30
Cathode effective length (mm)	~20
Cathode active area ( $\text{cm}^2$ )	~0.75

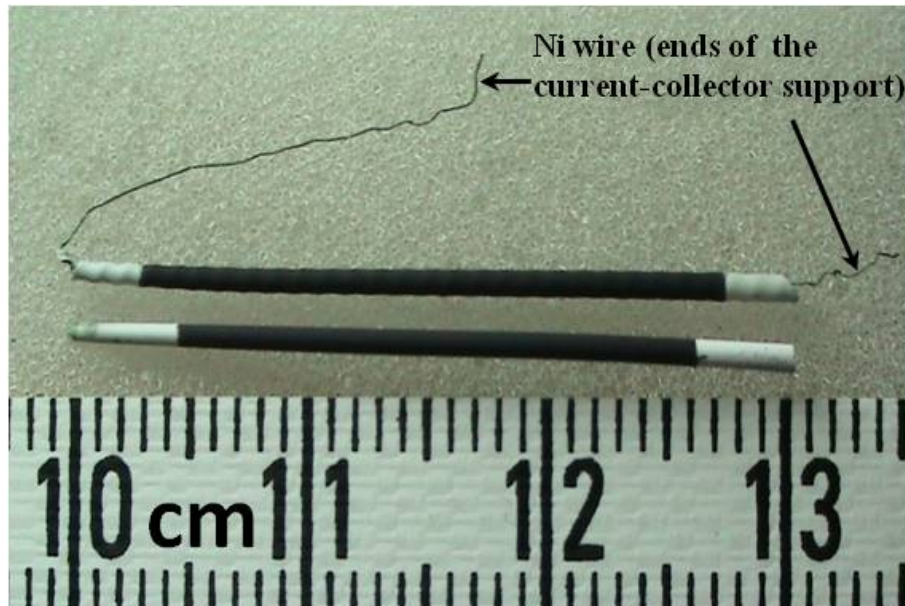


Figure 3.38. Photograph of the complete current collector-supported (top) and common (bottom) micro-tubular cell.

### 3.4.2 Current paths

As mentioned in previous sections, one of the major advantages of the current collection method developed in this study is the reduction of current paths in tubular geometry. This current collection method not only reduces the current paths but the percolation threshold along the anode thickness too. Although the nickel content in the anode cermet ensures a high electrical conductivity the porosity and thickness of the cermet can reduce the percolation paths causing ohmic losses. If a nickel wire is integrated within the anode, the overall nickel content is increased, thus increasing the

effective percolation paths. The effect in percolation and current paths by using an integrated current collector is shown in figure 3.39 and 3.40, respectively. It can be seen that the number of effective percolation paths is increased when the current collector is within the anode (figure 3.39 (b)). This benefits porous materials where the continuity of the percolation paths is interrupted.

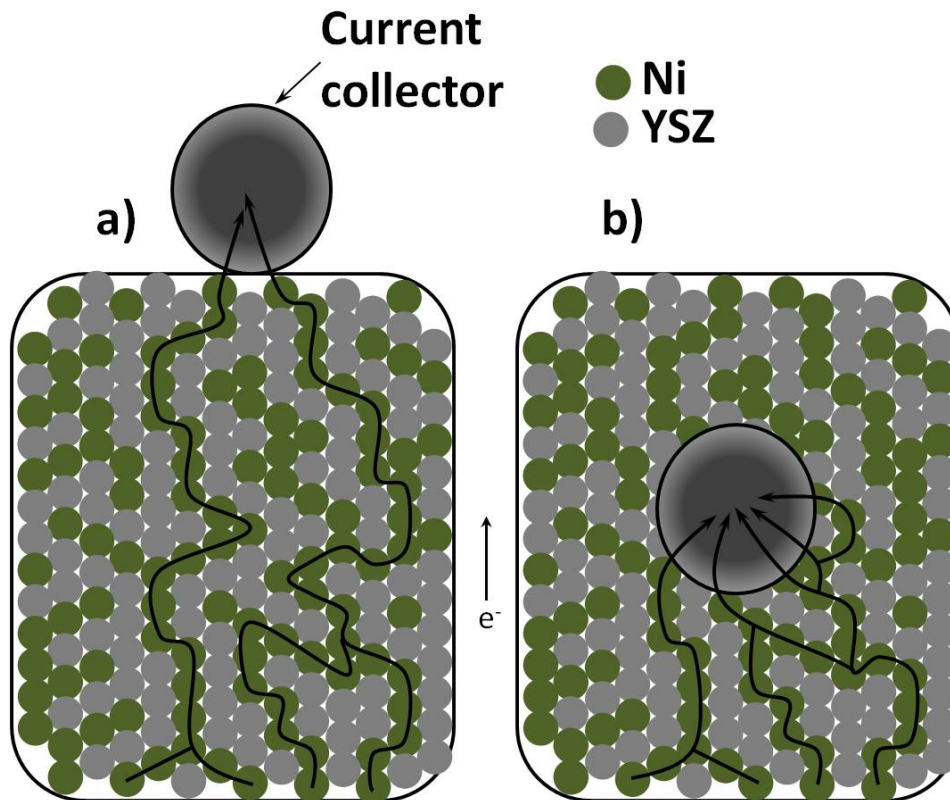


Figure 3.39. Schematic diagram of the effect of a superficial (a) and integrated (b) current collector on the percolation paths in the anode cermet. Arrows indicate the effective percolation paths.

The current paths shown in figure 3.40 are clearly shorter than those described in previous sections. Thus, the current collector-supported cells should offer a significant ohmic losses reduction.

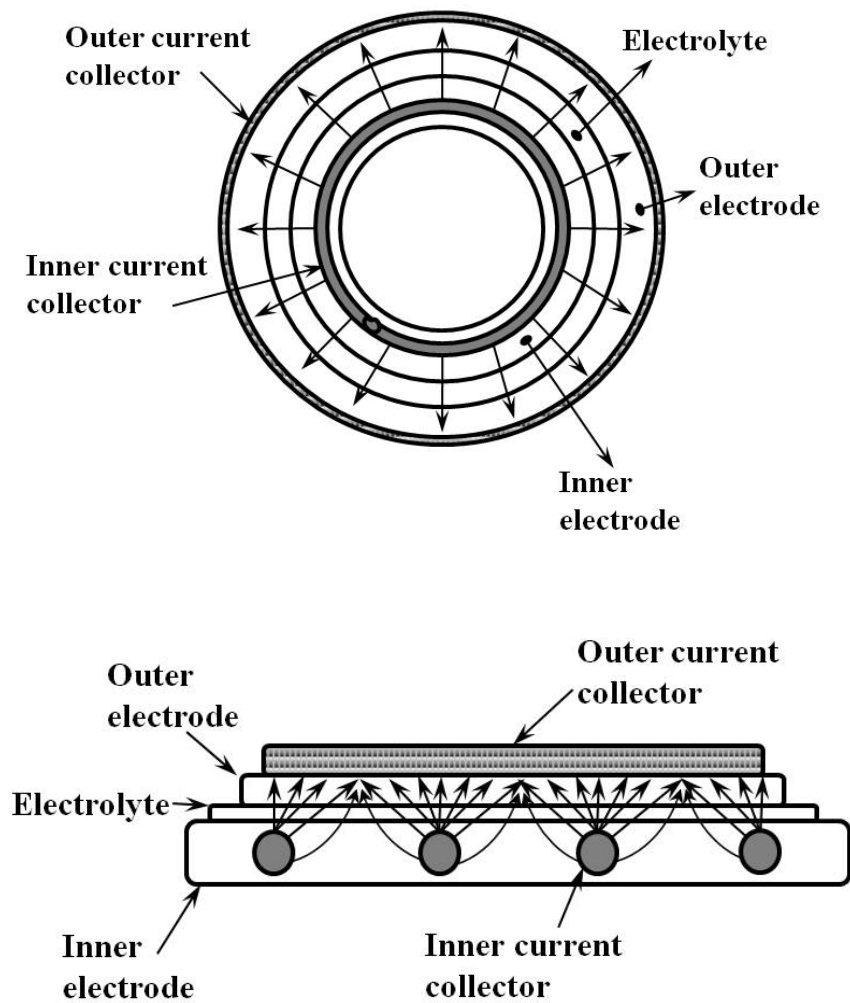


Figure 3.40. Schematic diagram of the current path in radial and axial direction by using the current collector-supported method.

### **3.4.3 Performance of current collector-supported cells**

The longitudinal-section view of the current collector-supported cell is presented in figure 3.41. The embedment of nickel wire within the anode cermet is clearly seen.

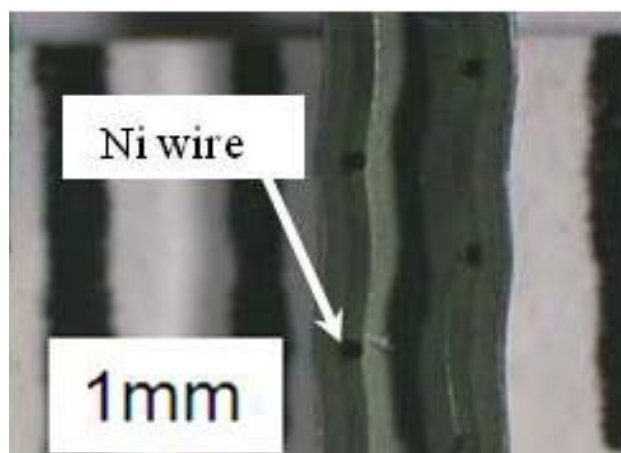


Figure 3.41. Photograph of the longitudinal-section view of the current collector-supported cell.

#### ***3.4.3.1 Carbon fibre sacrificial core***

The performance of the current collector-supported micro-tubular cell with carbon fibre as sacrificial inner core is shown in figure 3.42. The open circuit voltage (OCV) achieved was 0.94 V; this voltage was slightly lower

than expected possibly caused by a gas leakage in the electrolyte. The peak power outputs were 92, 142 and 202 mW/cm<sup>2</sup> at 700, 750 and 800°C, respectively.

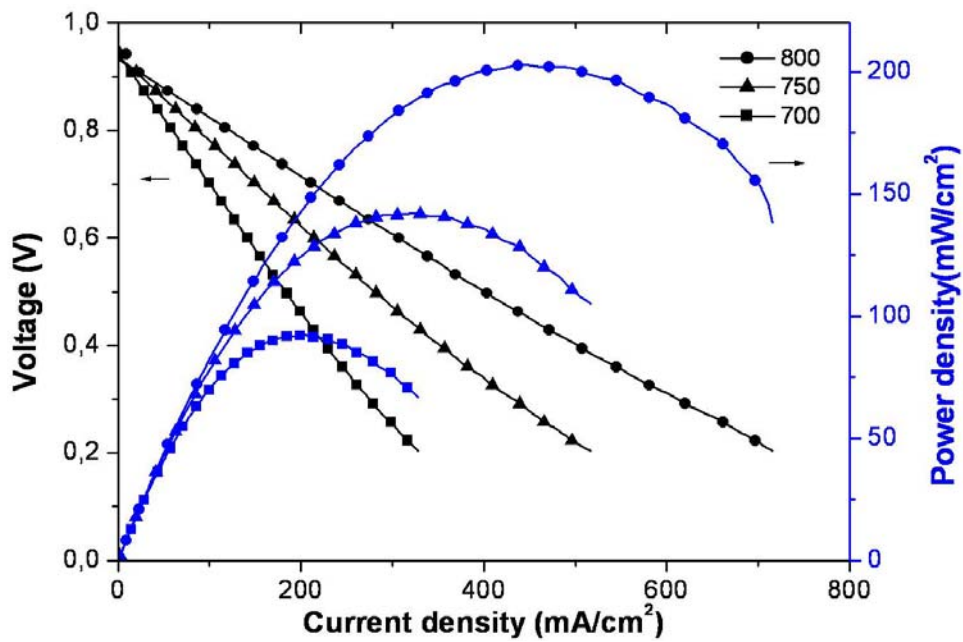


Figure 3.42. Performance of current collector-supported micro-tubular cell with carbon fibre as sacrificial inner core.

### 3.4.3.2 Pencil lead sacrificial core

The performance of the current collector-supported micro-tubular cell with pencil lead as sacrificial inner core is shown in figure 3.43. In this case, the OCV was 0.93 V and the maximum power outputs were 56, 112 and 190

$\text{mW}/\text{cm}^2$  at 700, 750 and 750°C, respectively. The power density of the cells made using pencil leads shows a barely lower performance in comparison with those fabricated with the carbon fibre at 800°C, but becomes more significant as decrease the temperature. This result suggests that the remains of the pencil leads have a low detrimental effect on the performance of cell, especially at high temperatures. Additionally, the OCV values obtained in both cells are similar, thus the remains do not affect the gas tightness of the electrolyte.

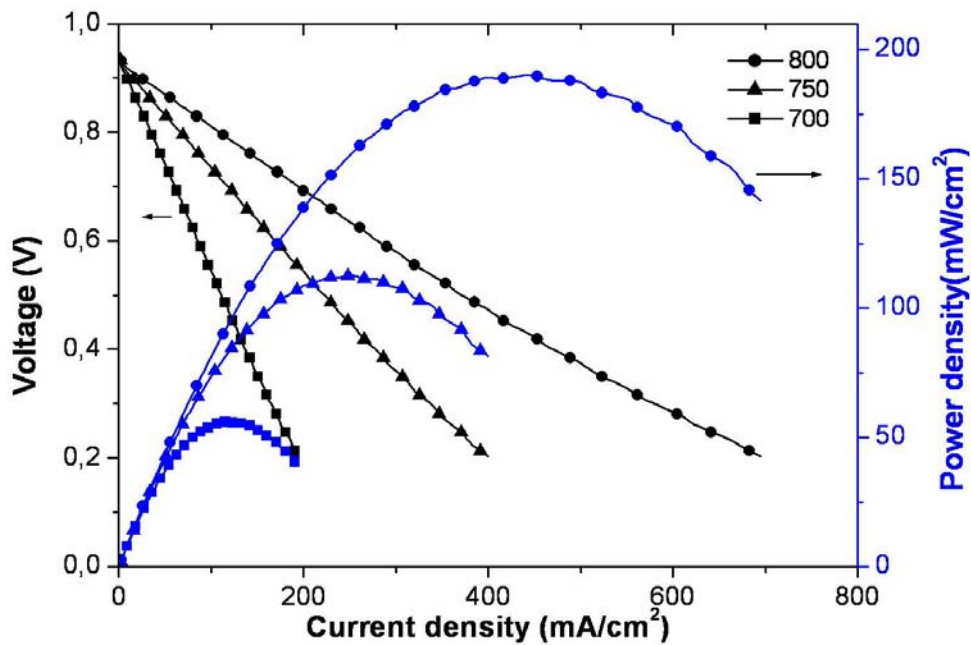


Figure 3.43. Performance of current collector-supported micro-tubular cell with pencil lead as sacrificial inner core.

### **3.4.4 Performance of cells with straight wire within the cell core**

The longitudinal-section view of the tubular cell for testing with the common current collection methods is show in figure 3.44.

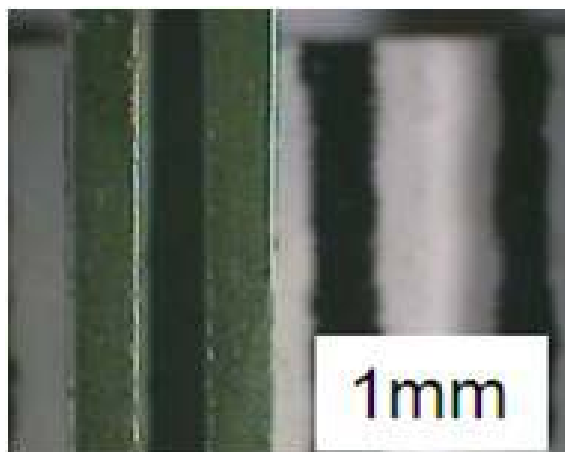


Figure 3.44. Photograph of the longitudinal-section view of the cell tested with a common current collector.

#### ***3.4.4.1 Carbon fibre sacrificial core***

The performance of the micro-tubular cell with carbon fibre as sacrificial inner core is shown in figure 3.45. The OCV achieved (1.06 V) indicates a denser without leakage electrolyte layer. The peak power outputs were 18, 34 and 55 mW/cm<sup>2</sup> at 700, 750 and 800°C, respectively. These

performances are 3-4 times lower than those reported for the current collector-supported cells, thus the effectiveness of the innovative current collection methods has been demonstrated.

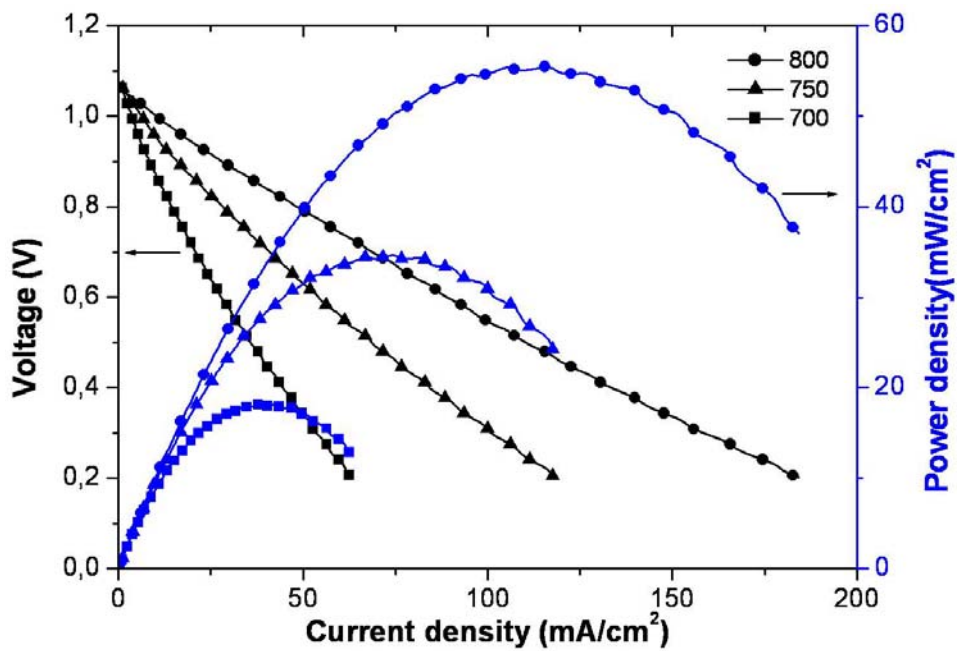


Figure 3.45. Performance of the micro-tubular cell with carbon fibre as sacrificial inner core and straight wire within the cell core as current collector.

#### 3.4.4.2 Pencil lead sacrificial core

The performance of the cells with the common current collector method and pencil lead as core shown the lowest performance registered among the different cases (figure 3.46). Here, the effect of the remains on the cell

### 3 – Results and Discussion

performance also reduced the overall cell performance in similar ratio than the current collector-supported cells. The OCV achieved was 1.08 V and the maximum power densities were 13, 23 and 43 mW/cm<sup>2</sup> at 700, 750 and 800°C, respectively.

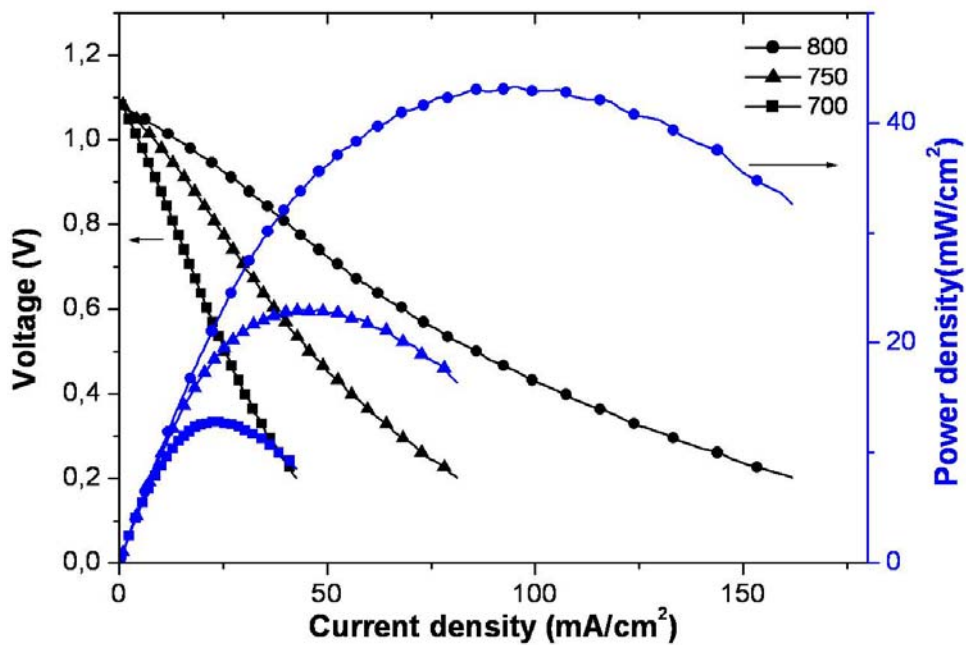


Figure 3.46. Performance of the micro-tubular cell with pencil lead as sacrificial inner core and straight wire within the cell core as current collector.

# 4. Conclusions

---

## 4.1 Cell Supports

Commercial carbon composites materials such as pencil leads and carbon fibre were successfully used as sacrificial inner core for the production of micro-tubular SOFC.

The pencil leads offer the most economic option, but many drawbacks were observed. The difference in compositions between marks and batches can not ensure constant chemical composition and therefore the thermal behaviour and additive traces change, too. Furthermore, the sizes of the pencil leads are established and it is not possible change the length for the production of longer cells. Additionally, the fragility of pencil leads becomes a problem during processing.

The carbon fibres are relatively more expensive material, but the benefits offered in the production of the micro-tubular cells were invaluable. The composition of the carbon fibre is completely defined, thus the thermal and physical properties are quite constant. The most important characteristics of the carbon fibre are the high flexural resistance and the

null presence of remains after pyrolysis. Moreover, longer carbon fibre lengths are commercially available.

The number of turns per centimetre along the cores was effectively controlled by using an engine. Although the 0.05 and 0.1 mm wire diameters were successfully coiled around the cores only the thicker wire kept enough mechanical resistance after the pyrolysis treatment.

## **4.2 Production of Micro-Tubular Cells**

Micro-tubular cells with two different configurations were successfully produced by sequentially dip coating.

The most proper conditions in porosity, thermal behaviour, dip coating parameters, solid loading contents, sintering temperatures and atmospheres were established for the production of these devices.

Good reproducibility in the two micro-tubular cells configurations was achieved. Nevertheless, the processing of cells produced with pencil leads was much more arduous due to the fragility of the pencil leads during the coating and drying steps.

## **4.3 Performance of Micro-Tubular Cells**

The efficiency of the innovative current collector developed in this study was demonstrated. The current collector method reported enhances significantly the overall performance of micro-tubular cells by shorter current paths.

The power density achieved with the current collector-supported micro-tubular cells with diameter below 1.2 mm and a cathode active area of  $\sim 0.75 \text{ cm}^2$  was in good agreement with the current state of the art for analogous devices.

The performances of cells with pencil lead as sacrificial core were lower than those with carbon fibre due to the effect of the impurities on porosity and electrical conductivity of the anode cermet.

## **4.4 Future work**

Currently, different approaches are being analysed for the improvement of the current collector-supported micro-tubular cells reported in this study. The most concern issues includes: (i) the effect of the number of turns per centimetre around the cores on the cell performance, (ii) improvement of

#### 4 – Conclusions

---

the cermet microstructure by using functional anode layer, (iii) impedance analysis on cells to distinguish the polarization contributions, (iv) effect of the current collector on the mechanical properties of the micro-tubular cells, (v) development of a coating technique in which the sacrificial core would not be necessary and (vi) development of cells for intermediate temperature by using new materials for anode and electrolyte.

# References

---

1. D.J.L. Brett, A. Atkinson, N.P. Brandon and S.J. Skinner, "Intermediate temperature solid oxide fuel cells", *Chem. Soc. Rev.*, 37 [3] (2008) 1568-78.
2. N.Q. Minh, "Ceramic fuel cells", *J. Am. Ceram. Soc.*, 76 [3] (1993) 563-88.
3. L.J.M.J. Blomen and M.N. Mugerwa, "Fuel cell systems", *Plenum Press*, New York, (1993).
4. W.Z. Zhu and S.C. Deevi, "A review on the status of anode materials for solid oxide fuel cells", *Material Science and Engineering A*, 362 [1-2] (2003) 228-39.
5. K. An, "Mechanical properties and electrochemical durability of solid oxide fuel cells", PhD Thesis, Virginia Polytechnic Institute and State University, USA, (2003).
6. S.C. Singhal and K. Kendall, "High temperature solid oxide fuel cells: fundamentals, design and applications", Oxford, UK, Elsevier Ltd., (2003).
7. S.C. Singhal, "Solid oxide fuel cells for stationary, mobile, and military applications", *Solid State Ionics*, 152-153 (2002) 405-10.
8. G.T. Lee and F.A. Sudhoff, "Fuel cell/gas turbine system performance studies", *Fuel-Cells Review Meeting*, FETC Publication, Department of Energy, USA (1996) 12-31.
9. S.E. Veyo and W.L. Lundberg, "Solid oxide fuel cell power system cycles", *International Gas Turbine Institute*, ASME paper 99-GT-356, Indianapolis (1999).
10. D. Dong, M. Liu, Y. Dong, B. Lin, J. Yang and G. Meng, "Improvement of the performances of tubular solid oxide fuel cells by

## References

---

- optimizing co-sintering temperature of the NiO/YSZ anode-YSZ electrolyte double layers”, *J. Power Sources*, 171 [2] (2007) 495-8.
11. M.C. Williams, J. Strakey and W. Sudoval, “U.S. DOE fossil energy fuel cells program”, *J. Power Sources*, 159 [2] (2006) 1241-7.
  12. J. Zizelman, S. Shaffer and S. Mukerjee, “Solid oxide fuel cell auxiliary power unit-A developed update”, SAE Paper 2002-01-0411 (2002).
  13. J.J. Botti, M.J. Grieve and J.A. Macbain, “Electric vehicle range extension using an SOFC APU”, SAE Paper 2005-01-1172 (2005).
  14. W. Münch, H. Frey, M. Edel and A. Kessler, “Stationary fuel cells-results of 2 years of operation at EnBW”, *J. Power Sources*, 155 [2] (2006) 77-82.
  15. M. Sorrentino, C. Pianese and Y.G. Guezennec, “A hierarchical modeling approach to the simulation and control of planar solid oxide fuel cells”, *J. Power Sources*, 180 [1] (2008) 380-92
  16. D.A. Noren and M.A. Hoffman, “Clarifying the Butler-Volmer equation and related approximations for calculating activation losses in solid oxide fuel cell models”, *J. Power Sources*, 152 (2005) 175-81.
  17. EG&G Technical Services, Inc. Fuel Cell Handbook (Seventh edition), Morgantown, West Virginia, USA: U.S. Department of Energy, (2004).
  18. S. Campanari and P. Iora, “Definition and sensitivity analysis of a finite volume SOFC model for tubular cell geometry”, *J. Power Sources*, 132 [1-2] (2004) 113-26.
  19. J. Jia, R. Jiang, S. Shen and A. Abudula, “Effect of operation parameters on performance of tubular solid oxide fuel cell”, *J. American Institute of Chemical Engineering*, 54 [2] (2008) 554-64.
  20. J. Larminie and A. Dicks, “Fuel cell systems explained”, John Wiley & Sons Ltd, Second edition (2003).
  21. E. Fabbri, “Tailoring materials for intermediate temperature solid oxide fuel cells (IT-SOFCs) based on ceramic proton conducting electrolyte”, PhD Thesis, Università degli studi di Roma, Italy, (2009).
  22. S.H. Chan, K.A. Khor and Z.T. Xia, “A complete polarization model of a solid oxide fuel cell and its sensitivity to the change of cell component thickness”, *J. Power Sources*, 93 [1-2] (2001) 130-40.

## References

---

23. C. Ciano, "Different approaches to the modeling of tubular solid oxide fuel cells", PhD Thesis, Politecnico di Torino, Italy, (2008).
24. B. Boer, "SOFC Anodes: Hydrogen oxidation at porous nickel and nickel/yttria-stabilized zirconia cermet electrodes", PhD Thesis, University of Twente, Netherlands, (1998).
25. M. Cologna, "Advances in the production of planar and micro-tubular solid oxide fuel cells", PhD Thesis, Università degli studi di Trento, Italy, 2009.
26. O. Yamamoto, "Solid oxide fuel cells: fundamental aspects and prospects", *Electrochimica Acta*, 45 [15-16] (2000) 2423-35.
27. J.W. Fergus, "Electrolytes for solid oxide fuel cells", *J. Power Sources*, 162 [1] (2006) 30-40.
28. K. Nomura, Y. Mizutani, M. Kawai, Y. Nakamura and O. Yamamoto, "Aging and Raman scattering study of Scandia and yttria doped zirconia", *Solid State Ionics*, 132 [3-4] (2000) 235-9.
29. V.V. Kharton, F.M.B. Marques and A. Atkinson, "Transport properties of solid oxide electrolyte ceramics: a brief review", *Solid State Ionics*, 174 (2004) 135-49.
30. J.W. Fergus, "Doping and defect association in oxide for use in oxygen sensors", *J. Mater. Sci.*, 38 [21] (2003) 4259-70.
31. R. Pornprasertsuk, P. Ramanarayanan, D.B. Musgrave and F.B. Prinz, "Predicting ionic conductivity of solid oxide fuel cell electrolyte from first principles", *J. Appl. Phys.*, 98 [103513] (2005).
32. I. Taniguchi, R.C. van-Landschoot and J. Schoonman, "Electrostatic spray deposition of  $Gd_{0.1}Ce_{0.9}O_{1.95}$  and  $La_{0.9}Sr_{0.1}Ga_{0.8}Mg_{0.2}O_{2.87}$  thin films", *Solid State Ionics*, 160 [3-4] (2003) 271-9.
33. M. Mogensen, N.M. Sammes and G.A. Tompsett, "Physical, chemical and electrochemical properties of pure and doped ceria", *Solid State Ionics*, 129 [1-4] (2000) 63-94.
34. C. Kleinlogel and L.J. Gauckler, "Sintering and properties of nanosized ceria solid solutions", *Solid State Ionics*, 135 [1-4] (2000) 567-73.
35. M. Gödickemeier, K. Sasaki and L.J. Gauckler, "Electrochemical characteristics of cathodes in solid oxide fuel cells based on ceria electrolytes", *J. Electrochem. Soc.*, 144 [5] (1997) 1635-46.

## References

---

36. D. Perednis and L.J. Gauckler, "Solid oxide fuel cells with electrolytes prepared via spray pyrolysis", *Solid State Ionics*, 166 [3-4] (2004) 229-39.
37. J.L.M. Rupp, A. Infortuna, and L.J. Gauckler, "Thermodynamic stability of gadolinia-doped ceria thin film electrolytes for micro-solid oxide fuel cells" *J. Am. Ceram. Soc.*, 90 [6] (2007) 1792-7.
38. A.V. Joshi, J.J. Steppan, D.M. Taylor and S. Elangovan, "Solid electrolyte materials, devices, and applications", *J. Electroceram.*, 13 [1-3] (2004) 619-25.
39. M. Liu, M. Shi, C. Wang, Y.P. Yuan, P. Majewski and F. Aldinger, "Microstructure and ionic conductivity of Sr-and Mg-doped LaGaO<sub>3</sub>", *J. Mater. Sci.*, 41 [13] (2006) 4205-13.
40. T. Ishihara, M. Enoki, J.W. Yan and H. Matsumoto in: S.C. Singhal and J. Mizusaki (Eds.), *Proceedings of the Ninth International Symposium on Solid Oxide Fuel Cells*, Quebec, Canada, (2005) 1117.
41. J.W. Stevenson, K. Hasinska, N.L. Canfield and T.R. Armstrong, "Influence of cobalt iron additions on the electrical and thermal properties of (La,Sr)(Ga,Mg)O<sub>3-δ</sub>", *J. Electrochem. Soc.*, 147 [9] (2000) 3213-8.
42. B.A. Khorkounov, H. Näfe and F. Aldinger, "Relationship between the ionic and electronic partial conductivities of co-doped LSGM ceramics from oxygen partial pressure dependence of the total conductivity", *J. Solid State Electrochem.* 10 [7] (2006) 479-87.
43. T. Ishihara, S. Ishikawa, M. Ando, H. Nishiguchi and Y. Takiga, "P<sub>O2</sub> dependence of valence number of Co in LaGaO<sub>3</sub> and its influence on partial electronic and oxide ionic conductivity", *Solid State Ionics*, 173 [1-4] (2004) 9-15.
44. T. Ishihara, J. Tabuchi, S. Ishikawa, J. Yan, M. Enoki and H. Matsumoto, "Recent progress in LaGaO<sub>3</sub> based solid electrolyte for intermediate temperature SOFCs", *Solid State Ionics*, 177 [19-25] (2006) 1949-53.
45. M. Enoki, J. Yan, H. Matsumoto and T. Ishihara, High oxide ion conductivity in Fe and Mg doped LaGaO<sub>3</sub> as the electrolyte of solid oxide fuel cells", *Solid State Ionics*, 177 [19-25] (2006) 2053-57.
46. K. Huang, M. Feng, J.B. Goodenough and M. Schmerling, "Characterization of Sr-doped LaMnO<sub>3</sub> and LaCoO<sub>3</sub> as cathode

## References

---

- materials for a doped LaGaO<sub>3</sub> ceramic fuel cell”, *J. Electrochem. Soc.*, 143 [11] (1996) 3630-6.
47. L. Zhang, S.P. Jiang, W. Wang and Y. Zhang, “NiO/YSZ, anode-supported, thin-electrolyte, solid oxide fuel cells fabricated by gel casting”, *J. Power Sources*, 170 [1] (2007) 55-60.
  48. J.B. Goodenough and Y.H. Huang, “Alternative anode materials for solid oxide fuel cells”, *J. Power Sources*, 173 [1] (2007) 1-10.
  49. A. Atkinson, S. Barnett, R.J. Gorte, J.T.S. Irvine, A.J. McEvoy, M. Mogensen, S.C. Singhal and J.Vohts, “Advanced anodes for high-temperature fuel cells”, *Nature Materials*, 3 [1] (2004) 17-27.
  50. M. Mori, T. Yamamoto, H. Itoh, H. Inaba and H. Tagawa in: U. Stimming, S.C. Singhal, H. Tagawa, W. Lehnert (Eds.), *Proceedings of the Fifth International Symposium on Solid Oxide Fuel Cells*, Aachen, Germany, (1997) 869.
  51. D.W. Dees, T.D. Claar, T.E. Easler, D.C. Fee and F.C. Mrazek, “Conductivity of porous Ni/ZrO<sub>2</sub>-Y<sub>2</sub>O<sub>3</sub> cermets”, *J. Electrochem. Soc.*, 134 [9] (1987) 2141-6.
  52. E.I. Tiffée, W. Wersing and M. Schiebl, “Ceramic and metallic components for a planar SOFC”, *B. Bunsen-Ges. Phys. Chem.*, 94 (1990) 978-81.
  53. S.K. Pratihari, R.N. Bazu, S. Mazumder and H.S. Maiti in: S.C. Singhal, M. Dokiya (Eds.), *Proceedings of the Sixth International Symposium on Solid Oxide Fuel Cells*, Honolulu, Hawaii, (1999) 513.
  54. H. Itoh, T. Yamamoto, M. Mori, T. Horita, N. Sakai, H. Yokokawa and M. Dokiya, “Configurational and electrical behavior of Ni-YSZ cermet with novel microstructure for solid oxide fuel cell anodes”, *J. Electrochem. Soc.*, 144 [2] (1997) 641-6.
  55. T. Iwata, “Characterization of Ni-YSZ anode degradation for substrate-type solid oxide fuel cells”, *J. Electrochem. Soc.*, 143 [5] (1996) 1521-5.
  56. A. Tintinelli, C. Rizzo, G. Giunta and A. Selvaggi in: U. Bossel (Ed.), *Proceedings of the First European Solid Oxide Fuel Cells Forum*, Lucerne, Switzerland, (1994) 455.
  57. Y. Matsuzaki and I. Yasuda, “The poisoning effect of sulfur-containing impurity gas on a SOFC anode: Part1. Dependence on

## References

---

- temperature, time and impurity concentration”, *Solid State Ionics*, 132 (2000) 261-9.
58. D. Simwonis, F. Tietz and D. Stöver, “Nickel coarsening in annealed Ni/8YSZ anode substrates for solid oxide fuel cells”, *Solid State Ionics*, 132 [3-4] (2000) 241-51.
  59. N. Nakagawa, H. Sakurai, K. Kondo, T. Morimoto, K. Hatanaka and K.Kato, “Evaluation of the effective reaction zone at Ni (NiO)/Zirconia anode by using an electrode with a novel structure”, *J. Electrochem. Soc.*, 142 [10] (1995) 3474-9.
  60. S. McIntosh and R.J. Gorte, “Direct hydrocarbon solid oxide fuel cells”, *Chem. Rev.*, 104 [10] (2004) 4845-65.
  61. S.P. Jiang and S.H. Chan, “A review of anode materials development in solid oxide fuel cells”, *J. Mater. Sci.*, 39 [14] (2004) 4405-39.
  62. M. Mogensen and K. Kammer, “Conversion of hydrocarbons in solid oxide fuel cells”, *Annu. Rev. Mater. Res.*, 33 (2003) 321-31.
  63. J.W. Fergus, “Oxide anode materials for solid oxide fuel cells”, *Solid State Ionics*, 177 [17-18] (2006) 1529-41.
  64. M.L. Toebes, J.H. Bitter, A.J. van-Dillen, and K.P. de-Jong, “Impact of the structure and reactivity of nickel particles on the catalytic growth of carbon nanofibers”, *Catal. Today*, 76 [1] (2002) 33-42.
  65. C. Sun and U. Stimming, “Recent anode advances in solid oxide fuel cells”, *J. Power Sources*, 171 [2] (2007) 247-60.
  66. S. Tao and J.T.S. Irvine, “Discovery and characterization of novel oxide anodes for solid oxide fuel cells”, *The Chemical Record*, 4 [2] (2004) 83-95.
  67. R.J. Gorte and J.M. Vohs, “Novel SOFC anodes for the direct electrochemical oxidation of hydrocarbons”, *J. Catalysis*, 216 [1-2] (2003) 477-86.
  68. D. Hirabayashi, A. Hashimoto, T. Hibino, U. Harada and M. Sano, “Bi-based oxide anodes for direct hydrocarbon SOFCs at intermediate temperatures”, *Electrochem. Solid-State Lett.*, 7 [5] (2004) A108-10.
  69. J.C. Ruiz, J. Canales, J. Peña, D.M. López and P. Núñez, “On the simultaneous use of  $\text{La}_{0.75}\text{Sr}_{0.25}\text{Cr}_{0.5}\text{Mn}_{0.5}\text{O}_{3-\delta}$  as both anode and cathode material with improved microstructure in solid oxide fuel cells”, *Electrochimica Acta*, 52 [1] (2006) 278-84.

## References

---

70. P. Vernoux, M. Guillodo, J. Fouletier and A. Hammou, "Alternative anode material for gradual methane reforming in solid oxide fuel cells", *Solid State Ionics*, 135 [1-4] (2000) 425-31.
71. A. Kaiser, J.L. Bradley, P.R. Slater and J.T.S. Irvine, "Tetragonal tungsten bronze type phases  $(\text{Sr}_{1-x}\text{Ba}_x)_{0.6}\text{Ti}_{0.2}\text{Nb}_{0.8}\text{O}_{3-\delta}$ : Material characterisation and performance as SOFC anodes", *Solid State Ionics*, 135 [1-4] (2000) 519-24.
72. H.L. Tuller, "Oxygen ion conduction and structural disorder in conductive oxides", *J. Phys. Chem. Solids*, 55 [12] (1994) 1393-404.
73. B.J. Wuensch, K.W. Eberman, C. Heremans, E.M. Ku, P. Onnerud, E.M.E. Yeo, S.M. Haile, J.K. Stalick and J.D. Jorgensen, "Connection between oxygen-ion conductivity of pyrochlore fuel-cell materials and structural change with composition and temperature", *Solid State Ionics*, 129 [1-4] (2000) 111-33.
74. M. Pirzada, R.W. Grimes, L. Minervini, J.F. Maguire and K.E. Sickafus, "Oxygen migration in  $\text{A}_2\text{B}_2\text{O}_7$  pyrochlores", *Solid State Ionics*, 140 [3-4] (2001) 201-8.
75. C. Sun, R. Hui and J. Roller, "Cathode materials for solid oxide fuel cells: a review", *J. Solid State Electrochem.*, 14 [7] (2010) 1125-44.
76. S.B. Adler, "Factors governing oxygen reduction in solid oxide fuel cell cathodes", *Chem. Rev.*, 104 [10] (2004) 4791-844.
77. N.Q. Minh and T. Takahashi, "Science and technology of ceramic fuel cells", Elsevier, Amsterdam, (1995).
78. S.P. Jiang, J.G. Love, J.P. Zhang, M. Hoang, Y. Ramprakash, A.E. Hughes and S.P.S Badwal, "The electrochemical performance of LSM/zirconia-yttria interface as a function of a-site non-stoichiometry and cathodic current treatment", *Solid State Ionics*, 121 [1-4] (1999) 1-10.
79. O. Yamamoto, Y. Takeda, R. Kanno and M. Noda, "Perovskite-type oxides as oxygen electrodes for high temperature oxide fuel cells", *Solid State Ionics*, 22 [2-3] (1987) 241-6.
80. T. Kenjo and M. Nishiya, "LaMnO<sub>3</sub> air cathodes containing ZrO<sub>2</sub> electrolyte for high temperature solid oxide fuel cells", *Solid State Ionics*, 57 [3-4] (1992) 295-302.
81. C. Clausen, C. Bagger, J.B. Bilde-Sørensen and A. Horsewell, "Microstructural and microchemical characterization of the interface

## References

---

- between  $\text{La}_{0.85}\text{Sr}_{0.15}\text{MnO}_3$  and  $\text{Y}_2\text{O}_3$ -stabilized  $\text{ZrO}_2$ ”, *Solid State Ionics*, 70–71 [1] (1994) 59-64.
82. G. Stochniol, E. Syskakis and A. Naoumidis, “Chemical compatibility between strontium-doped lanthanum manganite and yttria-stabilized zirconia”, *J. Am. Ceram. Soc.*, 78 [4] (1995) 929-32.
83. T. Setoguchi, T. Inoue, H. Takebe, K. Eguchi, K. Morinaga and H. Arai, “Fabrication and evaluation of flat thick film type solid oxide fuel cell”, *Solid State Ionics*, 37 [2-3] (1990) 217-21.
84. H. Yokokawa, N. Sakai, T. Kawada and M. Dokiya, “Thermodynamic analysis on interface between perovskite electrode and YSZ electrolyte”, *Solid State Ionics*, 40–41 [1] (1990) 398-401.
85. J.M. Ralph, A.C. Schoeler and M. Krumpelt, “Materials for lower temperature solid oxide fuel cells”, *J. Mater. Sci.*, 36 [5] (2001) 1161-72.
86. Y. Takeda, R. Kanno, M. Noda and O. Yamamoto, “Perovskite electrodes for high temperature solid electrolyte fuel cells”, *Bull. Inst. Chem. Res.*, 64 [4] (1986) 157-69.
87. A. Weber and E.I. Tiffée, “Materials and concepts for solid oxide fuel cells (SOFCs) in stationary and mobile applications”, *J. Power Sources*, 127 [1-2] (2004) 273-83.
88. J.M. Ralph, C. Rossignol and R. Kumar, “Cathode materials for reduced-temperature SOFCs”, *J. Electrochem. Soc.*, 150 [11] (2003) A1518-22.
89. S.P. Simner, J.F. Bonnett, N.L. Canfield, K.D. Meinhardt, V.L. Sprenkle and J.W. Stevenson, “Optimized lanthanum ferrite-based cathodes for anode-supported SOFC”, *Electrochem. Solid-State Lett.*, 5 [7] (2002) A173-5.
90. S.P. Simner, J.F. Bonnett, N.L. Canfield, K.D. Meinhardt, J.P. Shelton and V.L. Sprenkle and J.W. Stevenson, “Development of lanthanum ferrite SOFC cathodes”, *J. Power Sources*, 113 [1] (2003) 1-10.
91. C.E. Hatchwell, N.M. Sammes and K. Kendall, “Cathode current-collectors for a novel tubular SOFC design”, *J. Power Sources*, 70 [1] (1998) 85-90.
92. N. Tomita, T. Namikawa, and Y. Yamazaki, “A flexible alloy-wire interconnection for planar SOFC cathode”, *J. Electrochem. Soc. Jpn. Denki Kagaku*, 62 (1994) 638-9.

## References

---

93. Y. Yamazaki, T. Namikawa, T. Ide, H. Kabumoto, N. Oishi, T. Motoki and T. Yamazaki in: U. Stimming, S.C. Singhal, H. Tagawa, W. Lehnert (Eds.), *Proceedings of the Fifth International Symposium on Solid Oxide Fuel Cells*, Aachen, Germany, (1997) 1291.
94. K. Akagi, A. Siartori, M. Iha and O. Chikagawa in: M. Dokiya, O. Yamamoto, H. Tagawa, S.C. Singhal (Eds.), *Proceedings of the Fourth International Symposium on Solid Oxide Fuel Cells*, Yokohama, Japan, (1995) 129.
95. T. Kimura, T. Namikawa and Y. Yamazaki, *J. Electrochem. Soc. Jpn. Denki Kagaku*, 61 (1993) 1115-7.
96. B.K. Flandermeyer, M.M. Nasrallah, A.K. Agarwal and H.U. Anderson, "Defect structure of Mg-doped LaCrO<sub>3</sub> model and thermogravimetric measurements", *J. Am. Ceram. Soc.*, 67 [3] (1984) 195-8.
97. W. Quadackers, H. Greiner and W. Köck in: U. Bossel, (Ed.), *Proceedings of the First European Solid Oxide Fuel Cells Forum*, Lucerne, Switzerland, (1994) 525.
98. Y. Akiyama, S. Taniguchi, T. Yasuo, M. Kadowaki and T. Saitoh, "Surface treatment of alloy separator in a planar-type solid oxide fuel cell", *J. Power Sources*, 50 [3] (1992) 361-8.
99. H. Schmidt, B. Bruckner and F. Fischer in: M. Dokiya, O. Yamamoto, H. Tagawa, S.C. Singhal (Eds.), *Proceedings of the Fourth International Symposium on Solid Oxide Fuel Cells*, Yokohama, Japan, (1995) 869.
100. T. Kadowaki, T. Shiomitsu, E. Matsuda, H. Nakagawa, H. Tsuneizumi and T. Maruyama, "Applicability of heat resisting alloys to the separator of planar type solid oxide fuel cell", *Solid State Ionics*, 67 [1-2] (1993) 65-9.
101. T. Shiomitsu, T. Kadowaki, T. Ogwaw and T. Maruyama in: M. Dokiya, O. Yamamoto, H. Tagawa, S.C. Singhal (Eds.), *Proceedings of the Fourth International Symposium on Solid Oxide Fuel Cells*, Yokohama, Japan, (1995) 850.
102. C. Hatchwell, N.M. Sammes, I.W.M. Brown and K. Kendall, "Current collectors for a novel tubular design of solid oxide fuel cell", *J. Power Sources*, 77 [1] (1999) 64-8.

## References

---

103. N.Q. Minh, "Solid oxide fuel cell technology-features and applications", *Solid State Ionics*, 174 [1-4] (2004) 271-7.
104. R.M.C. Clemmer, "The Processing and characterization of porous Ni/YSZ and NiO/YSZ composites used in solid oxide fuel cell applications", PhD thesis, University of Waterloo, Canada, (2006).
105. I.P. Kilbride, "Preparation and properties of small diameter tubular solid oxide fuel cells for rapid start-up," *J. Power Sources*, 61 [1-2] (1996) 167-71.
106. T. Suzuki, T. Yamaguchi, Y. Fujishiro, and M. Awano, "Fabrication and characterization of micro tubular SOFCs for operation in the intermediate temperature", *J. Power Sources*, 160 [1] (2006) 73-7.
107. N.M. Sammes and Yanhai Du, "Fabrication and characterization of tubular solid oxide fuel cells", *Int. J. Appl. Ceram. Technol.*, 4 [2] (2007) 89-102.
108. L. Zhang, H.Q. He, W.R. Kwek, J. Ma, E.H. Tang and S.P. Jiang, "Fabrication and characterization of anode-supported tubular solid-oxide fuel cells by slip casting and dip coating techniques", *J. Am. Ceram. Soc.*, 92 [2] (2009) 302-10.
109. E. Traversa, "Toward the miniaturization of solid oxide fuel cells", *Electrochemical Society Interface*, 18 [3] 2009 49-52.
110. T. Yamaguchi, T. Suzuki, S. Shimizu, Y. Fujishiro, and M. Awano, "Examination of wet coating and co-sintering technologies for micro-SOFCs fabrication", *J. Membrane Science*, 300 [1-2] (2007) 45-50.
111. T. Suzuki, Y. Funahashi, T. Yamaguchi, Y. Fujishiro and M. Awano, "Effect of anode microstructure on the performance of micro tubular SOFCs", *Solid State Ionics*, 180 [6-8] (2009) 546-49.
112. V. Lawlor, S. Griesser, G. Buchinger, A.G. Olabi, S. Cordiner and D. Meissner, "Review of the micro-tubular solid oxide fuel cell: Part I. Stack design issues and research activities", *J. Power Sources*, 193 [1-2] (2009) 387-99.
113. T. Suzuki, Y. Funahashi, T. Yamaguchi, Y. Fujishiro, and M. Awano, "Fabrication and characterization of micro tubular SOFCs for advanced ceramic reactors", *J. Alloys Comp.*, 451 [1-2] (2008) 632-5.
114. T. Suzuki, Y. Funahashi, Z. Hasan, T. Yamaguchi, Y. Fujishiro, and M. Awano, "Fabrication of needle-type micro SOFCs for micro power devices", *Electrochem. Commun.*, 10 [10] (2008) 1563-6.

## References

---

115. Y. Funahashi, T. Shimamori, T. Suzuki, Y. Fujishiro, and M. Awano, "Fabrication and characterization of components for cube shaped micro tubular SOFC bundle", *J. Power Sources*, 163 [2] (2007) 731-6.
116. T. Suzuki, Y. Funahashi, T. Yamaguchi, Y. Fujishiro, and M. Awano, "Anode-supported micro tubular SOFCs for advanced ceramic reactor system", *J. Power Sources*, 171 [1] (2007) 92-5.
117. T. Suzuki, Y. Funahashi, T. Yamaguchi, Y. Fujishiro, and M. Awano, "Development of cube-type SOFC stacks using anode-supported tubular cells", *J. Power Sources*, 175 [1] (2008) 68-74.
118. N.M. Sammes, Y. Du, and R. Bove, "Design and fabrication of a 100 W anode supported micro-tubular SOFC stack", *J. Power Sources*, 145 [2] (2005) 428-34.
119. Y. Liu, S.I. Hashimoto, H. Nishino, K. Takei, M. Mori, T. Suzuki and Y. Funahashi, "Fabrication and characterization of micro-tubular cathode-supported SOFC for intermediate temperature operation", *J. Power Sources*, 174 [1] (2007) 95-102.
120. T. Yamaguchi, S. Shimizu, T. Suzuki, Y. Fujishiro and M. Awano, "Fabrication and evaluation of cathode-supported small scale SOFCs", *Materials Letters*, 62 [10-11] (2008) 1518-20.
121. T. Yamaguchi, S. Shimizu, T. Suzuki, Y. Fujishiro and M. Awano, "Fabrication and characterization of high performance cathode supported small-scale SOFC for intermediate temperature Operation", *Electrochem. Commun.*, 10 [9] (2008) 1381-3.
122. G.J. Saunders and K. Kendall, "Reactions of hydrocarbons in small tubular SOFCs", *J. Power Sources*, 106 [1-2] (2002) 258-63.
123. N. Yang, X. Tan, Z. Ma, and A. Thursfield, "Fabrication and characterization of  $\text{Ce}_{0.8}\text{Sm}_{0.2}\text{O}_{1.9}$  microtubular dual-structured electrolyte membranes for application in solid oxide fuel cell technology", *J. Am. Ceram. Soc.*, 92 [11] (2009) 2544-50.
124. K. Kendall, "Progress in microtubular solid oxide fuel cells", *Int. J. Appl. Ceram. Technol.*, 7 [1] (2010) 1-9.
125. D. Beckel, A. Bieberle-Hütter, A. Harvey, A. Infortuna, U.P. Muecke, M. Prestat, J.L.M. Rupp and L.J. Gauckler, "Thin films for micro solid oxide fuel cells", *J. Power Sources*, 173 [1] (2007) 325-45.

## References

---

126. Y. Zhang, J. Gao, D. Peng, M. Guanyao and X. Liu, "Dip-coating thin yttria-stabilized zirconia films for solid oxide fuel cell applications", *Ceramics International*, 30 [6] (2004) 1049-53.
127. J. Ding, J. Liu, W. Yuan and Y. Zhang, "Slip casting combined with colloidal spray coating in fabrication of tubular anode-supported solid oxide fuel cells", *J. Eur. Ceram. Soc.*, 28 [16] (2008) 3113-7.
128. T. Suzuki, Y. Funahashi, T. Yamaguchi, Y. Fujishiro and M. Awano, "Performance of the micro-SOFC module using submillimeter tubular cells", *J. Electrochem. Soc.*, 156 [3] (2009) B318-21.
129. Y. Liu, M. Mori, Y. Funahashi, Y. Fujishiro and A. Hirano, "Development of micro-tubular SOFCs with an improved performance via nano-Ag impregnation for intermediate temperature operation", *Electrochem. Commun.*, 9 [8] (2007) 1918-23.
130. T. Yamaguchi, S. Shimizu, T. Suzuki, Y. Fujishiro and M. Awano, "Demonstration of the rapid start-up operation of cathode-supported SOFCs using a microtubular LSM support", *J. Electrochem. Soc.*, 155 [11] (2008) B1141-4.
131. Y.W. Sin, K. Galloway, B. Roy, N.M. Sammes, J.H. Song, T. Suzuki and M. Awano, "The properties and performance of micro-tubular (less than 2.0mm O.D.) anode supported solid oxide fuel cell (SOFC)", *Int. J. Hydrogen Energy* 36 [2] (2010) 1882-9.
132. C. Yang, W. Li, S. Zhang, L. Bi, R. Peng, C. Chen and W. Liu, "Fabrication and characterization of an anode-supported hollow fiber SOFC", *J. Power Sources*, 187 [1] (2009) 90-2.
133. N. Droushiotis, M.H.D. Othman, U. Doraswami, Z. Wu, G. Kelsall and K. Li, "Novel co-extruded electrolyte-anode hollow fibres for solid oxide fuel cells", *Electrochem. Commun.*, 11 [9] (2009) 1799-802.
134. N. Droushiotis, U. Doraswami, D. Ivey, M.H.D. Othman, K. Li and G. Kelsall, "Fabrication by co-extrusion and electrochemical characterization of micro-tubular hollow fibre solid oxide fuel cells", *Electrochem. Commun.*, 12 [6] (2010) 792-5.
135. P. Sarkar, L. Yamarte, H. Rho, and L. Johanson, "Anode-supported tubular micro-solid oxide fuel cell", *Int. J. Appl. Ceram. Technol.*, 4 [2] (2007) 103-8.

## References

---

136. T. Suzuki, T. Yamaguchi, Y. Fujishiro and M. Awano, "Current collecting efficiency of micro tubular SOFCs", *J. Power Sources*, 163 [2] (2007) 737-42.
137. D. Cui, L. Liu, Y. Dong and M. Cheng, "Comparison of different current collecting modes of anode supported micro-tubular SOFC through mathematical modeling", *J. Power Sources*, 174 [1] (2007) 246-54.
138. A.V. Virkar, F.F. Lange and M.A. Homel, "A simple analysis of current collection in tubular solid oxide fuel cells", *J. Power Sources*, 195 [15] (2010) 4816-25.
139. C. Mallon and K. Kendall, "Sensitivity of nickel cermet anodes to reduction conditions", *J. Power Sources*, 145 [2] (2005) 154-60
140. Patent Cooperation Treaty (PCT), International publication number WO 2007/005675 A1.
141. H. Zhu and R.J. Kee, "The influence of current collection on the performance of tubular anode-supported SOFC cells", *J. Power Sources*, 169 [2] (2007) 315-26.
142. J.J. Sun, Y.H. Koh, W.Y. Choi and H.E. Kim, "Fabrication and characterization of thin and dense electrolyte-coated anode tube using thermoplastic coextrusion", *J. Am. Ceram. Soc.*, 89 [5] (2006) 1713-6.
143. D. Montinaro, "Synthesis and processing of oxides powders for solid oxide fuel cells (SOFC) production", PhD Thesis, Università degli studi di Trento, Italy, (2007).
144. R. De-La-Torre, "Fabrication of mullite from kyanite-bauxite and kyanite-pseudoboehmite mixtures", M.Sc. Thesis, National Polytechnic Institute, Mexico, (2006).
145. D. Dong, J. Gao, X. Liu and G. Meng, "Fabrication of tubular NiO/YSZ anode-support of solid oxide fuel cell by gelcasting", *J. Power Sources*, 165 [1] (2007) 217-23.
146. M. Costa-Sousa, J.W. Buchanan, "Observational models of graphite pencil materials", *J. Computer Graphics Forum*, 19 [1] (2000) 27-49.